HOST UNIVERSITY: University of Maryland

FACULTY: A. James Clark School of Engineering

DEPARTMENT: Department of Fire Protection Engineering

Academic Year 2019-2020

Numerical Simulations of Brand Transport in Large Outdoor Fires

Leo Willem Menzemer

Promoters:

Prof. Arnaud Trouvé, University of Maryland

Prof. Bart Merci, Ghent University

Master thesis submitted in the Erasmus+ Study Programme

International Master of Science in Fire Safety Engineering

DISCLAIMER

This thesis is submitted in partial fulfilment of the requirements for the degree of *The International Master of Science in Fire Safety Engineering (IMFSE)*. This thesis has never been submitted for any degree or examination to any other University/programme. The author(s) declare(s) that this thesis is original work except where stated. This declaration constitutes an assertion that full and accurate references and citations have been included for all material, directly included and indirectly contributing to the thesis. The author(s) gives (give) permission to make this master thesis available for consultation and to copy parts of this master thesis for personal use. In the case of any other use, the limitations of the copyright have to be respected, in particular with regard to the obligation to state expressly the source when quoting results from this master thesis. The thesis supervisor must be informed when data or results are used.

Read and approved,

Leo Willem Menzemer

(Stadthagen, Germany - April 30th, 2020)

Abstract

In wildland fires, burning particles of vegetative material can be lofted by the fire plume and are subsequently transported horizontally by cross wind. Depending on the state of the firebrands (flaming, smoldering, inert hot, inert cold) upon landing they bear the potential to cause secondary fires. The present work introduces theoretical analysis of the problem of combustion and transportation of firebrands. Afterwards, possible approaches to numerical modelling of the important aspects of the problem are discussed. Fire Dynamics Simulator is used as computational tool and a pyrolysis model is developed based on the reaction rates from first order Arrhenius equations. Firebrands exposed to high temperatures are found to fully pyrolyze in the first seconds after exposure to the fire and lower initial temperatures enable pyrolysis to sustain for a longer time while also reducing the cooling rates of firebrands, because energy losses to endothermic pyrolysis are minimized. Increasing thickness and density of firebrands leads to the same effect due to increasing thermal inertia. The mass loss is established as most accurate criterion to define whether a particle is still flaming or not. A three-dimensional numerical model is presented with a flow field from a 100 MW tree crown fire at wind speeds of 6.7 m/s. Firebrands equivalent to disc-like geometries with densities from 50-200 kg/m³, 4 and 10 cm diameter, and 0.2 to 10 cm thickness are released from the canopy. The product $\rho_f^{w_0} \times \tau$ is found to be a controlling factor of the firebrand dynamics and results show that particles with $\rho_f^{w_0} \times \tau \geq 1$ are not lofted by the plume and land on the ground flaming, at a maximum travel distance of 10 m downstream. Particles $\rho_f^{w_0} \times \tau \leq 0.6$ are found to be lofted and travel at least 50 m from the fire. Future investigations need to address the validation of the pyrolysis model and invoking a model for char oxidation to allow analysis of firebrands that get lofted and do not land in a flaming state.

Abstract (German)

In Wald- und Flächenbränden kann brennendes Material durch den Plume aufwärts und durch Wind anschließend horizontal transportiert werden. Abhängig vom Zustand beim Landen (lodernd, glühend oder inert mit hoher oder niedriger Oberflächentemperatur) können diese brennenden Partikel Sekundärbrände auslösen. Die vorliegende Arbeit beschäftigt sich mit den theoretischen Ansätzen zum Transport solcher Glutteilchen und ebenso mit der Verbrennung dieser. Anschließend werden mögliche Ansätze diskutiert, welche angewendet werden können, um die relevanten Aspekte des Problems numerisch zu modellieren. Der Fire Dynamics Simulator (FDS) wird als Werkzeug zum Erstellen eines Computermodells und als Gleichungslöser eingesetzt. Die Reaktionsraten zur Pyrolyse werden durch eine Arrhenius-Gleichung erster Ordnung abgebildet und anschließende Einzeltests von Glutteilchen zeigen, dass unter hohen Temperaturen ($\geq 900°C$) ein Verkohlen des gesamten Materials binnen Sekunden abläuft. Niedrigere initiale Temperaturen verlängern den Pyrolyseprozess und führen zu reduzierten Abkühlungsraten der Teilchen, da weniger Energie an die endotherme Pyrolyse verloren geht. Erhöhte Stärke und Dichte der Partikel schlagen sich ähnlich nieder, da die thermische Trägheit des Körpers zunimmt. Als zuverlässiges Kriterium zur Definition des Zustands indem sich ein Glutteilchen befindet, wird die Massenverlustrate etabliert. Ein dreidimensionales numerisches Modell wird letztlich erarbeitet, welches ein Strömungsfeld berechnet, das sich aus einem Baumkronenbrand mit einer Gesamtintensität von 100 MW und Wind mit einer Geschwindigkeit von 6,7 m/s ergibt. Plattenförmige Glutteilchen mit viereckiger Grundfläche werden in Annäherung an scheibenförmige Teilchen mit verschiedenen Dichten (50-200 kg/m³), Durchmessern (4 und 10 cm) und Stärken (0.2-10 cm) am oberen Ende der windabgewandten Seite des Blätterdachs in die Strömung eingelassen. Das Produkt aus anfänglicher Dichte und Stärke, $\rho_f^{w_0} \times \tau$, erweist sich als aussagekräftigste Größe, um die Dynamik von Glutteilchen zu kategorisieren. Teilchen mit $\rho_f^{w_0} \times \tau \geq 1$ werden nicht durch den aufwärts strömenden Plume angehoben und nur durch den Wind seitwärts transportiert und landen etwa mit 10 m Entfernung zum Feuer in loderndem Zustand. Teilchen mit $\rho_f^{w_0} \times \tau \leq 0.6$ werden allesamt in den Plume eingesogen und landen nichtlodernd im Abstand von mindestens 50 m bis über 1000 m zum Brandherd. Künftige Weiterentwicklungen des Modells sollte sich insbesondere der Validierung des Pyrolysemodells widmen, als auch ein Modell für die heterogene Oxidation der Kohleschicht vorantreiben. Diese Reaktion bestimmt das Verhalten und den Zustand des Glühens im Anschluss an das lodernde Brennen eines Teilchens maßgeblich.

IMFSE Master Thesis Declaration

This form has been developed in the context of the unforeseen circumstances due to Covid-19, necessitating a reduction of practical project work (whether it be laboratory based, computational, or fieldwork) during the master thesis semester. It acts as a record of the impact on the master thesis. The form has been completed by the student and verified by the supervisor. **A copy of the signed form is included behind the abstract in the dissertation.**

Name: Leo Willem Menzemer

Work completed

All items of wholly, or partially completed work must be listed, indicating the percentage completion for each task. **Please take care to provide a full detailed list of all work done.**

The work could be carried out as expected.

Work not commenced

Any items of outstanding work that have not been started should be listed here.

Declaration

To the best of our knowledge, this form is an accurate record of the project status on (date)

Student:_____(Signature)

Supervisor: Arnaud Trouvé 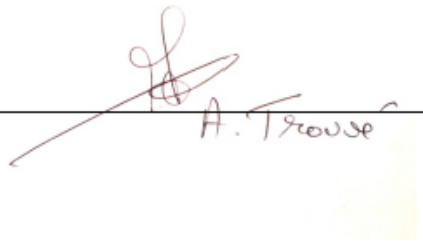

Abbreviations

CFD	Computational Fluid Dynamics	HOR	Heat of Reaction
DNS	Direct Numerical Simulation	LES	Large-Eddy Simulation
DWF	Dry Wildland Fuel	MLRPUA	Mass Loss Rate Per Unit Area
FDS	Fire Dynamics Simulator	RANS	Reynolds-Averaged Navier-Stokes
GPP	Gaseous Pyrolysis Product(s)	WUI	Wildland-Urban Interface

Nomenclature

A	pre-exponential factor	T	temperature
A_{cs}	cross sectional area	u	velocity
c_p	Specific heat	v	volume
D	diameter	V	volume
g	gravity acceleration vector	z	height
ΔH_c	heat of combustion	**Greek symbols**	
ΔH_r	heat of reaction	α	phase volume fraction
h	heat transfer coefficient	ε	emissivity
k	thermal conductivity	κ	Von Kármán constant
L	length	λ	thermal conductivity
m	mass	η	aspect ratio
$\dot{Q}$	heat release rate	ρ	density
s	(surface) area	τ	thickness
t	time		

Subscripts and superscripts

$char$	residual char	r	radiative
cr	critical	ref	reference value
CO	carbon monoxide	s	solid phase
f	firebrand	$soot$	soot
g	gas phase	t	time
H_2O	water	v	vegetation
k	solid phase (fire source)	vap	vaporization
O, ox	oxidation	w	wood (vegetation)
p	particle	0	initial value
pyr	pyrolysis	∞	value of the ambient
R	relative		

List of Equations

List of Figures

List of Tables

Contents

1 Introduction

Wildfires pose an immediate threat to the environment and in areas where structures are arranged close to wild land, referred to as wildland-urban interface (WUI), they endanger people and their homes as well. In the United States alone, it was estimated in 2005 that more than 42 million homes are located within such areas and since 1984 on average 850 homes are destroyed by wild fires annually, since 2000 this number rose to 1,100 [1]. Furthermore, the fires cause significant financial damage. The California wild fires in 2003, for example, caused damages adding up to over 2 billion dollars alone [1]. Additionally, the suppression of outdoor fires is hard and needs a lot of resources in fire-fighting which resulted in 1.3 billion dollars being spent annually in the US from federal agencies towards suppression efforts between 2000 and 2003 [1].

The recent development in climate change is seen as a driving force in increasing the threats from wild fires and producing fire-prone environments in the years to come [2] where for some regions a doubling in risk for major forest fires is estimated in case of a global warming of 2 °C and the effect is already noticeable at the time [3].

In 2017 the most severe wild fires in the history of British Columbia, Canada, occurred resulting in 1.2 million ha of land being burnt, 65,000 evacuated and 649 million dollars in costs for fire suppression [4]. In 2018 Sweden suffered the most severe forest fires in the country's history with a burnt area of almost 25,000 ha after already being struck in 2014 by exceptional fires [5]. The 2018 fires could only be fought with international help from various European Countries [5]. In 2014, almost 15,000 ha area were burnt [5] and more than 1,000 people and 1,700 animals had to be evacuated and one person died in the fire [6].

Currently, Australia is going through a bush fire season of historical severity. From November 2019 until February 2020 more than 18,600,000 ha land were burnt, and 34 casualties are reported along with the evacuation of thousands [7]. Professor Christopher Dickman from the University of Sydney estimates that since the start of the fires in 2019 until early January 2020 more than 1 billion animals have died in the fires [8].

The suppression of wildfires is not easily done as they can spread quickly and suddenly. Three fire spread mechanisms can be distinguished in wild fires: Radiative and Convective heat transfer, and the spread via spotting, where burning brands from the main fire are lofted in the air by the fire plume and are then transported by the wind causing secondary fires upon landing ahead of the flame front [1,9,10]. Depending on the size of the fire, weather conditions and brand properties, spot fires can occur up to several kilometres away from the source of the brands [9,11]. Investigations suggest that in WUI fires spotting is the main fire spread mechanism that leads to ignition of structures [12]. Other ways of fire spread become less effective

once reaching residential areas since the wildfire decreases in intensity due to the decrease of vegetative fuel [13]. Spotting fires were recorded, for instance, to be responsible for the vast extent of fire spread in the great fire of London in 1666, during which residents formed a ring to protect St. Pauls' cathedral but could not save it as firebrands ignited the church's roof. In fact, the phenomenon, later described as "leaping" fires, was numerously reported and a main cause for fire spread during the London fire [14]. A rich summary of further historical reports for fire spread due to firebrands can be found in Koo et al. (2010) [15].

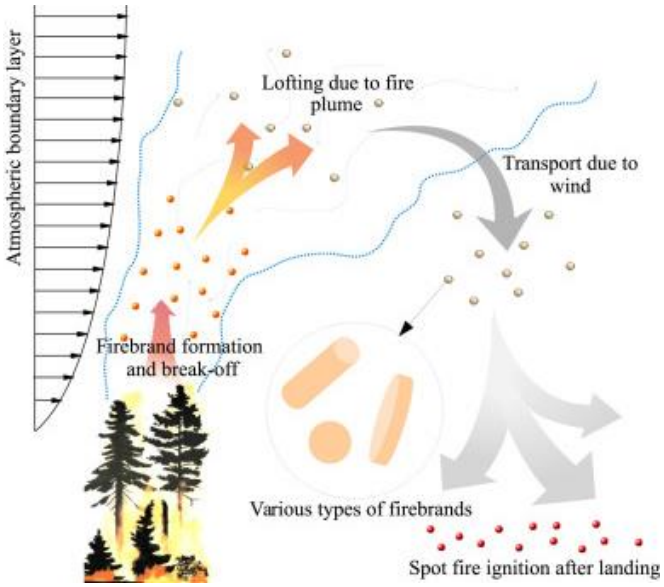

Figure 1: Schematic diagram of the spotting process from firebrand formation and break-off through lofting, wind driven transport, and spot fire ignition [13].

The formation of spot fires is schematically explained in Figure 1 [13] and can be subdivided in multiple consecutive steps:

First, firebrands are formed when combusting particles break off from larger burning structures or vegetation as a result of the weakening of the material by combustion and the forces acting on it [13]. The characterization of firebrands is primarily done regarding their shape, where usually spherical, cylindrical and disc shapes are distinguished [15–17]. Recent research in the firebrand generation from burning trees and vegetation suggest that mainly cylindrical and disc shaped brands are generated in wild fires [13,18]. Several set of experiments, where different pine trees were burnt under no-wind-conditions and the generated brands were weighed and measured, showed that all brands that were collected were solely of cylindrical shape [9,19–21]. Figure 2 [19] shows a sample of the brands from these experiments.

Secondly, the firebrands are lofted in the air by the fire plume and are transported horizontally by wind actions. Lastly, the brands will burn to completion or extinguish while in the air, or land on the ground in a smoldering or flaming state bearing a potential to cause secondary fires [15].

Figure 2: Photography of collected firebrands [19].

The transport of firebrands is often analyzed in respect of the maximum spotting distance [11,22] as this might be one of the most important outputs in the predictions of wildfire behaviour. With increasing fire intensity, the spotting distance increases due to the higher vertical velocity of the plume [15]. The distance a burning ember can travel depends on its initial size and the burning rate of the material [23]. While smaller particles potentially travel farther than larger ones as they are lofted higher in the plume and sink to the ground slower, they may burn out before falling to the ground and hence, the maximum spotting distance is also a function of the lifetime of a firebrand, depending on its initial properties and its combustion parameters [11]. Further influence on the transport of burning particles are the weather conditions as firebrands tend to be carried over longer distances with higher ambient temperatures under the same wind conditions, which further influence the brand transport in obvious ways for themselves, too [24].

Firebrands that are not burnt out by the time of their landing can potentially cause a spot fire. While the maximum spotting distance is one interesting parameter that can be analyzed it is also important to look at firebrands that travel shorter distances. Especially in WUI fires, it might not be the maximum distance that a brand can travel and land in a glowing state that is of interest, but the flux of firebrands that structures closer to the fire are exposed to [18]. Consequently, risk assessments for these regions could be carried out as the ignition of solids by firebrands is a problem that involves ignition criteria of the respective fuel, the heat capacity of firebrands and the heat transfer between firebrands, air and the fuel as well as the complex aspects of smoldering combustion and fire spread through it [15].

1.1 Research Objective

The aim of this manuscript is to lay a foundation for developing a numerical model using computational fluid dynamics for the problem of firebrand transport in large outdoor fires. In the best case, the model should be able to predict the flight paths for reacting firebrands that are generated in wildland fire scenarios. Associated with this capability is the tracking of particle properties in time and space along the projected trajectories. Detailed results on, for example, temperature and mass of a firebrand at the time that it falls to the ground enables analysis regarding the state that the particle is in at that time. That might be flaming combustion, smoldering or inert after self-extinguishment, but even non-reacting hot brands bear the potential to cause secondary fires.

In the following work, the theoretical aspects that need consideration in the firebrand transport and spotting ignition problem are first approached theoretically and the current state of the research regarding these topics shall be presented, before the approach to numerical modelling of the problem is to be discussed.

Ultimately, the model that is developed throughout this research project shall be used to analyze the instantaneous properties of firebrands when reaching the ground with regard to their landing distance from the fire and the initial properties of the particle. The combustion of firebrands needs to be investigated in order to define a criterion that allows simple, but more importantly accurate, classification of the firebrand's state upon landing. These results can then be a source to enable an assessment of the potential threats to areas exposed differently to firebrand showers in wildland fires.

2 Theory and Research on Fire Spread through Firebrands

The following chapter is meant to give an overview on the theory that covers the multiple aspects of fire spread through firebrands and discuss it briefly but sufficiently thorough. The formation and break-off mechanisms as well as secondary ignition are not part of the numerical study that is conducted in this work, but they are addressed nonetheless to generate understanding of the problem of firebrand transport and subsequent spot fire ignition as a whole and present the current state of research in the field.

2.1 Firebrand Formation and Characteristics

Hot particles that are transported from the location of their formation to another place bear the risk of causing secondary ignition. This includes hot pieces of metal as they can, for example, emerge from power line interactions and hot or mechanical work [25]. In wildfires, however, the more important kind of hot particles are firebrands, which are small burning or smoldering particles formed during the burning of vegetation or structures that compose of such material [25].

Generally, firebrands form when parts of trees, other plants or vegetative fuel are weakened in their structural integrity due to a fire and the forces acting on those parts, for example induced by wind, become larger than the bearing capacity of the material [13]. These mechanisms, however, are very complex to describe and are not extensively studied. Predictive models would have to deal with the highly fluctuating characteristic properties of the vegetation due to the sensitive dependence on e.g. atmospheric conditions and generically complex geometries [13]. Caton-Kerr et al. [26] recently published their work on the behaviour of thermally-degraded cylindrical woods under external loading. Further research in this topic, could aim for a time-dependent firebrand release model for various species [26].

The currently more feasible approach for data on the characteristics of firebrands, such as shape, size or density, seems to be experimental. There have been numerous experimental studies in the past years in which firebrands generated from burning trees [9,20,21,27] and structures [28–32] were collected, measured and weighed.

Firebrands are typically considered to be spherical, rod-like (cylindrical, rectangular) or in the shape of a disc [13,22,23,33–35] as shown in Figure 3 and they can be described using their respective characteristic dimensions. However, when investigating on the behaviour of firebrands, it is often more convenient to introduce an aspect ratio, η, instead. The aspect ratio for disc-like, cylinders and rectangular shapes, respectively, is defined as [13,33,34]:

$$\eta = \frac{\tau}{D};\ \eta = \frac{L}{D};\ \eta = \frac{L_z}{L_{x,y}} \quad \text{for} \quad L_x = L_y \tag{2-1}$$

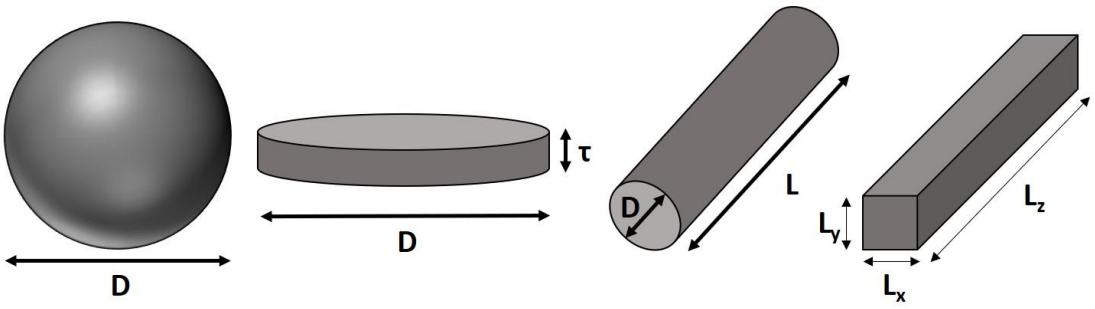

Figure 3: Typical shapes for firebrands.

Naturally, real firebrands will deviate from the idealized shapes presented in Figure 3. Experimentally obtained data for the size of (irregular or inconsistent shaped) firebrands is therefore often presented with the approximate surface area of the brands, together with their density and mass [28–30]. The surface area is related to the pyrolysis and oxidation of firebrands as well as the heat transfer towards fuels they might land on, aspects that are discussed in later chapters.

In recent works investigating the characteristics of firebrands from burning structures, Suzuki and Manzello [30] have included a table that lists findings from similar studies. Their results from this study fit those from other experiments well. In detail, firebrands generated in fires of structures were found to have mostly a surface area <10 cm² and weigh less than 1 g [30], while the correlation between size and mass is seemingly linear (Figure 5a). Nonetheless, there are also significant numbers of brands that exceed these numbers. In the presented work, firebrands were collected after an urban fire in Itoigawa-city, Niigata, Japan in 2016 that went on for 30h and destroyed 120 structures, the largest firebrand that was found weighed 114g and had a projected area of 130 cm² with a thickness of 3 cm (Figure 4) [30].

In studies investigating firebrands from full-scale fires of structures various shapes of brands are reported [29,30]. In contrast, full-scale experiments in which trees were burnt and the generated firebrands were collected and analyzed, solely cylindrical brands were found (Figure 2) [19–21]. The correlation between size and mass in this case follows a power-law where the surface area (s) correlates linearly with $m^{\frac{2}{3}}$ (Figure 5b) [13] and the brands show a similar characteristic distribution in size and weight (<10 cm² and < 1 g) as those formed in the fires of structures [9,21].

Figure 4: Large firebrand found in an urban fire in Japan [30].

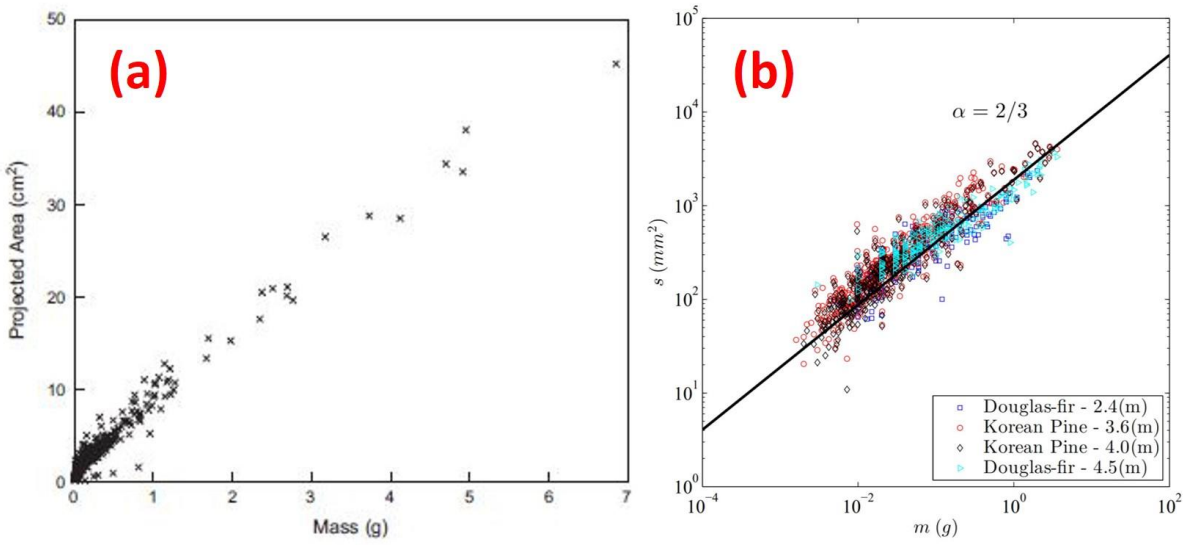

Figure 5: Size and mass distribution for firebrands from (a) structural fuel fires [29] and (b) wildland fuel fires [13].

Besides the geometry, further interesting properties of the firebrands are the material density, the thermal properties (such as heat capacity and conductivity) and the initial moisture content as these parameters influence the burning behaviour of the particles and depend on the species the brands originate from as well as external conditions the fuel is subjected to.

2.2 Firebrand Transport

The effects of firebrands depend on their landing spot either in the near or far field from the original fire, where long-range firebrands are lifted high in the sky by the plume of the outdoor fire and are subsequently transported horizontally by wind over long distances [36]. Fires that are started from these embers, are developing independently from the original fire source before they are assimilated by the original flame front they might as well act as an independent fire when the original flame front does not catch up. In contrast, fires originating from short-range firebrands might either have no significant influence on fire spread as they are incorporated by the original fire before they get to develop or they can increase the rate of fire spread if they land far enough ahead of the original flame front so they can significantly develop before being absorbed in the original fire [36]. Both types, however, might bridge gaps in vegetative fuel that has been man-made to impair the spread of wildland fires and pose a potential threat to firefighters that might not be aware of recently new ignited fires behind them and could get trapped between the flame fronts [36].

The momentum of a particle is governed by [37]:

$$m_p \frac{d\vec{V}_p}{dt} = \vec{F}_g + \vec{F}_D \qquad (2\text{-}2)$$

$$\frac{d\vec{r}_p}{dt} = \vec{V}_p \tag{2-3}$$

In this context, $\vec{V}_p$ is the velocity of the particle in the horizontal directions x and y and the vertical z direction with respect to the ground and $\vec{r}_p$ is the position of the particle in each direction. $\vec{F}_g$ is the gravity force that is 0 in both horizontal directions and $\vec{F}_D$ is the drag force on a particle [37]:

$$\vec{F}_g = m_p \vec{g} \tag{2-4}$$

$$\vec{F}_D = \frac{1}{2} C_D \rho_{air} A_{cs} \left|\vec{V}_R\right|^2 \frac{\vec{V}_R}{|\vec{V}_R|} \tag{2-5}$$

with $\vec{V}_R = \vec{V}_w - \vec{V}_p$ being the relative velocity between the particle and the air. From combining the equations for drag and gravitational force and momentum of a particle, the following equations are found for governing the motion of particles in space [22,37]:

$$\frac{dV_{p,x}}{dt} = \frac{1}{2m_p} C_D \rho_{air} A_{cs} |\vec{V}_R| (V_{w,x} - V_{p,x}) \tag{2-6}$$

$$\frac{dV_{p,y}}{dt} = \frac{1}{2m_p} C_D \rho_{air} A_{cs} |\vec{V}_R| (V_{w,y} - V_{p,y}) \tag{2-7}$$

$$\frac{dV_{p,z}}{dt} = \frac{1}{2m_p} C_D \rho_{air} A_{cs} \left|\vec{V}_R\right| (V_{w,z} - V_{p,z}) - g \tag{2-8}$$

where

$$\frac{dx_p}{dt} = V_{p,x} \tag{2-9}$$

$$\frac{dy_p}{dt} = V_{p,y} \tag{2-10}$$

$$\frac{dz_p}{dt} = V_{p,z} \tag{2-11}$$

The trajectory of a particle can be obtained as the solution of to the equations *(2-6)-(2-11)* [37]. An additional complication to the problem now is that the particles that have to be considered in wildland fire spread decrease in mass and thickness over time. As a consequence, they reduce in their cross sectional area and geometry and hence the drag coefficient is a transient parameter as well, which has to be obtained experimentally and depends on the geometry of the particle [22,37].

The process of the transportation of firebrands in outdoor fire problems can be divided in two phases: the lofting by the buoyant plume and horizontal transport by wind [11]. The plume flow field that is established from the hot gases emerging from the fire as those gases rise upward due to their lower density and resulting buoyancy and entrain cold air on the way cooling down with height. This way, velocity and temperature profiles are established within the horizontal planes of the plume that have their peak along the centerline and converge towards the values of the ambient with distance from the plume center.

For the description of the equations that govern the momentum and energy content of the gases and the buoyancy forces on them to derive analytical expressions of the velocities and temperatures inside the plume, the interested reader is referred to the literature which addresses the fundamentals of this subject very well [38]. In practice, engineering correlations for axisymmetric plumes that were derived from experiments are widely used to obtain solutions for the plume velocity and temperature profiles. Some of these correlations will be briefly addressed in a later chapter of this manuscript.

The wind velocities that influence a particle once it has left the fire plume transport the particle over horizontal distances. This part is, however, not as straight forward, because the horizontal velocities of air are a function of the height decreasing near to the ground as a result of frictional drag [37]. An approach to model adequate wind and temperature profiles for the atmosphere in dependence of the height above the ground is presented in chapter 3.5 that addresses the boundary conditions to the numerical transportation model.

As a starting point to solve for the trajectories of firebrands from the governing equations *(2-6)* to *(2-11)*, Tarifa et al. [22] have shown from experiments, that firebrands can be assumed to travel at their terminal velocity almost immediately after being released. It usually takes the particles up to 3 seconds to come close to their asymptotic final values for their velocity and compared to the burning times of several minutes, the approximation to assume firebrands to always travel at their terminal velocities produces negligible errors in the solution in terms of the practical use of this assumption [22]. Following this approximation, the relative velocity between the particle and the wind will be 0 in the horizontal direction, and the particle velocity can be calculated from the wind velocity and the falling velocity due to gravity forces.

The transportation of firebrands has been addressed in research on secondary ignition from wildfires the most thoroughly of all the involved aspects so far:

Albini [11] has developed a relatively simple calculation model to predict the maximum spotting distance for firebrands from smaller tree fires where single trees or smaller groups of them “torch out”. The model was developed as a quick approach for planners that work in forest environments and as a tool to improve prevention of forest conflagrations. It includes a step-

by-step procedure that is arranged as a single-page worksheet, to calculate the horizontal travel distances of embers from a specific fire incident [11]. Albini's work includes a simple combustion model for firebrands to model the decrease in density and size over time depending on the initial properties and characteristics of the embers and wind velocities, it is addressed in the section on pyrolysis later in this chapter.

There have been many studies that address the trajectories of firebrands which are very thoroughly reviewed in Koo et al. [15]. It can be summarized that the burning of the firebrands is mostly referred to as the most crucial and complex part of the problem in order to come to accurate results for the trajectories, because the secondary ignition after landing and the generation of firebrands can be analyzed in decoupled approaches. The combustion process, on the other side, actually adds another transient dimension to the transport of brands and needs to be considered simultaneously. Even works of numerical modelling of the trajectories face the same problems as it is often hard to correctly estimate the kinetic parameters of the problem which leads to uncertainty in the results [39].

Fundamental research recently conducted by Tohidi and Kaye [33] shows that the problem of firebrand transport needs a coupling of the flow fields from upward flowing plumes and cross wind. In the study a series of inert model brands, consisting of polyurethane foam, with different aspect ratios was released in a vertical jet within a wind tunnel, representing a fire plume in cross wind. Tohidi and Kaye [33] come to the conclusion that the entire flow field needs to be modelled as the maximum landing locations normalized over the maximum lofting heights show similar probability density functions in their analysis regardless of the aspect ratio, which indicates that the lofting height significantly influences the travelling distance. Furthermore, the trajectories of the brands are found to be very sensitive to the initial conditions of the release and variations in the velocity field [33].

The maximum height to which a firebrand is lofted is hence influencing the spotting distance significantly, which is consistent following the theory on the particle transport. The brand will travel at terminal velocities in horizontal and vertical directions and the higher it rises before it begins falling down, the farther it can travel horizontally before reaching the ground. However, for combusting particles this travel distance is also limited by the time the particle takes to burn out as only particles landing before their respective burn out time pose a fire hazard. The sensitivity to the changes in the velocity fields that are highly fluctuating for high intensity outdoor fires, indicate that it is inevitable to model the entire flow field as it emerges from the fire and the resulting plume and the cross wind in a coupled approach to get accurate results [33].

2.3 Secondary Ignition

Secondary ignition caused by smoldering or flaming firebrands is especially an issue in WUI fires under unfavorable wind conditions, which can subsequently spread from roof to roof, but also in wildland fires where travelling firebrands can significantly contribute to the fire spread [15].

Upon landing on the recipient fuel, the fuel is heated while the firebrand keeps cooling down [25]. To cause ignition, the fuel bed needs to be heated until it releases combustible volatiles that then mix with ambient air and are set alight by the hot particle acting as a pilot igniter [25].

Solids heated by an external source increase in temperature from the outside and the heat is then transferred through the body by conduction which makes it the main heat transfer mechanism in solids that is captured in Fourier's law [40]:

$$\dot{q}_x^{"} = -k \times \frac{dT}{dx} \tag{2-12}$$

With $\dot{q}_x^{"}$ being the heat flux in x-direction and, k being the thermal conductivity of the solid and $\frac{dT}{dx}$ being the temperature gradient over the thickness.

The temperature varying in space over the body of the solid determines the heat that is transferred through the same. This temperature gradient is more significant for some objects than for others as, for example, thin solids with a high thermal conductivity will almost have a uniform temperature and heat up almost instantaneously when exposed to a heat source. Thicker samples with low thermal conductivity, on the contrary, need longer times to reach a state of thermal equilibrium with no temperature gradients within the body. To quantify the varying characteristic of solids to heat up or cool down at certain pace, the concept of thermal inertia can be introduced. The thermal inertia ($k\rho c$) of a body is a bulk property of a material calculated as the product of the thermal conductivity, k, the density, ρ, and the heat capacity, c, that allows quick assessment of the thermal behaviour of a material and its capability to absorb and store heat [41].

Solids that heat up quickly and do not develop significant temperature differences throughout their body can be described as 'thermally thin', with the opposite consequently being 'thermally thick'. A mean to establish, whether an object can be regarded as the one or the other is the Biot number [42]:

$$Bi = \frac{L_c h}{k} \tag{2-13}$$

Where L_c is the characteristic length, usually taken as the (half-)thickness, and h is the convective heat transfer coefficient. Therefore, the Biot number is a ratio of the internal resistance of a body to the conduction of heat over the heat conduction resistance on the surface [42]. The Biot number indicates which process is dominating in the considered case and for high thermal conductivities and small length scales, the number becomes small and the resistances on the surface dominate. Solids are usually considered as thermally thin for Bi < 0.1 and as thermally thick for Bi > 0.1 since the Biot number becomes larger for low thermal conductivities and thicker objects, increasing the importance of internal resistance to heat conduction for the temperature of the body [42]. This boundary should be applied cautiously, however, as materials close to it might be of intermediate thermal thickness and neither completely follow typical behaviour patterns of thermally thick nor thermally thin solids and the thermal gradients within the body must be addressed in these cases, nonetheless [43].

Figure 6 schematically shows a comparison for resulting temperature profiles throughout a thermally thick and a thermally thin solid by an external heat source and how the temperature gradients in thermally thin materials are of negligible nature. The external heat source causes the surface temperature to rise on the exposed side. When the surface temperature reaches a certain threshold value, T_p, the material will start to thermally decompose and release combustible volatiles. Further increase in temperature after pyrolysis onset, shortly leads to reaching the flash point, T_{fp}, and the fire point, T_{FP}. As the time scales to get to the fire point and flash point and for mixing of the flammable gases with ambient air are very small compared to the time to reach pyrolysis, it is simpler to neglect them, which allows to define the ignition temperature of the solid as the pyrolysis temperature [44]:

$$T_{ig} = T_p \tag{2-14}$$

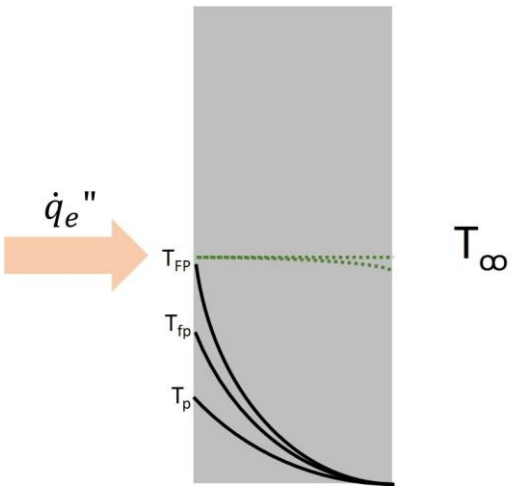

Figure 6: Resulting temperature profiles from an external heat flux within a thermally thick solid (black lines) in a thermally thin solid (green, dashed lines), based on a lecture by J.L. Torero.

This presentation is physically not perfectly accurate, but bears the perks of allowing for a single parameter to be characteristic for the ignition of a solid instead of having to take all micro time scales and temperature differences into account [43,44]. While the vast majority of combustible solids have relatively similar ignition temperatures, it becomes evident that the firstly presented characteristics of solids regarding their capabilities to absorb and transfer heat are representing the approach to the time scale of the ignition problems and are subsequently establishing the large diversity in ignitability of solids [41].

The above described mechanism for the ignition of solids and the attached characteristic properties and parameters give an overview of how complicated and detailed the phenomenon of spotting ignition really is. It is also possible that a particle might not cause flaming ignition right away, but that the fuel bed is put in a smoldering state first and transforms to flaming burning at a later stage [25]. Relevant factors with regard to the pilot ignitor particle are, on one side, its size, temperature and state upon landing, which includes the material it is made of and the attached properties and whether it is inert, smoldering or flaming [25]. On the other side, the recipient fuel and its characteristics such as fuel type, temperature, density, porosity and moisture content must be considered, along with the environmental boundary conditions such as weather and wind and landing characteristics (e.g. whether the particle is partially or fully embedded on the fuel bed) [25].

The latter cases, where the hot particles are partially or fully embedded within the fuel bed, enable different mechanisms to lead to ignition. Hadden et al. [45] conducted experimental work on the ignition of combustible fuel beds by inert hot metal spheres and employed comparison with hot spot ignition theory which showed good qualitative agreement with the experimental results, but quantitatively the theoretical results seem to be too conservative in their predictions. Moreover, a correlation between the size of a particle and the temperature required for flaming or smoldering ignition is reported [45]. Figure 7 shows the results for ignition of dry cellulose powder by hot metal spheres of different temperatures, where the regions of flaming and smoldering ignition are separated by two lines that can be described as [45]:

$$2r_{particle} = C_1 T_{particle} \sqrt{\left(\exp\left(\frac{C_2}{T_{particle}}\right)\right)} \qquad (2\text{-}15)$$

With C_1 being 0.0004 and 0.0011 m/K and C_2 being 4862 and 4264 K for smoldering and flaming ignition, respectively.

The minimum particle temperature to cause smoldering ignition was found to be 550 °C and minimum 650°C was required to cause flaming ignition, where both temperatures were observed for the largest particle diameter of 19.1 mm and generally, flaming was only reported for particles larger than 2.4 mm and heated to 1200 °C [45].

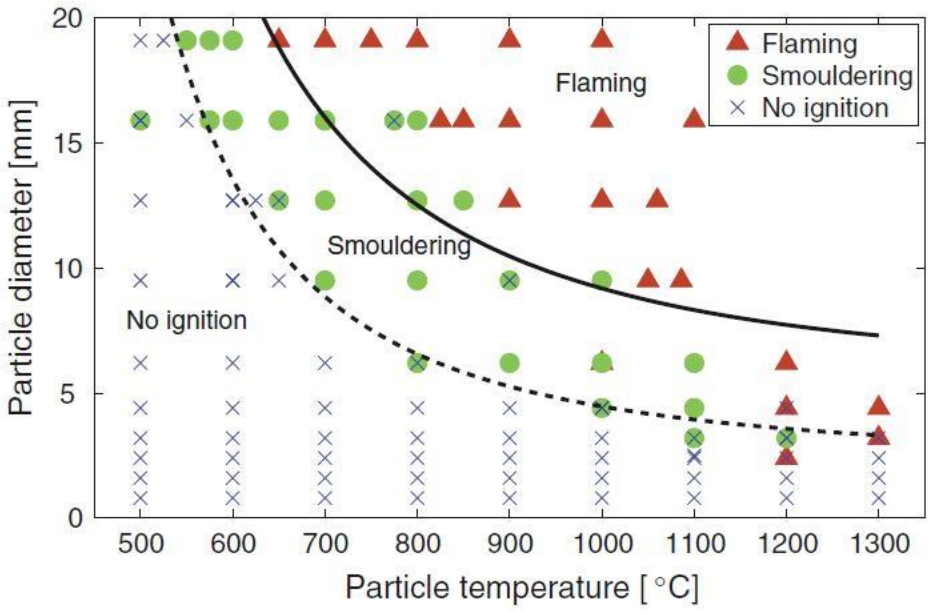

Figure 7: Ignition propensity of dry cellulose using heated steel spheres [45].

The form of Equation (2-15) was based on the theory for ignition from hot spots, where the critical hot spot radius can be calculated with the adequate thermophysical properties as follows [45]:

$$r_{cr} = \delta_{cr} \sqrt{\frac{k}{\rho A \Delta H} \frac{R T_{particle,0}^2}{E} \exp\left(\frac{E}{R T_{particle,0}}\right)} \qquad (2\text{-}16)$$

The Equation (2-16) for the critical radius is derived from the Frank-Kamenetskii hot spot parameter defined as in Equation (2-17) [45], a form of the dimensionless heat generation rate, δ, which is defined in the Frank-Kamenetskii theory to analyse spontaneous ignition and the onset of thermal runaway [46]. The parameter represents the energy balance between heat generation and heat loss of a material and usually indicates the capability of a material to undergo ignition when the heat generation, or in this application the heat transferred from the hot spot into the material and subsequent generated heat from exothermic thermal degradation of the material, exceeds the losses [38]. However, ignition does not occur before a critical value for the Frank-Kamenetskii parameter is reached, otherwise the process will be limited to the partial thermal decomposition of the material (subcritical self-heating) [38]. In the described experimental study, a correlation found by Gol'dshlegler et al. [47] from fitting their numerical results from research on secondary ignition by hot objects is employed to determine the critical value δ_{cr}. The result for the ignition from a hot particle as a function of the particle temperature and size is shown in Figure 8.

$$\delta = r \sqrt{\frac{\rho A \Delta H}{k} \frac{E}{R T_{p0}^2} \exp\left(-\frac{E}{R T_{p0}}\right)} \qquad (2\text{-}17)$$

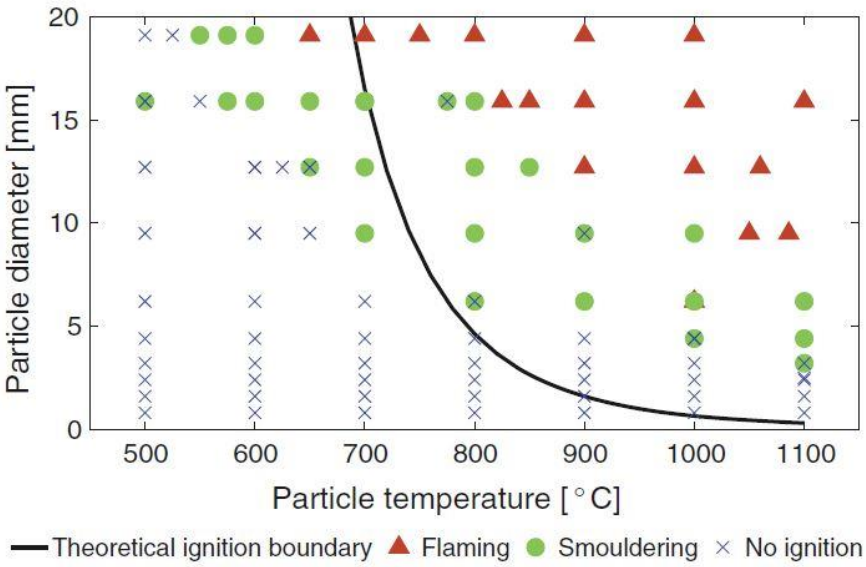

Figure 8: Comparison of experimental data with hot spot theory (Equation (2-16)) [45].

Even though the theoretical prediction does not meet the experimental results quantitatively, the qualitative trend of the theoretical derived correlation matches the observed behaviour, which makes this kind of analysis of the problem to a promising approach to assess the problem. The discrepancies may also partially be devoted to the fact that flaming ignition might differ from thermal runaway in the hot spot theory, which also assumes fully embedded particles, whereas particles in the experimental study were sometimes rather sitting on top of the fuel bed [45].

Other current research towards the problem of secondary ignition is nearly completely of an experimental nature and predictive theory models still need to be developed from these. Numerous experiments are, for example, conducted under the use of a firebrand generator developed by the National Institute of Standards and Technology (NIST) [12], which resulted, for instance, in the quantification of the necessary firebrand mass load for sustained ignition of wood boards as they are built in on patio floors [48]. Another study adresses the investigation of the hazard that mulch beds pose in outdoor fire problems as they are easily ignited by firebrands and further ignite adjacent structures [49]. From a set of experiments that used different materials of fuel beds (shredded paper, pine needles and cedar crevices) it became evident that ignition is more likely with increasing firebrand size, an increased number of firebrands landing on the same fuel bed and it also depends on the material properties and moisture content [50].

2.4 Pyrolysis and Oxidation of Firebrands

The combustion of firebrands is an important part of the transportation problem as major characteristics influencing the transport equations presented in chapter 2.2 in the equations *(2-2)* to *(2-11)*, such as mass, density and geometrical dimensions change with time while the particle is in mid-flight.

The basic concept of pyrolysis has been explained in the previous chapter discussing secondary ignition. In a simplification of the problem, the ignition temperature for a solid is there defined as the onset temperature of pyrolysis.

$$Solid + Heat \rightarrow Products$$
$$A + B \rightarrow Products \qquad (2\text{-}18)$$

The pyrolysis rates or reaction rates in general for a simple reaction as shown in Equation (2-18) [41] can be described by Arrhenius reaction equations as functions of the temperature [43]:

$$\dot{\omega} = A \times Y_O^m \times Y_s^n \times \exp\left(-\frac{E}{RT}\right) \quad ; \quad Y_s = \frac{\rho_s}{\rho_{s,0}} \qquad (2\text{-}19)$$

Where Y_s^n is representing the solid fuel mass fraction participating in the degradation of the solid, with n being an experimentally obtained constant that are usually taken as 1 [43]. Y_O^m is a term in Arrhenius equations that is usually only regarded for oxidation reactions as it represents the oxygen mass fraction that is available on the surface and m is therefore usually taken as 0 for pyrolysis reactions [43]. A is the pre-exponential factor in units of invert seconds ([1/s]) and E is the activation energy. Both values are specific for each reaction and must usually be obtained from Thermo-Gravimetric Analysis (TGA). R is the ideal gas constant and has a value of $8.314 \times 10^{-3}\ kJ\ mol^{-1}K^{-1}$ [43].

In TGA experiments, a small sample size (5-10 mg) of a material is heated at rates between 1-20 K/min [51]. The small sample size and the slow heating rates ensure that the specimen is in thermal equilibrium with the conditions prescribed by the apparatus. During the test, the mass of the specimen is recorded and the mass loss as a function of the temperature can be derived. As a result, the kinetic parameters to estimate the reaction rates of thermal degradation and decomposition of a single material can be determined. These processes do not necessarily only involve a single step.

The production of gaseous fuel is essential before flaming ignition can occur and it has been established that the thermal decomposition of a solid material is a function of the temperature, but also of the oxygen concentration that controls the level of oxidation of the gaseous pyrolysis

products (GPP), which range from fully oxidized gases (CO_2), over partially oxidized products (CO), to fuel gases (CO, CH_4, H_2) and inert gases like water vapor [43].

In wildland fires, it is often wood or organic, vegetative material that needs to be considered as solid fuel and it tends to create a char layer from pyrolysis [52]. Figure 9 visually explains the concept of pyrolysis for vegetative fuels whose decomposition is generally represented by a simplified 3-step reaction mechanism, where mass and density is reduced by pyrolysis but the volume of the solid only reduces from surface oxidation [52]:

1. Endothermic drying of wet wildland fuel matter (WWF) to dry wildland fuel matter (DWF):

$$WWF \rightarrow v_{H_2O} H_2O + \left(1 - v_{H_2O}\right) DWF \qquad (2\text{-}20)$$

2. Endothermic pyrolysis:

$$DWF \rightarrow v_{char} Char + (1 - v_{char})(GPP + Soot) \qquad (2\text{-}21)$$

3. Exothermic char oxidation:

$$Char + sO_2 \rightarrow (1 + s - v_{ash}) CO_2 + v_{ash} Ash \qquad (2\text{-}22)$$

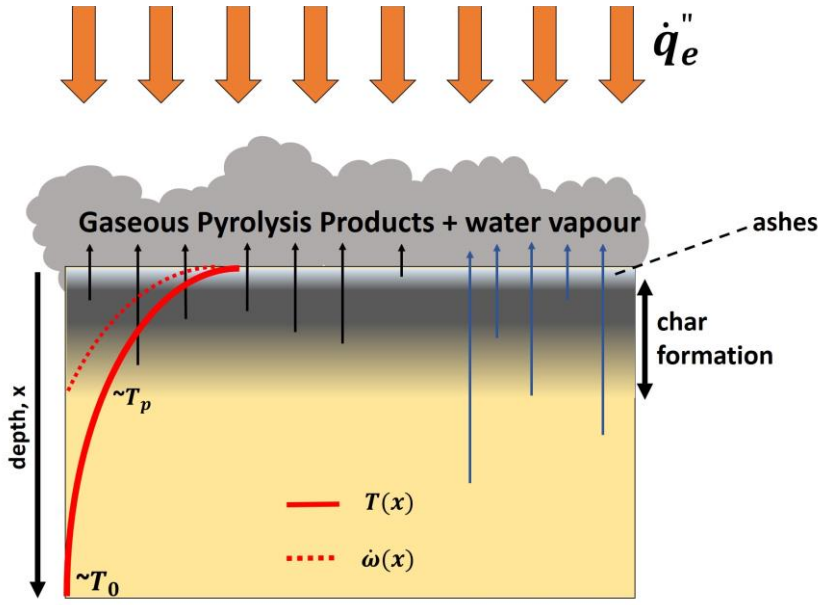

Figure 9: Schematic for the simplified representation of pyrolysis of a solid material exposed to an external heat source. (not to scale; after [43])

With increasing temperature and depth the quantities of fuel gas that emerges as part of the GPP increases as well [43]. By mixing with ambient oxidizer (usually the oxygen in ambient air), the gaseous fuel can create a flammable atmosphere when the concentrations fall within the flammability limits of the mixture. The mixing process and the resulting fuel distribution within the gas phase is complex to describe as it is established by the flow pattern of the ambient gases resulting from the flames and the geometry of the environment and it is usually

best to be measured or modelled [43]. Once a flammable mixture has formed it can either be ignited by pilot ignition or if the ambient temperature is sufficiently high, auto-ignition might occur. The resulting flame will cause a heat feedback towards the surface of the solid increasing the pyrolysis rates. If those rates are sufficiently high to maintain a certain level of gaseous fuel supply, sustained burning can be observed. Otherwise, it might come to a series of flashes originating from flammable mixtures that are formed and consumed, formed and consumed again and so on, before the pyrolysis rate has been increased to a level that allows for sustained burning [43].

The latter description of this phenomenon might at first leave a contradictory impression to the simplification that is made in the previous chapter, where the ignition temperature of a solid was simplified as the pyrolysis temperature and the time scales to reach the flash and fire point of the material are neglected. It is now evident, that this is a conservative simplification to the problem, but also that the onset of pyrolysis enables sustained burning to occur depending on further boundary conditions. Therefore, it seems justified in most practical cases to make this simplification as it allows to take a single property to be responsible of ignition in the hazard assessment of materials rather than having to assess specific setups and attached boundary conditions to each problem.

Pyrolysis results in gaseous and solid products, whereas the char as well as the GPP that are formed can subsequently be oxidized in exothermic combustion processes [53]. The combustion/oxidation of fuel gas is not explicitly stated as a mechanism step occurring simultaneously to char oxidation (Equation (2-22)) in the above pyrolysis description it follows the following pattern [53]:

$$GPP + O_2 \rightarrow Heat + CO_2 + H_2O + other\ gases \qquad (2\text{-}23)$$

Heterogenous char oxidation (see Equation (2-21)) occurs, where the solid char layer, which consists for forest fuel matter of almost pure carbon [52], reacts with the ambient gaseous oxygen releasing heat and forming ash, a final solid residue that is high in mineral content and of negligible reactivity [53]. Figure 10 shows schematically how a solid body is first pyrolyzed and how the formed char layer is later oxidized on the outside, where it can come in contact with ambient oxygen and how with time a new layer forms (ashes) as the material is burnt away by smoldering, oxidation is still possible where the oxygen can penetrate through the porous ashes into the solid. However, the process requires sufficiently high temperatures or activation energies and is hard to suppress once initiated and it is thus controlled by the oxygen supply and the heat transfer [53]. Whether now flaming or smoldering combustion occurs, depends on where the oxidation takes place. Flaming combustion occurs for oxidation in the gas phase and smoldering combustion occurs when the solid material is being oxidized [53]

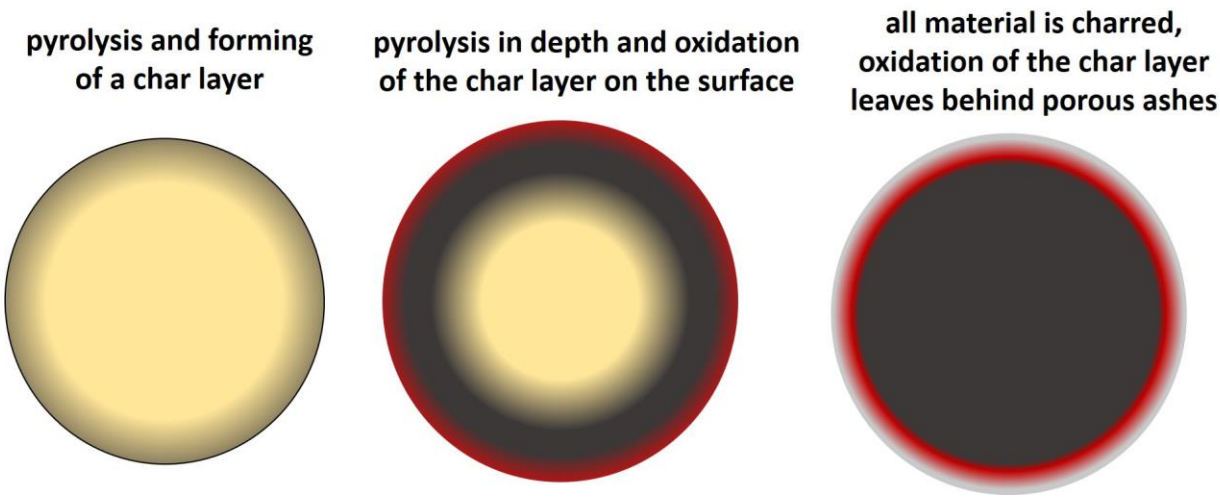

Figure 10: Schematic of the process of char oxidation.

In the case of firebrands, char oxidation, also referred to as surface combustion, occurs when the flaming combustion is stopped either because the particle has undergone pyrolysis over its entire depth and no more fuel gas is being released from the process or because the flame is (partially) quenched due to wind or the velocity of the particle [34]. Woycheese [34] describes the controlled burning of over 500 disc-shaped particles under different wind conditions and finds that surface combustion is dominant for less dense wood types, where the same would self-extinguish for denser species when the flame from the combustion of the gaseous phase was not near to supply heat to the reaction. Moreover, he describes how low-density woods tend to burn to completion unlike their counterparts and firebrands of higher density showed longer flaming combustion but would have significant higher mass residues in the end [34]. Lastly, increasing wind velocities will be unfavorable for sustained flames but increase surface combustion once it has been established prior to the extinguishing of the flame [34].

Tarifa [16] reports that the times for a firebrand to burn to completion decrease with constant wind velocities, where the loss in volume shows two distinct zones where the first is a slow loss rate followed by a steep linear loss rate. The time span of the slow loss rate, before the more sudden volume loss is observed, decreases with increased wind speeds [16] which substantiates the assumption of flaming combustion and surface combustion (char oxidation) occurring in sequence as the flaming combustion is being suppressed by high wind speeds. This is consistent with the observations by Woycheese that are mentioned above.

From the results of experiments by Muraszew [54], where numerous cylindrical firebrands were burned under different wind conditions and initial and final values for mass and density of the specimen are reported for changing burning times, Albini [11] developed a burning rate model. The model gives the fractional loss of thickness multiplied with the density of firebrands as a function of the density and velocity of the ambient gases and the burning time of the particle over the initial properties of the ember [11]:

$$y = bx \tag{2-24}$$

with

$$y = 1 - \frac{\left(\rho_f D\right)_t}{\left(\rho_f D\right)_0} \tag{2-25}$$

and

$$x = \frac{\rho_{air} u_{wind} t}{\left(\rho_f D\right)_0} \tag{2-26}$$

The variable y was established from the square root of the ratio of the product of mass times density after and before burning as the diameter was not measured for most samples [11]:

$$y = 1 - \sqrt{\frac{(\rho_f M)_t}{(\rho_f M)_0}} \tag{2-27}$$

Albini plotted both variables against each other and obtained a regression variable of $b = K = 0.0064$ from the graph shown in Figure 11. The scatter in the data was partially explained with samples that did not burn to completion leaving behind much larger final values for the density and mass. Moreover, some samples burnt through, and parts were blown away by wind giving much lower values for the final mass, but not for the density. As faulty measurements included in the reported data by Muraszew (if any) were not flagged, the model is based on all reported experiments and therefore bears uncertainty in its derivation from varying data [11].

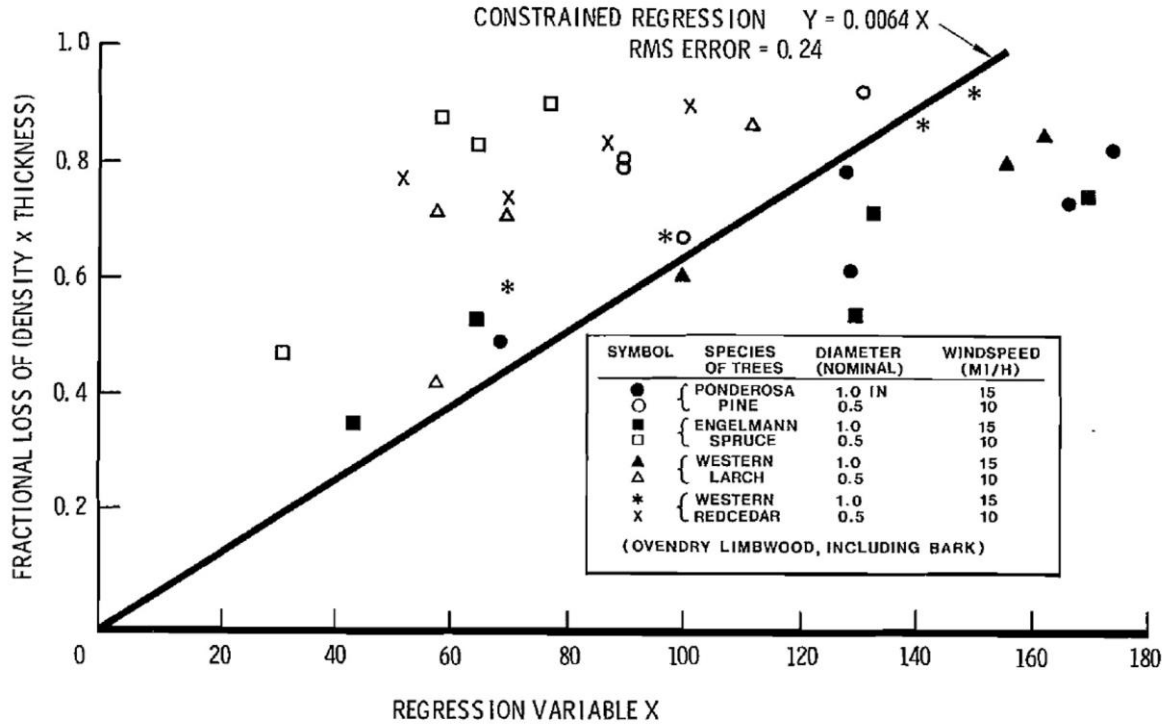

Figure 11: Data used by Albini to establish a firebrand burning rate model [11].

This burning model offers an easy approach that can be solved by hand calculations to the problem of the pyrolysis and oxidation of firebrands over time. The mass (thickness) and density over burning time and depending on environmental conditions can be established quickly, which is beneficial as these properties are important to subsequently analyse the trajectories of the firebrands that depend on the mass and geometry of the particles. This model can be used to predict the relevant instantaneous properties of the firebrands, which otherwise need to be established by solving the heat transfer around and within the particle and the reaction kinetics of the thermal degradation processes. However, one should be aware of the limitations concerning the wind speeds and particle sizes this model was derived for and also the uncertainty it bears due to its derivation from data that might include single faulty measurements. Furthermore, it represents a vast simplification to the problem of the degradation of solids as it linearizes the otherwise complex problem of two simultaneously, or actually sequentially, occurring different combustion processes and takes no thermophysical properties of the solid into account. Thus, the model should be applied to solids similar to those tested in the experiments it was established from.

3 Numerical Modelling of the Transport of Reacting Firebrands

The problem of the transportation of reacting firebrands is to be modelled using a computational fluid dynamics (CFD). The approach to CFD is to obtain a complete, time-dependent and three-dimensional solution of the fundamental governing conservation equations for a defined volume. In the process, the volume is subdivided into smaller volumes, so called cells, to which subsequently the basic laws of mass, momentum and energy conservation are applied [40]. The solver that is used in this work is the Fire Dynamics Simulator (FDS), which is a Lage Eddy Simulation (LES) solver suitable for low Mach number flows, i.e., flow velocities that are much lower than the speed of sound which is the case for most fire induced flows but not necessarily when explosions are involved [55]. In the following a short description of relevant information on CFD modelling is given, but the discussion and detailed explanation of the modelling of flows using CFD is beyond the scope of this work and the interested reader is referred to the cited literature for more information. For detailed descriptions of the solved governing conservation equations in FDS the reader is directed to [56].

One main difference between most CFD codes is the treatment of turbulence, which emerges from flows becoming unstable when exceeding a certain Reynolds number introducing velocity fluctuations and turbulent eddies (rotational flow structures) and additional Reynolds stresses on the fluid [40]. These fluctuations can occur very fast and at high frequencies with length scales of the order of µm [40] and thus very fine meshes are needed to represent a subdivision of a computational domain that can capture all these phenomena. The larger scales for length, time and velocity are called “integral scales” and are of the same order of magnitude as the geometry (for length scales) and mean flow (for velocity and time scales), while the integral scale range also carries most of the turbulent kinetic energy [55]. The smallest scales, on the contrary, are the ‘Kolmogorov scales’ where the turbulence is dissipated. Eddies of larger sizes break up into smaller eddies and then even smaller eddies, until reaching a size so small that they dissipate from the damping actions of viscosity, while only little energy is dissipated in the break-up process(es) [55]. There are different approaches on how the turbulence of fluid flows can be modelled and the computationally most expensive one is Direct Numerical Simulation (DNS), where all time and length scales of the turbulent flows are resolved and therefore, a very fine computational grid and small time steps are necessary to obtain a direct solution [57]. Much less expensive than DNS is the approach of (LES), which takes advantage of the fact, that most of the energy is transported on the integral scales [57]. Only large eddies that are at least the size of the cells of the computational domain are considered, by applying filters on the velocity field [57]. However, as the energy transported on smaller scales cannot be unaccounted for, subgrid scale models (SGS models) are introduced to represent phenomena smaller than the cell size in the conservation equations. Lastly, the approach with the lowest computational cost is by time averaging relevant parameters over the unsteadiness and

turbulence which generates new terms in the conservation equations and to close the system of equations, sub-models represented by engineering correlations are introduced [57]. However, those Reynolds Averaged Navier-Stokes (RANS) equations also bear the least accurate solution to complex problems.

Figure 12 shows schematically the modelling approaches of DNS, LES and RANS models.

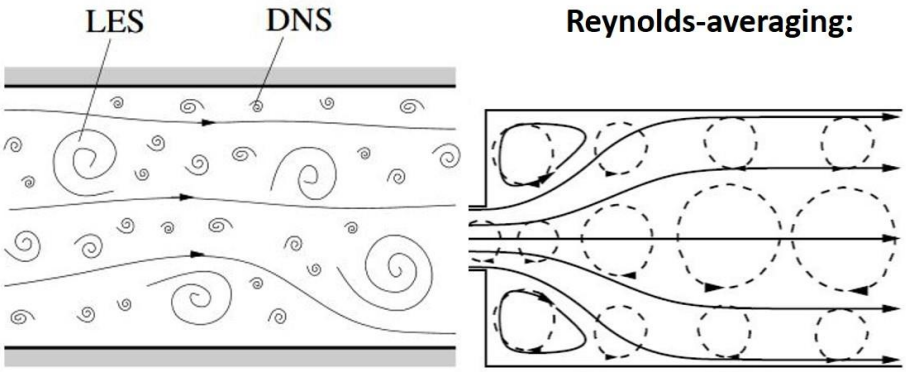

Figure 12: Schematic of the approaches for LES, DNS [57] and RANS [58] in turbulence modelling.

The model that is described in the following sections is based on work describing the develepoment of a numerical model for combusting particles by Sardoy et al. in 2007 [39], where the transport of firebrands from burning trees is investigated (see Figure 13). FDS v6.7.0 is used to develop a similar model and analyze the transportation of firebrands in dependence of different firebrand properties.

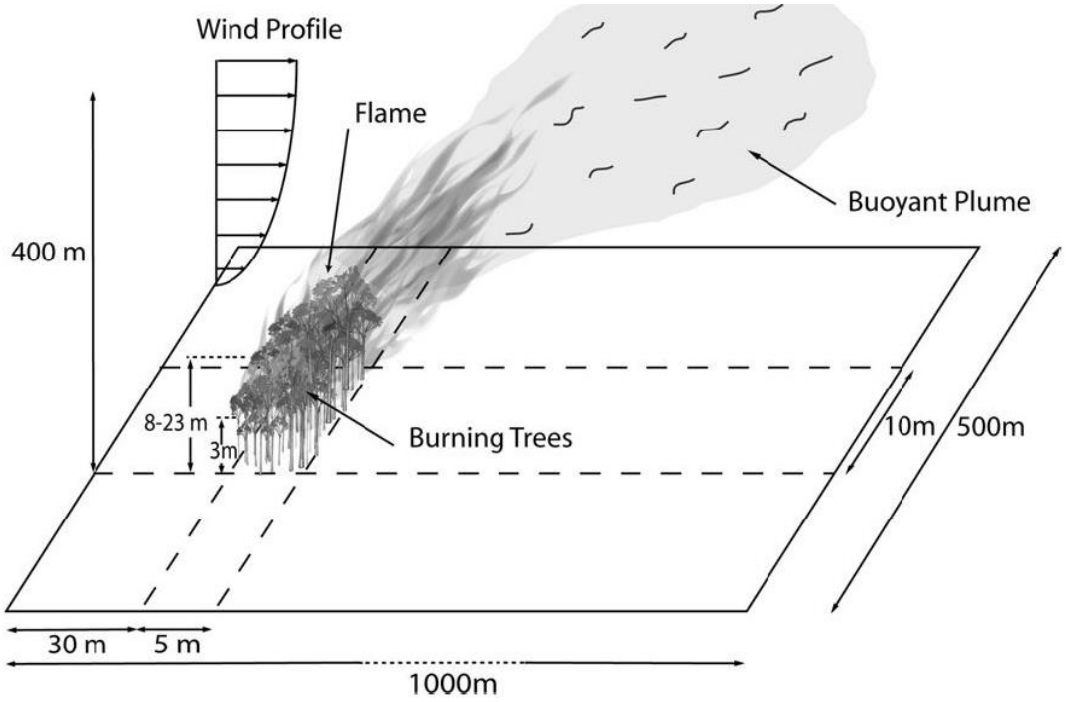

Figure 13: Schematic of the physical problem, computational domain, and coordinate system used in the analysis by Sardoy et al.[39]. (not to scale)

The choice to use the Fire Dynamics Simulator to model the firebrand trajectories sometimes limits the control that can be taken over submodels calculations. The following sections explain the choices that were made to model the problem of the transport of reacting firebrands in large fires and how the different mechanisms are invoked and treated in FDS. Comparison to the implementation in [39] are included where appropriate as the results from both models shall be comparable to each other. This includes discussions on the treatment of particles in the flow, the computational domain, the fire source and the resulting plume, the pyrolysis and char oxidation mechanisms, the combustion of fuel gases and the boundary conditions such as wind and temperature profiles of the atmosphere. Relevant parts of the FDS input file may be discussed or displayed in the respective subsection, the entire input file can be found in the appendix of this manuscript.

3.1 Firebrand Modelling

In FDS, firebrands can be represented by solid particles. An Eulerian-Lagrangian model is used by FDS for those cases. The gas phase is calculated from an Eulerian approach and the solid particles are tracked with an Lagrangian approach within the fluid. The difference between the two frameworks lies in the philosophy that a fluid or element of a fluid is treated with. In the Lagrangian approach, a specific element is considered that passes through the flow and the physical variables for that element are described, whereas the Eulerian treatment of a fluid governs the physical properties of locations within the considered space, while a fluid flows through that space [59].

Particles in FDS can be tracked on a subgrid-scale and can be assigned thermophysical properties to represent solids within the flow field. The momentum transferred from particles to the gas is integrated in the gas phase momentum equation and obtained by summing the force transferred from each particle in a grid cell and dividing by the volume of the cell [56]:

$$f_b = \frac{1}{V}\sum\left[\frac{\rho}{2}C_d A_{cs}(V_P - V_g)|V_p - V_g| - \frac{dm_p}{dt}(V_p - V_g)\right] \qquad (3\text{-}1)$$

The particle acceleration and position are determined from the formulations in *(2-6)* to *(2-11)*. The same formulations are used in Sardoy et al. [39].

The drag coefficient, C_d, is calculated in FDS from drag laws or the coefficient can be defined explicitly overriding the calculation procedures. The default drag law that is invoked is that for spherical objects:

$$C_d = \begin{cases} \dfrac{24}{Re_D} & Re_D < 1 \\ \dfrac{24(0.85 + 0.15Re_D^{0.687})}{Re_D} & 1 < Re_D < 1000 \\ 0.44 & 1000 > Re_D \end{cases} \qquad (3\text{-}2)$$

Sardoy et al. [39] consider disc-shaped particles that are released in an incidence angle of 145°. The drag coefficient for that case is calculated from the drag coefficient for an angle of attack of 90° which is defined in the paper as [39]:

$$c_D(90) = 1.98 - 0.821\left(1 - \exp\left(-\frac{20}{\eta}\right)\right) \qquad (3\text{-}3)$$

Particles in FDS can be assigned spherical, cylindrical or cartesian geometries but the incidence angle cannot be controlled. The relevant input lines for defining firebrands in their geometry and property are shown in Figure 22 after discussing pyrolysis and combustion which are attached to those inputs.

In LES calculations with FDS and in Sardoy et al. [39] the convective heat transfer to solids takes particle geometries into account and is captured as follows [56]:

$$\dot{q}_c^{"} = h\left(T_g - T_k\right)\left[\frac{W}{m^2}\right] \;\; ; \;\; h = \max\left[C\left|T_g - T_s\right|^{\frac{1}{3}}, \frac{k}{L}Nu, \frac{k}{\frac{\delta n}{2}}\right]\left[\frac{W}{m^2 K}\right] \qquad (3\text{-}4)$$

$$Nu = C_1 + C_2 Re^n \mathrm{Pr}^m \;\; ; \;\; Re = \frac{\rho|u|L}{\mu} \;\; ; \;\; Pr = 0.7 \qquad (3\text{-}5)$$

The constants used in the calculations of the heat transfer coefficient are partially experimental values and depend on the particle geometry and configuration. They can be found in the respective literature for Sardoy et al. [39] and FDS [56].

FDS considers one dimensional heat conduction for the solid phase, which is in compliance with the assumptions in [39], in the direction normal to the surface into the solid for cartesian elements as follows [56]:

$$\rho_s c_s \frac{\partial T_s}{\partial t} = \frac{\partial}{\partial x}\left(k_s \frac{\partial T_s}{\partial x}\right) + \dot{q}_s''' \;\; ; \;\; \dot{q}_s''' = \dot{q}_{s,c}''' + \dot{q}_{s,r}''' \qquad (3\text{-}6)$$

where $\dot{q}_{s,c}'''$ and $\dot{q}_{s,r}'''$ are essentially the heat production (loss) rate by pyrolysis and the radiative absorption, respectively.

The thermal radiation from surrounding gases is stored in the surface of the solid in FDS for opaque objects like firebrands and the net radiative heat flux is calculated as [56]:

$$\dot{q}_r'' = \dot{q}_{r,in}'' - \dot{q}_{r,out}'' \tag{3-7}$$

with

$$\dot{q}_{r,in}'' = \varepsilon \int_{s' \cdot n_s < 0} I_s(s') \, |s' \cdot n_s| \, d\Omega \tag{3-8}$$

$$\dot{q}_{r,out}'' = \varepsilon \sigma T_s^4 \tag{3-9}$$

3.2 Computational Domain

The computational domain is derived from the expected trajectories of the firebrands. The trajectories are influenced by many factors, but the most important input variable to distinguish different cases is the intensity of the fire. Sardoy et al. consider two different fire scenarios in their analysis, where the smaller fire represents burning tree crowns over a region of 5 m x 10 m x 5 m with an intensity of 10 MW/m over the width of 10 meters and the larger fire is derived from burning tree crowns of 5 m x 10 m x 20 m with an intensity of 40 MW/m over the same width.

With regard to the computational cost of the simulation, that increases with the size of the computational domain when the mesh resolution is not lowered, it was chosen to model only the case of the smaller line fire that has a total intensity of 100 MW. The maximum height and distance that firebrands travelled in the X and Y direction (see Figure 14) are therefore expected to be around 120 m, 680m and $\pm$140 m, respectively at a crosswind speed of 6.7 m/s [39]. The computational domain was fitted to the needs derived from these numbers at first, but later results have shown that the particles had longer flight paths in the X direction and as a results, the domain was extended to 1000 m in this direction. The dimensions are shown in the schematic of the domain in Figure 14. To avoid confusion for the reader, the difference in the coordinate system between the model by [39] and the work of this manuscript is emphasized at this point (see Figure 13 and Figure 14Figure 14).

To make the model more efficient, the domain is subdivided into several meshes with cubic cells and changing resolution. The finest resolution with an edge size of 0.5 m is applied to the region of the fire source to span at least 10 grid cells over this characteristic area ($\Delta x = 5\,m$). As a result, the area in which the fire is introduced is spanned by 10, 20 and 10 cells in the X, Y and Z direction, respectively, which adds up to 2,000 cells in total. In order to analyse the mesh resolution, a grid independence study is carried out for the plume model described below

to confirm whether that resolution is sufficient to capture the details of the dynamics in the fire plume and accurately represent it.

From the region with the finest mesh (colored red in Figure 14), the meshes are getting coarser with distance to the fire and each new color in Figure 14 represents a new class of meshes where the edge size from the previous resolution is doubled. The coarsest grid, where the cells feature an edge size of 4 m, is assigned to the regions that are represented blue in Figure 14. The total number of grid cells from all meshes is 1,500,800.

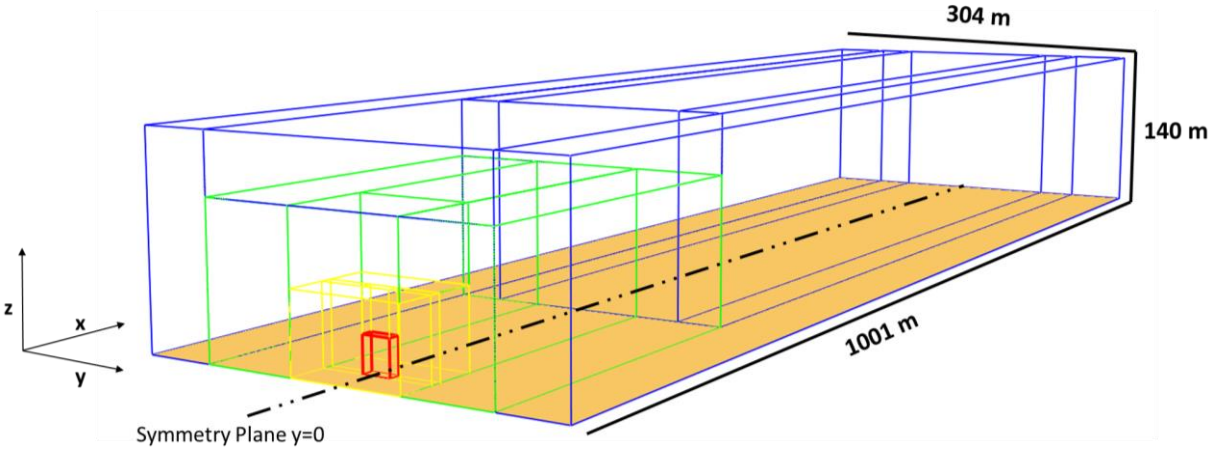

Figure 14: Screenshot of the computational domain in FDS, visualized in Smokeview (not to scale).

3.3 Fire Model

The fire spans a region of 5 m x 10 m x 5 m with an intensity of 10 MW/m. The total heat release rate of the fire is hence prescribed with 100 MW.

To get close to the actual conditions of burning vegetation, the fire is controlled by small particles representing vegetative material that release a constant mass loss rate per unit area (MLRPUA) of the gaseous pyrolysis product (GPP) into the domain.

This process shall mimic a simple, single-step endothermic pyrolysis reaction [39]:

$$DWF \rightarrow v_k^{char} Char_k + \left(1 - v_k^{char}\right) \times \left[(1 - v_k^{soot}) GPP_k + v_k^{soot} Soot\right] \qquad (3\text{-}10)$$

Where

$$GPP_k = \alpha_k^{CO} CO + \left(1 - \alpha_k^{CO}\right) CO_2 \qquad (3\text{-}11)$$

v_k^{char} is taken as 0.3, α_k^{CO} as 1 [39] and the formation of soot is not considered until the combustion of the GPP. The pyrolysis products, such as carbon monoxide, carbon dioxide, methane, hydrogen and others, are dependent on the fuel and the temperature and are therefore very hard to predict [39]. To simplify this problem, carbon monoxide is considered as the combustible gas in the GPP as it is the most prominent of the pyrolysis products and since the

deviation in resulting temperatures does not exceed 4 % for other representative combustible mixtures of seven components [39,60].

The particles that represent the vegetation are of cylindrical shape and have a length of 0.3 m and a radius of 0.400534 mm and can be regarded as long pine needles. The dimensions are derived from the values that are reported for the fire model by Sardoy et al., who state the volume fraction of solid material to be 2.44×10^{-4} over the region of the fire and the surface-to-volume ratio, σ_k, with $5000\ m^{-1}$ [39].

As a result, the volume of all solid vegetative material, V_k, over the tree crowns that occupy 250 m³ and the surface area, S_k, of the same are 0.61 m³ and 3050 m², respectively.

The total HRR of the fire is desired to be 100 MW, with the heat of combustion of 10,100 kJ/kg for carbon monoxide [61], the corresponding mass loss rate (MLR) can be calculated from [40]

$$\dot{Q} = \dot{m} \times \Delta H_c \tag{3-12}$$

$$\dot{m} = \frac{100{,}000\ kW}{10{,}100 \frac{kJ}{kg}} = 9.9009 \frac{kg}{s} \tag{3-13}$$

Subsequently, the MLRPUA is determined to be

$$\dot{m}'' = \frac{\dot{m}}{S_k} = \frac{9.9009 \frac{kg}{s}}{3050\ m^2} = 0.0032462 \frac{kg}{m^2 s} \tag{3-14}$$

The total number of particles that are necessary to meet the MLR of fuel to get to the prescribed fire intensity can be derived from the surface area of a single cylindrical pine needle and the total surface area of the vegetation, S_k. A total of 4,034,000 particles are introduced into the model in the 2,000 grid cells spanning the volume of the tree crowns. To reduce the computational cost, actually only 2,000 particles (one per cell) are visualized and simulated in the model with each particle representing 2,017 smaller pine needles.

The actual formation of char is not considered in the model as the decomposition of the solid fuel is not of interest for the scope of this work at this part of the model, but the fire is just a mean to obtain a fire plume with the proper characteristics to later model the firebrand transport. The formation of soot is accounted for in the combustion of the fuel gases and the soot yield is calculated corresponding to the ratio in which soot was produced to GPP in equation (3-10). This simplification is introduced as the particles would otherwise need to be modelled with an extended pyrolysis model, which is not necessary to meet the required representation of this fire source.

The ratio is calculated as

$$Soot\ Yield = \frac{(1-\alpha_{char})\alpha_{soot}}{(1-\alpha_{char})(1-\alpha_{soot})} = \frac{0.61 \times 0.03}{0.61 \times 0.97} = 0.0309278 \qquad (3\text{-}15)$$

Figure 15 shows the relevant FDS input that describes the fire for the considered case.

```
&REAC   FUEL = 'CARBON MONOXIDE',
        SOOT_YIELD = 0.03092783505,
        CO_YIELD = 0.000,
        C = 1,
        H = 0,
        O = 1,
        HEAT_OF_COMBUSTION=10100./

&PART   ID='pine needles',
        SAMPLING_FACTOR=1,
        SURF_ID='vegetation',
        PROP_ID='needle image',
        STATIC=.TRUE. /

&INIT   PART_ID='pine needles',
        XB=30.001,34.999,-4.999,4.999,3.001,7.999,
        N_PARTICLES_PER_CELL=1,
        PARTICLE_WEIGHT_FACTOR=2017/

&SURF   ID = 'vegetation',
        MLRPUA = 0.00324622626197,
        MATL_ID = 'NEEDLE',
        THICKNESS = 0.000400534,
        LENGTH = 0.3,
        GEOMETRY = 'CYLINDRICAL' /
```

Figure 15: FDS input lines prescribing the fire.

To check the plausibility of the calculated plume, analytical solutions in the form of established engineering correlations are employed to calculate the theoretical centerline velocity and temperature and the mean flame height.

The flame height is visually obtained from FDS by adding colored thin and inert obstacles behind the flame which allow a visual estimate of the flame height in steps of 0.5 m (see Figure 16). The theoretical mean flame heights, defined as the height at which the flame can be observed at 50 % of the time, is obtained from correlations given by Heskestad derived from pool fire experiments and by Yuan and Cox for line fires.

The mean flame height after Heskestad is calculated as [62]:

$$L_f = 0.235\dot{Q}^{\frac{2}{5}} - 1.02D \qquad (3\text{-}16)$$

The heat release rate is known to be 100,000 kW and the diameter is calculated as the corresponding diameter to the base area of the fire:

$$A = 5 \times 10\ m^2 = 50\ m^2 \qquad (3\text{-}17)$$

$$A = \pi r^2 \qquad (3\text{-}18)$$

$$r = \sqrt{\frac{50}{\pi}} = \frac{D}{2} \qquad (3\text{-}19)$$

$$L_f = 0.235 \times 100{,}000^{\frac{2}{5}} - 1.02 \times 2 \times \sqrt{\frac{50}{\pi}} = 15.362\ m \qquad (3\text{-}20)$$

The flame height after Yuan and Cox is calculated as [63]:

$$L_f = 0.034 \dot{Q}_l^{2/3} = 15.781\ m \qquad (3\text{-}21)$$

Where $\dot{Q}_l$ is the heat release rate per unit length in kW/m.

The theoretical mean flame height after Heskestad of 15.36 m is about 4 m (~40 %) higher than what can be observed for the flame as calculated in FDS (Figure 16), while the correlation given by Yuan and Cox gives about 43% higher results.

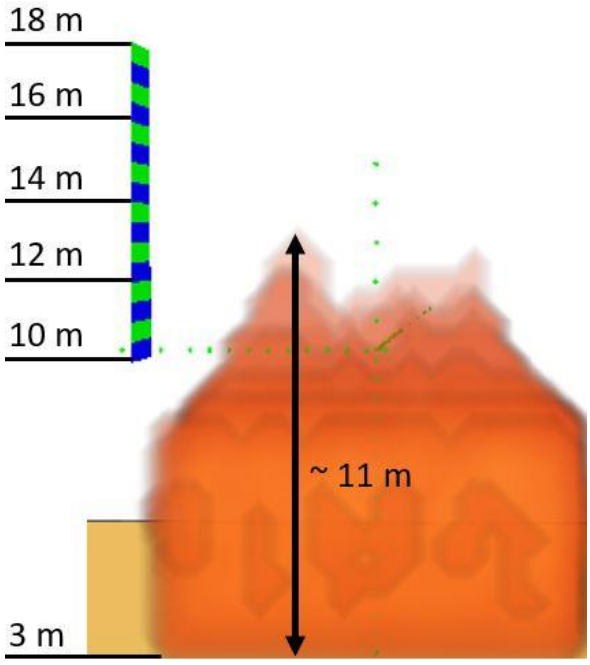

Figure 16: Flame height visualized in Smokeview (FDS).

The centerline temperature and the centerline velocity of the plume calculated by FDS are compared to the analytical solutions of engineering correlations derived by Heskestad and McCaffrey from pool fires [62] and Yuan and Cox [63] who present a set of correlations for line fires. Heskestad uses a concept of a virtual origin (see Figure 17) for his calculations and for ambient conditions ($T_\infty = 293K, \rho_\infty = 1.2\frac{kg}{m^3}, c_p = 1\frac{kJ}{kg\,K}, g = 9.81\frac{m}{s^2}$), the following forms of the correlations apply [62]:

$$\Delta T = 25 \times \left(\frac{\dot{Q}_c^{\frac{2}{5}}}{(z - z_0)} \right)^{\frac{5}{3}} \qquad (3\text{-}22)$$

$$u_0 = 1.0 \times \left(\frac{\dot{Q}_c}{(z - z_0)}\right)^{\frac{1}{3}} \quad (3\text{-}23)$$

With

$$z_0 = 0.083\dot{Q}^{\frac{2}{5}} - 1.02D \text{ and } \dot{Q}_c = (1 - X_r)\dot{Q} \quad (3\text{-}24)$$

X_r is the radiative fraction of the HRR, this value ranges usually between 20% and 40% [62]. In this case $X_r = 0.3$ is considered. Moreover, it must be mentioned that the equations are only valid for the plume above the mean flame height as it was calculated above [62].

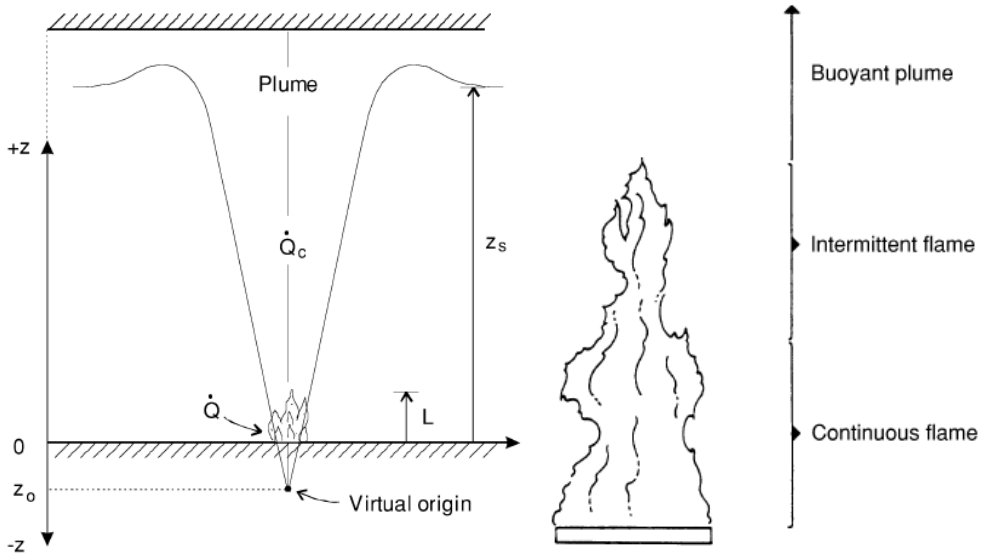

Figure 17: Schematic of the Heskestad plume (left) and the McCaffrey Plume (right) [62].

McCaffrey and Yuan & Cox distinguish three different plume zones (see Figure 17) [62,63]. Depending on the zone that is considered, the parameters κ and η in the following correlations by McCaffrey for centerline temperature and velocity are adjusted as presented in Table 1 [62]:

$$\Delta T_0 = \left(\frac{\kappa}{0.9\sqrt{2g}}\right)^2 \left(\frac{z}{\dot{Q}^{\frac{2}{5}}}\right)^{2\eta-1} * T_\infty \quad (3\text{-}25)$$

$$u_0 = \kappa \left(\frac{z}{\dot{Q}^{\frac{2}{5}}}\right)^{\eta} \dot{Q}^{\frac{1}{5}} \quad (3\text{-}26)$$

Table 1: Constants in McCaffrey's Plume Equations [62]:

Region	$\frac{z}{\dot{Q}^{2/5}}\left[\frac{m}{kW^{2/5}}\right]$	**η**	**κ**
Continuous	< 0.08	1/2	$6.8\left[\frac{m^{1/2}}{s}\right]$
Intermittent	0.08 – 0.2	0	$1.9\left[\frac{m}{kW^{1/5}s}\right]$
Plume	> 0.2	-1/3	$1.1\left[\frac{m^{4/4}}{kW^{1/3}s}\right]$

The centerline temperature and centerline velocity for line fires after Yuan and Cox can be obtained with the respective values for η, A and B taken from Table 2 with the following Equations [63]:

$$\Delta T_0 = B\left(\frac{z}{\dot{Q}_l^{\frac{2}{3}}}\right)^{2\eta-1} \qquad (3\text{-}27)$$

$$u_0 = A\left(\frac{z}{\dot{Q}_l^{\frac{2}{3}}}\right)^{\eta} \dot{Q}_l^{\frac{1}{3}} \qquad (3\text{-}28)$$

Table 2: Constants in the Plume Correlations by Yuan & Cox [63]:

Region	$\frac{z}{L_f}$	**η**	**A**	**B**
Continuous	$< \frac{1}{2}$	1/2	6.88	898
Intermittent	$\frac{1}{2} \leq \frac{z}{L} \leq 1$	0	0.75	11.8
Plume	$1 \leq \frac{z}{L} \leq 6$	0	0.62	7.2

In Figure 19 the centerline temperatures and centerline velocities are shown as calculated from the correlations presented above in comparison to the temperatures and velocities along the centerline of the plume as they are computed in the model by FDS. The values are naturally fluctuating around a mean value. In order to get durable average results for the values for u_o

and T_0 over height, the values were recorded over 150 seconds and after a steady state seemed to be reached after 60 seconds, the recorded values were then averaged over the remaining 90 seconds (see Figure 18). Additional radial profiles of the fire plume at two different heights (10 m and 35 m) are depicted Appendix A at the end of this manuscript.

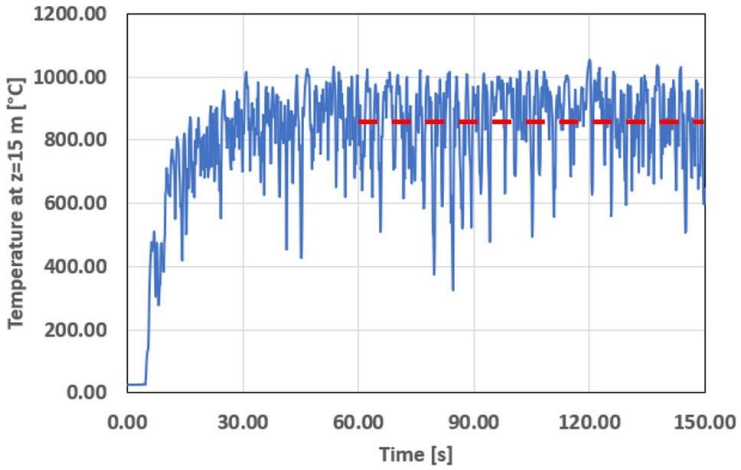

Figure 18: Temperature fluctuations over time at 15 m height in the centerline of the plume. The red line shows the time over which the value was averaged at the final mean value of ~860 °C.

The plume as it is computed by FDS shows an agreement of the centerline temperatures with those calculated from engineering correlations with deviations between 15 and 40 %, where FDS mostly overpredicts the temperatures. The general trend as well as the order of magnitude for the numbers calculated by FDS, however, seem decent. The velocities along the centerline, on the other contrary, show good compliance for FDS and the correlations by McCaffrey and Yuan and Cox within the region of the fire with deviations between 12 and 17 % and very good compliance in the region of the intermittent flame with deviations usually less than 10% and mostly between 2 and 4 %. However, in the region of the plume, the values calculated by FDS are 7-55 % higher than the values calculated via the correlations by McCaffrey and 26-90 % higher than the results obtained from the equations by Yuan and Cox. This observation is not completely unexpected as the engineering correlations that were employed here were derived from experiments with fires with much smaller heat release rates. Yuan and Cox, for example, derived their expressions from line fires with intensities up to 300 kW/m² [63]. As a result, the engineering correlations might not be suitable to estimate final gas temperatures and velocities within the plume from fires with intensities of many MW/m. The gas temperatures and hence the velocities within the region of the flame show good agreements across the different engineering correlations and the data computed by FDS. Those parameters do not fluctuate too much with the HRR of the fire, as they are rather a function of the flame temperature which depends on the heat capacity of the gases, the heat of combustion of the fuel and radiative heat losses to the surroundings [42].

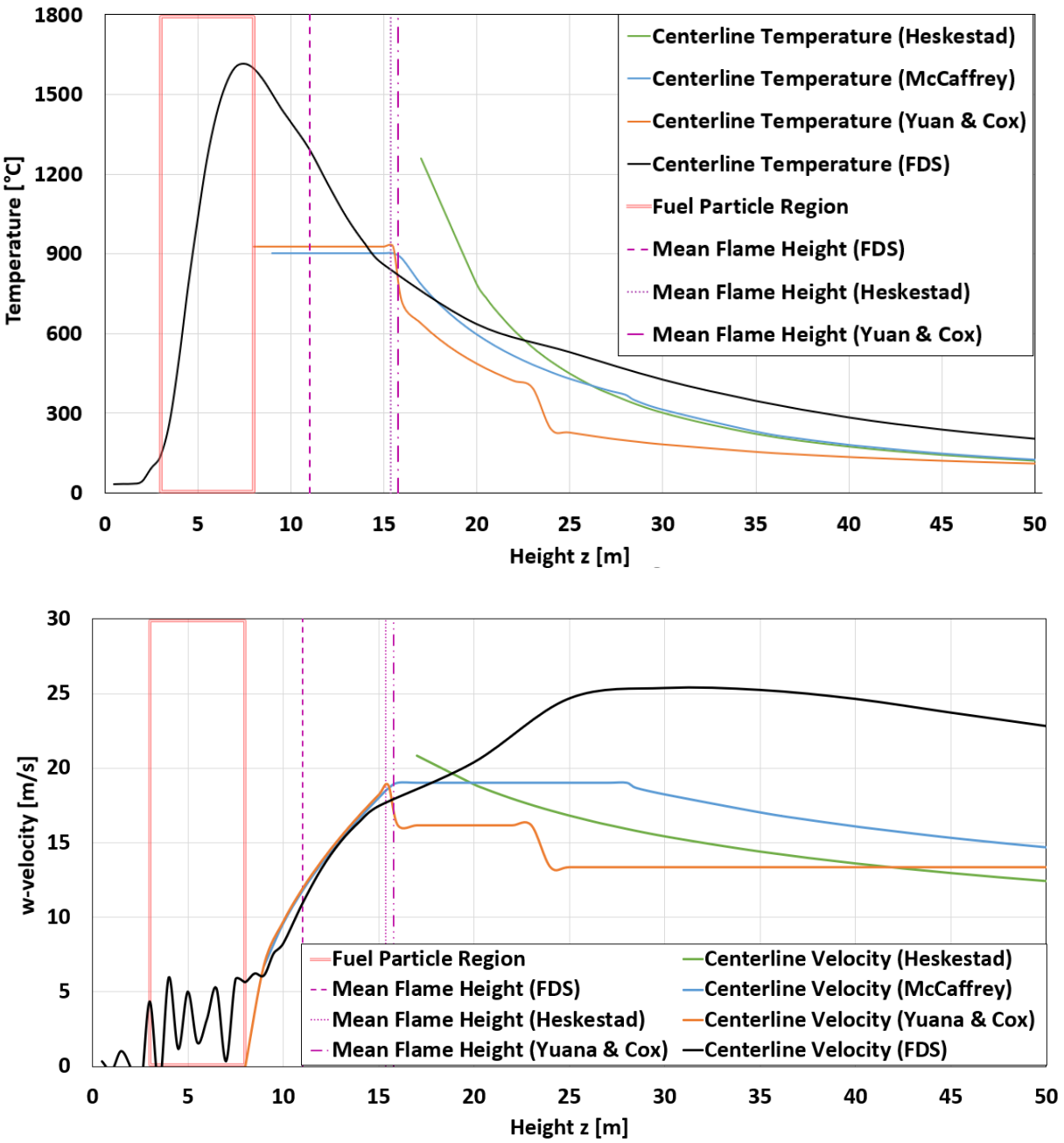

Figure 19: Comparison of centerline profiles obtained from engineering correlations and FDS.

Due to these facts, it makes sense that FDS and the hand calculations show similar values in the region below the flame height and the engineering correlations then tend to underestimate the gas velocities and temperatures along the plume centerline above the flame. Despite the difference, it is visible that the plume profile calculated by FDS shows the same trends as the values calculated via the correlations when it comes to the rates at which the velocity and temperature decrease after reaching their maximum which all are around the same height above the flame, too. Following this analysis, it needs to be added that the obtained fire plumes from the model are subjected to a level of uncertainty that already comes with the nature of the model. In the model that is used to obtain the plume depicted in Figure 19, the FDS input lines as shown in Figure 15 were employed. As a result, the 2,000 particles, representing the

total of 4,034,000 particles are each released at a random position within one of the 2,000 cells spanning the region of the fire. FDS gives an option to release those particles in the cell center instead, which results in differences in the plume characteristics (see Figure 20). For this case, the observed flame height is higher as is the centerline velocity and the centerline temperature, which might be a result of less particles being placed closer to the outer boundaries of the fire region and therefore a higher concentration of fuel gases towards the center of the fire and more heat being released towards the center of the plume.

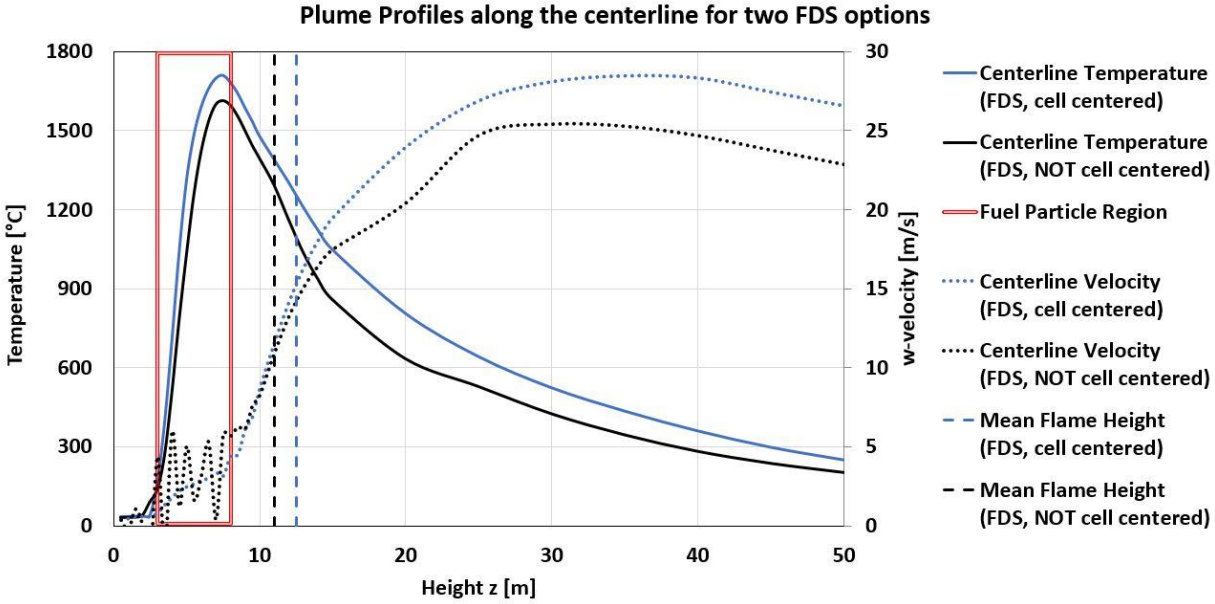

Figure 20: Comparison of the resulting fire plume for different FDS inputs.

3.3.1 Grid Independence Study

The term Grid independence study describes an analysis of the results calculated with different mesh resolutions of the computational domain for the same problem [64]. With increasing resolution, the turbulence and hence the flow is resolved better, because the turbulence is computed more accurately as described in the introduction to this chapter.

A grid independence study has the goal to evaluate whether the chosen grid resolution for a CFD simulation is sufficient to capture accurate results. Starting from poor mesh resolutions, there should be a steep difference in the obtained values between the different cases, before the obtained values from finer meshes get asymptotically closer to a final value [65]. Once the values do not change when refining the mesh, the resolution of a mesh can be deemed to deliver converged results. Figure 21 shows how the centerline profile of the fire plume changes with increased mesh resolution. The initially chosen edge size of 0.5 m was halved to 0.25 m and divided by four to 0.125 m in the considered cases. The subdivision of the domain in coarser meshes with distance to the fire is upheld as described in chapter 3.2 (see Figure 14).

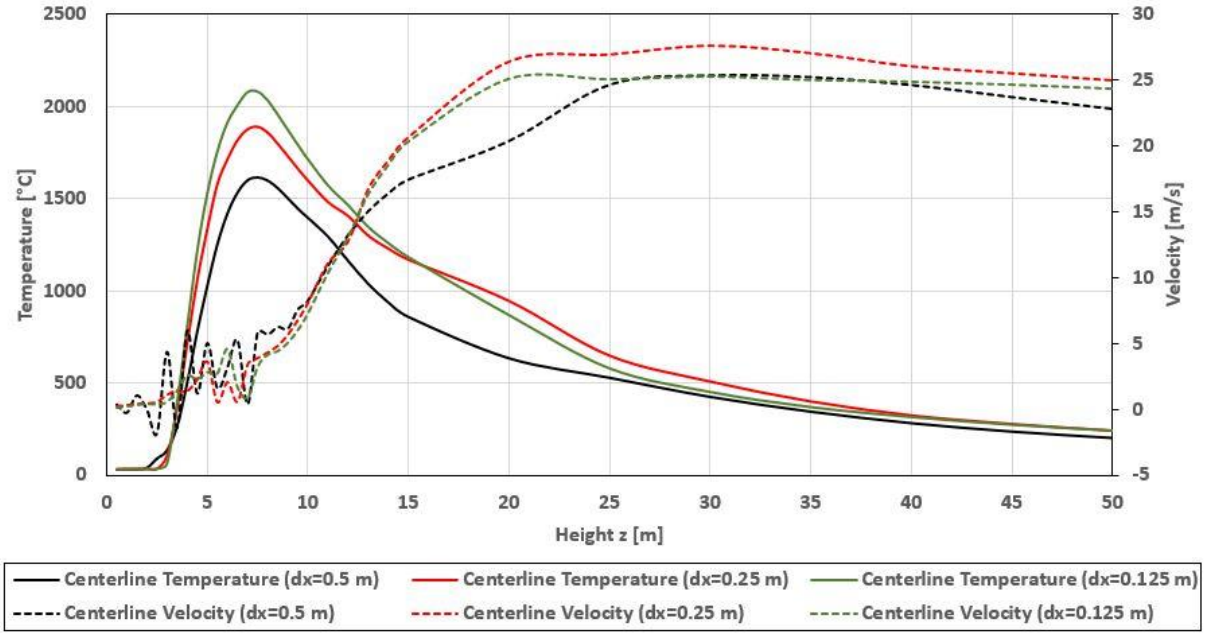

Figure 21: Recorded values for the plume centerline profile for different grid sizes in FDS.

The general trends that all meshes compute show decent agreement and also the velocities do not deviate much from each other, even though the coarse (0.5 m) resolution results in poor agreement in the region of z=13 m to z=25 m compared to the agreement that the other two cases show in that region. The peak velocities and temperatures are all obtained at the same respective heights and Table 3 shows the deviations of the values from increased mesh resolutions to the original grid size.

Table 3: Peak centerline temperatures and velocities for different mesh resolutions.

Physical property	Mesh resolution				
	0.5 m	0.25 m		0.125 m	
		absolute value	deviation	absolute value	deviation
velocity [m/s]	25.4	27.6	8.7 %	25.3	0.3 %
Temperature [°C]	1614.5	1887.4	16.9 %	2080.2	28.9 %

The general argument for not always using the finest mesh in CFD simulations or using DNS is the computational cost as simulations take more computational power to be solved with increased numbers of cells for which governing equations must be solved and the decrease in the time steps that comes with it. As a result, the mesh size is always a trade-off between accuracy and computational cost. Halving the edge size of the grid cells results in 2x2x2=8 times higher computational times for the increased number of cells and two times higher computational times, because the time stepping needs to be cut in half as well. Thus, the computational cost increases by the factor 16 when the mesh resolution is doubled.

Another factor has to be considered in this case. The deviations might not only be due to increased computational accuracy by the refinement of the mesh, but another parameter had to be adjusted together with the cell size. The previous chapter describes how the fire source

is modelled using a number of cells that release a constant amount of fuel gas into the domain. With more cells spanning the fire source, also the PARTICLE_WEIGHT_FACTOR that prescribes for how many particles a single discretized particle stands has to be changed accordingly. This might result in small changes of the HRR as it depends on the fuel mass released per particle surface area. Furthermore, this means minor changes in the arrangement of the model. Where in the initial simulation “bigger” particles are randomly distributed within each larger cell, the particles get smaller and as each cell holds one particle, the alignment of the particles will more and more look like a steady, periodic pattern. This alignment of the particles comes close to the cell centered setting of the fuel particles and has already been identified to lead to higher temperatures and velocities along the centerline, especially in the near field of the flame (see Figure 20).

From this point of view, the accuracy of the chosen 0.5 m grid resolution at the fire region can be deemed as at least satisfactory at this point as it provides reasonable calculation times on the order of hours when employing several cores in parallel mode and also a decent accuracy, especially concerning the velocities and above z=25m. As the particles will travel at a velocity that is approximately that of the gas (see chapter 2.2), they will enter the far field of the plume quickly after being released, therefore the deviations in the near field of the fire can be neglected at this point.

3.4 Model for Brand Pyrolysis and Combustion

Firebrands undergo combustion and oxidation as discussed in chapter 2.3. The process of char oxidation is relatively complicated to implement in FDS and there is no model available that can reproduce kinetics the same way as it is modelled by Sardoy et al. [39]. Due to time constraints of this project it was not possible to carry out sufficient parameter studies and employ the different approaches that are available for this problem in the framework of FDS. The decision was made to only look at the pyrolysis of firebrands and neglect char oxidation at this stage of the model. Nevertheless, the different approaches to potentially implement a char oxidation model with FDS are presented below to make them quickly available for future work in this field.

The firebrands lose mass and density by pyrolysis, volume is lost only from char oxidation. Pyrolysis of firebrands is represented by a first-order single-step reaction decomposing the virgin material into combustible fuel gas (volatiles) and char. The reaction rate is given by an equation of the form as presented in equation (2-19) for the endothermic reaction that is described by the equations (3-29) and (3-30) that resemble the pyrolysis reaction from the submodel for the fire source [39], input parameters are reported in Table 4.

$$DWF \rightarrow v_f^{char} Char_f + \left(1 - v_f^{char}\right) \times \left[\left(1 - v_f^{soot}\right) GPP_f + v_f^{soot} Soot\right] \quad (3\text{-}29)$$

Where

$$GPP_f = \alpha_f^{CO} CO + \left(1 - \alpha_f^{CO}\right) CO_2 \quad ; \quad \alpha_f^{CO} = 0.8 \quad (3\text{-}30)$$

FDS employs one-dimensional heat and mass transfer normal to the surface of a solid, in the case of particles that is along the diameter for cylindrical and spherical brands and along the thickness for plates. When char oxidation is invoked, the volume of a particle reduces in terms of the particle thickness, which is the direction of one-dimensional heat conduction and the radius for cylindrical and spherical particles and the half-thickness for cartesian elements [66].

In agreement with Sardoy et al. [39], char is considered to consist of pure carbon and the oxidation of the same considers only oxidation of all carbon into CO as described in equation (3-31). This exothermic one-step reaction is controlled by oxygen diffusion at the surface of the particle and the oxygen supply. During pyrolysis, the oxygen supply is affected by the release of combustible fuel gases and the flame around the particle that consumes oxygen in the combustion of the fuel gases. Once pyrolysis has ended, only char oxidation occurs.

$$C + \frac{1}{2} O_2 \rightarrow CO \quad (3\text{-}31)$$

The conservation equations for mass of virgin material of the firebrand and char are described by the following balance equations, input parameters for different tree species are shown in

$$\frac{\partial \rho_f^v}{\partial t} = -R_f^{pyr} \quad (3\text{-}32) \qquad \frac{\partial \rho_f^{char}}{\partial t} = v_f^{char} R_f^{pyr} \quad (3\text{-}33)$$

R_f^{pyr} is the mass loss rate per unit volume as a result from pyrolysis and can be calculated with the input parameters stated in Table 4.

$$.R_f^{pyr} = \rho_f^v \times \dot{\omega}_{pyr} = \rho_f^v \times A_f^{pyr} \times Y_f^n \times \exp\left(-\frac{E_f^{pyr}}{RT_f}\right) \quad (3\text{-}34)$$

Table 4: Firebrand properties and thermokinetic constants.

Property	Value	Units	References
v_f^{char}	0.39 (Ponderosa Pine)	-	[60]
	0.33 (other species)	-	[60]
v_f^{soot}	0.03	-	[60]
α_f^{CO}	0.8	-	[60]
A_f^{pyr}	725 (Ponderosa Pine)	s^{-1}	[60]
	3.2 (other species)	s^{-1}	[60]
E_f^{pyr}	57,361.48 (Ponderosa Pine)	$\frac{J}{mol}$	[60]
	36,600.3 (other species)	$\frac{J}{mol}$	[60]

The rate at which the particle loses volume when undergoing char oxidation is governed as follows [39]:

$$\rho_f^{char} \frac{\partial V_f}{\partial t} = -R_f^{char} s_{ox} \qquad (3\text{-}35)$$

where s_{ox} is given as $\frac{\pi D l}{2}$ for pyrolysis and $\pi D l$ for char oxidation processes, respectively. For plate or disc-like firebrands, the length l is replaced by the thickness τ [39].

The calculation of the reaction rate for heterogenous combustion (char oxidation) is the point where the approaches by Sardoy et al. [39] cannot be further implemented in the numerical model of this work due to the choice of models available in the FDS code. Sardoy et al. [39] calculate the rate of reaction for the case of no relative velocity between the wind and the particle ($\vec{V}_R = 0$) as follows:

$$R_f'^{char} = -\frac{48}{32}\left(\frac{D_{iff0}}{D}\right)\rho_0 \left(\frac{T_{film}}{273}\right)^{0.75} \times \frac{1}{\gamma}\ln\left(1 - \gamma Y_{O_2\,surf}\right) \qquad (3\text{-}36)$$

where $D_{iff0} = 18 \times 10^{-6}\ m^2 s^{-1}$ and ρ_0 are defined as the oxygen diffusion coefficient and gas density at 273 K. γ is defined as the Stefan coefficient and it is taken in the paper as -1 for a one-step char oxidation reaction. From $R_f'^{char}$ the rate of reaction is calculated for the case that $\vec{V}_R \neq 0$ as [39]:

$$R_f^{char} = R_f'^{char}\left[1 + 0.272Pr^{\frac{1}{3}}Re^{0.5}\right] \quad (3\text{-}37)$$

The Reynolds number is here calculated with the equal-volume sphere diameter as [39]:

$$Re = \frac{D_{sphere}\rho_{film}||V_R||}{\mu_{film}} \quad (3\text{-}38)$$

FDS, on the contrary, presents two different options to invoke a char oxidation model. The first one is the approach using an Arrhenius equation for the reaction rate, presented in chapter 2.3 (equation (2-19)) which takes the form of [66]:

$$\dot{\omega}_f^{char} = R_f^{char} = A_f^{char} \times Y_f^n \times e^{\frac{-E_f^{char}}{RT_f}} \times X_{ox}^{n_{ox}} \quad (3\text{-}39)$$

where the local oxygen volume fraction is calculated as a function of the depth x, the oxygen volume fraction of the adjacent gas phase within the next grid cell $X_{ox,g}$ and the gas diffusion depth L_g[66]:

$$X_{ox}(x) = X_{ox,g}e^{\frac{-x}{L_g}} \quad (3\text{-}40)$$

The second approach offered in FDS is by invoking a specific thermal degradation model for vegetation based on research papers on the subject [52,66–68]. This model consists of three reaction mechanisms is described in the equations (2-20) to (2-22). The calculation procedure for the reaction rate of pyrolysis does not change, only the parameter Y_s, is now explicitly defined as $Y_s = \frac{\rho_s}{\rho_{s,0}}$, where $\rho_{s,0}$ is the initial total density of the firebrand and ρ_s is the density of the wet, dry and charred firebrand, respectively. The reaction rate for char oxidation in this model is calculated from

$$R_f^{char} = \left(\frac{\rho_f^{char}}{\rho_{f,0}}\right)^0 A_f^{char} e^{\frac{-E_f^{char}}{RT_f}} \frac{\rho_g Y_{O_2}\sigma_f\beta_f(1 + \beta_{char}\sqrt{Re_f})}{v_{O_2,char}\rho_{f,0}} \quad (3\text{-}41)$$

Here the Reynolds number is calculated from $Re_f = \frac{\rho_g|u_p - u_\infty|D_f}{\mu}$ with the diameter being calculated from the surface-are-to-volume ratio σ_f ($D_f = \frac{4}{\sigma_f}$ for long cylinders). β_f is the packing ratio, which is for dispersed particles the sum of the volume from all particles over the overall volume that they are dispersed in. β_{char} is 0.2 by default and $v_{O_2,char}$ corresponds to the parameter s from equation (2-22) and is taken in FDS as 1.65 by default.

Another difference between all 3 models is the way that the energy release from the char oxidation reaction is treated. While Sardoy et al. [39] and the latter vegetation model in

FDS [66] add a term in the governing equation (see eq. (3-42) for the former and (3-43) for the latter formulation) for the (surface) energy of the particle that makes use of a parameter α_{char} to store a certain fraction of the released energy within the particle:

$$-k_f\left(\nabla T_f \cdot \boldsymbol{n}\right)_{surf} = h_{conv}\left(T_f^{surf} - T_{film}\right) + \varepsilon_f\left(\sigma {T_f^{surf}}^4 - \frac{G}{4}\right) + \alpha_{char} R_f^{char} \Delta H_f^{char} \qquad (3\text{-}42)$$

$$\rho_f c_{p,v} \frac{dT_f}{dt} = -\rho_{f,0}\Big(\Delta H_{vap} R_f^{H_2O} + \Delta H_{pyr} R_f^{pyr} + \alpha_{char} \Delta H_{char} R_f^{char} + \langle \nabla \cdot \dot{q}''_{c,f} \rangle V_p + \langle \nabla \cdot \dot{q}''_{r,f} \rangle V_p\Big) \qquad (3\text{-}43)$$

When using the Arrhenius formulation ((3-39),(3-40)) to model char oxidation in FDS, the only way to control the energy release from char oxidation towards the particle by distinguishing between HEAT_OF_REACTION and HEAT_OF_COMBUSTION in the inputs. The former will transfer the energy amount set for the reaction towards the particle, while the latter will release the energy towards the gas phase from combustion of the fuel gas, however some heat feed-back would be expected towards the particle from this portion as well and hence this is cum-bersome. As a result, it is hard to control the actual energy transfer from char oxidation towards the particle in this case and take user control of the energy balance.

For the cases analyzed in this work, the char oxidation process as it was discussed above has been disabled and only pyrolysis of the firebrands is considered. As a result, the firebrands will lose mass and density during the transport but will not decrease in volume and size. The for-mation of soot was modelled with the same minor simplification as explained for the fire source. Instead of making the soot generation part of the pyrolysis process, soot was taken to be gen-erated in the combustion of the fuel gases instead in the same ratio to the generation of GPP as intended in [39]. Figure 22 shows the relevant input line from the FDS code that was imple-mented in the model.

```
&PART    ID='brand_part',                &MATL ID = 'Vegetation',              &MATL ID = 'CHAR',
         SURF_ID='brand',                      DENSITY = 100.,                      DENSITY = 39.0,
         PROP_ID='particle',                   CONDUCTIVITY = 0.24,                 CONDUCTIVITY = 0.1,
         QUANTITIES='PARTICLE MASS' /          SPECIFIC_HEAT = 1.466,               EMISSIVITY=0.9,
&SURF ID='brand',                              EMISSIVITY=0.9,                      SPECIFIC_HEAT = 1.1 /
          MATL_ID='Vegetation',                N_S(1) = 1.0,
          COLOR    = 'RED',                    A(1) = 725.0,
          BACKING   = 'INSULATED' ,            E(1) = 57361.48,
          THICKNESS=0.002,                     MATL_ID(1,1) = 'CHAR',
          LENGTH=0.035449,                     NU_MATL(1,1) = 0.39,
          WIDTH=0.035449,                      SPEC_ID(1:2,1) =
          GEOMETRY='CARTESIAN' /              'CARBON MONOXIDE', 'CARBON DIOXIDE'
                                               NU_SPEC(1:2,1) = 0.488,0.122,
                                               HEAT_OF_REACTION = 418.0 /
```

Figure 22: Relevant FDS input describing firebrand pyrolysis.

3.5 Boundary Conditions

As further boundary conditions wind and temperature profiles of the atmosphere are considered. Sardoy et al. report three different wind conditions under which they gathered data: 10, 15 and 20 mph which correspond to 4.4, 6.7 and 8.9 m/s, respectively [39]. As they only report the results for a wind speed of 6.7 m/s, only this case is considered in the model of this paper as the starting point. The other wind velocities could easily be implemented in the model, but due to time constraints of the project and the simulation times for each case, that would subsequently also need to consider different subcases of varying firebrands, the decision was made to leave them out in this analysis.

Sardoy et al. [39] use the same approach to modelling wind and temperature profiles of the atmosphere with height as it is available in FDS [66]. The Monin-Obukhov theory is not to be discussed in detail here and for further reference the reader is directed to [66,69,70].

Generally, the theory describes the thermal stability and stratification of the atmosphere and the resulting influences on the turbulence of atmospheric flows (wind). Following the theory, the wind velocity and temperature of the atmosphere can be obtained as a function of the height z by [66]:

$$u(z) = \frac{u_*}{\kappa}\left[\ln\left(\frac{z}{z_0}\right) - \psi_m\left(\frac{z}{L}\right)\right] \qquad (3\text{-}44)$$

$$\theta(z) = \theta_0 + \frac{\theta_*}{\kappa}\left[\ln\left(\frac{z}{z_0}\right) - \psi_h\left(\frac{z}{L}\right)\right] \qquad (3\text{-}45)$$

$$u_* = \frac{\kappa u_{ref}}{\ln\left(\frac{z_{ref}}{z_0}\right)} \quad ; \quad \theta_* = \frac{u_*^2\theta_0}{g\kappa L} \quad ; \quad \theta = T\left(\frac{p_0}{p}\right)^{\frac{R}{W_{air}c_p}} \qquad (3\text{-}46)$$

where L is the Obukhov length that characterizes the thermal stability of the atmosphere and and should be infinitely large for cases of neutral stratification, which is the specification for the considered cases. It is recommended to use L with 1,000,000 for that purpose in FDS. θ is the potential temperature that can be obtained from equation (3-46), where p_0 is usually taken as 1000 mbar and $\frac{R}{W_{air}c_p} \approx 0.286$ [66]. κ is the Von Kármán constant that is taken as 0.4 in [39] and 0.41 in [66], u^* is the friction velocity obtained from the known wind speed at a reference height and z_0 is the aerodynamic roughness length of the ground, prescribed with 3.8×10^{-5} in [39] assuming very smooth terrain. As the atmosphere shall be neutrally stratified [39], which results in an infinite large Obukhov length, the term from the similarity functions ψ_m and ψ_h and also $\theta *$ become 0 for $L \to \infty$ and can consequently be disregarded in this work.

The reference wind speed of 6.7 m/s that was mentioned at the beginning was assigned a reference height of z=10m [39]. The resulting wind and temperature profiles as calculated by FDS and the analytically expected profiles are displayed in Figure 23.

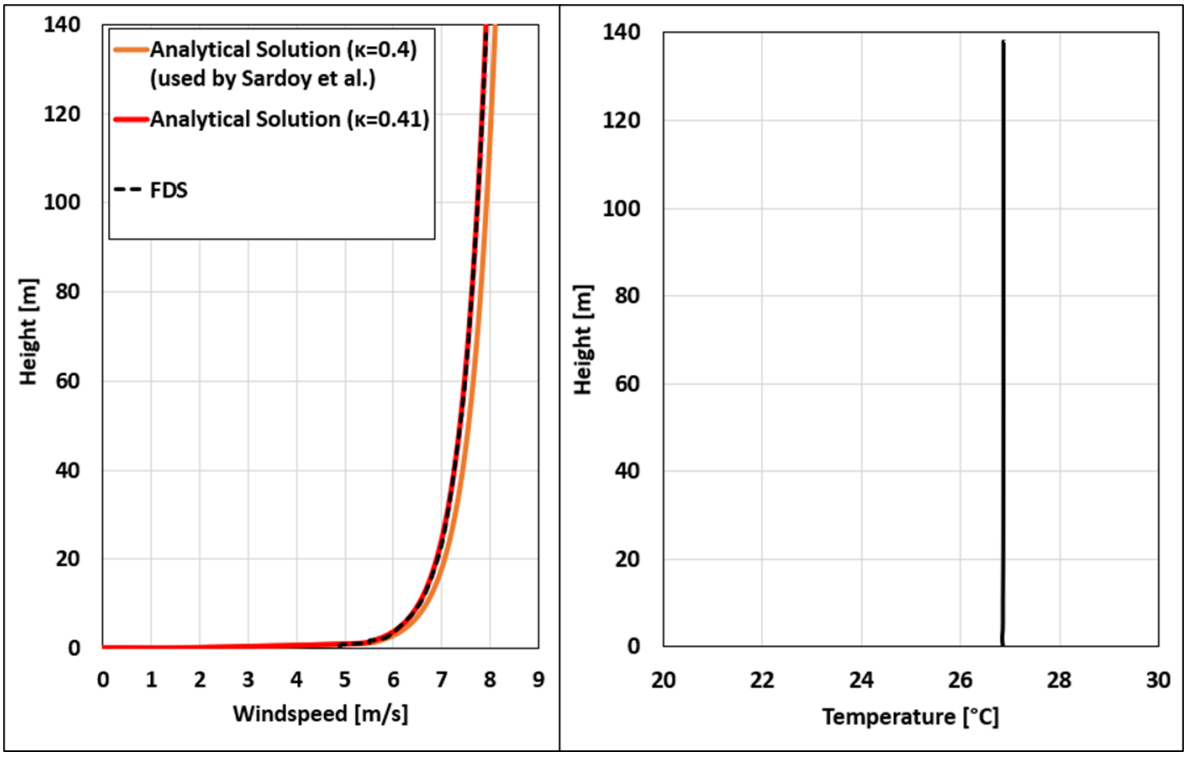

Figure 23: Atmospheric wind and temperature profiles.

4 Obtaining Relevant Data and Post Processing

Employing the FDS functions and models presented in the prior chapter, the pyrolysis and transport of disc-shaped firebrands shall be analysed with a focus on the trajectories from varied firebrand properties. FDS, however, does not have a function to properly invoke disc-like geometries for particles. Modelling the brands as short cylinders would results in the graphic appearance of discs, but the heat transfer and pyrolysis direction considered by FDS would be expected to be normal to the shell surface. Therefore, the discs are represented by plates with quadratic base areas. The width and length are chosen to be equivalent to the diameter of the disc-shaped firebrand, in terms of the resulting surface area, as schematically shown in Figure 24.

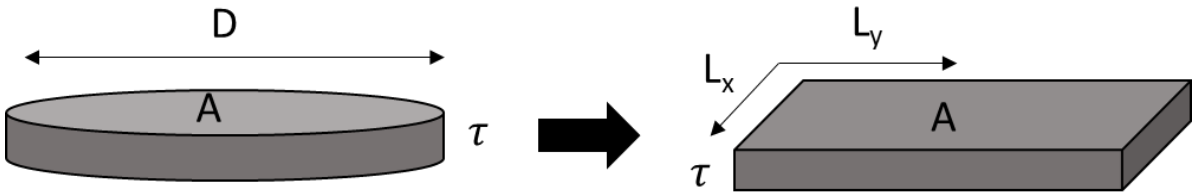

Figure 24: Plate-like representation of disc-shaped firebrands in FDS.

Table 5 gives the employed thermophysical properties of the firebrands considered in the FDS model in addition to those parameters and constants stated in Table 4.

Table 5: Thermophysical material properties for modelling firebrands.

Property	Value	Units	References
λ	0.24 (wood)	$\frac{W}{m\,K}$	[71]
	0.1 (char)	$\frac{W}{m\,K}$	[71]
C_p	1466 (wood)	$\frac{J}{kg\,K}$	[71]
	1100 (char)	$\frac{J}{kg\,K}$	[71]
ε_f	0.9	-	[72]
$\Delta H_{r,f}^{pyr}$	418	$\frac{kJ}{kg}$	[60]
ΔH_c^{CO}	10,100	$\frac{kJ}{kg}$	[61]

The particles considered in the model are assigned varied thicknesses between 0.2 cm and 10 cm. The density of the virgin material of firebrands is varied between 50 and 200 kg/m³, where the analysis is emphasized especially on those brands with densities between 50 and 150 kg/m³ to compare the observations to results from Sardoy et al. [39].

The point of release for the particles in the domain is chosen after [39], i.e. the ridge between the top and the downstream side of the fire source at a vertical plane that is 2.5 m offset from the symmetry plane of the domain ($x_0 = 35\,m; y_0 = 2.5\,m; z_0 = 8\,m$). The firebrands are released at an initial temperature that is equal to the time averaged local gas temperature of this spot. This temperature of 1044°C is acquired through the same methodology as described for the time average of the fire plume profiles.

The first set of simulations includes firebrands with the same properties for which Sardoy et al. [39] have reported the trajectories. Those firebrands have been assigned an initial velocity equal to the local gas velocity as this has been done in [39]. The local gas velocity at the point of release was found from time averaged measurements with 0.697, -0.666 and 0.174 m/s for the u-,v-, and w-components of the velocity, respectively.

The study is widened after running cases for comparison, and particles of varying thickness and density are analyzed. In this second set of simulations, the firebrands were released with zero initial velocity. This decision is based on the belief of the author that this represents the more realistic case, because firebrands will have zero velocity when they form by breaking off from larger units of material. The first particle is released after 60 seconds, which was the time to reach steady state in the closer regions to the plume. The rest of the particles are released with a delay of 1 second between the particles to ensure that their flight paths can be assumed not to be influenced by each other.

Appendix B contains the relevant lines of an FDS input file as it was used to model firebrands equivalent to 10 cm in diameter with a density of 100 kg/m³ and thicknesses between 0.2 and 10 cm. This file is meant to show an example of how the final simulations are set-up and how the previously discussed sub-models of the simulations are combined.

From the lines, it becomes apparent, that every particle is injected separately into the computational domain. This is done to simplify the post-processing of the output data and enable a system that makes the data for each particle much easier to extract. FDS tracks the X-, Y-, and Z-coordinates of a particle over time. Additionally, some key properties can be assigned to be tracked as well. The mass and temperature of particles is tracked along with the position over time in this case. FDS stores this information in a binary file that is written as an output file from the calculations. Using a Matlab script the information it contains can be read. However, FDS will arrange the information in a way that makes it very hard to keep track of which

values actually correspond to which particle as the information is arranged in a matrix of multiple columns. The values for each particle can be distributed over different columns which makes it hard to follow and get information on the properties of a single particle. A solution to this is that each particle is assigned a separate particle group, which then results in a separate matrix for that group only showing one column with the values that belong to that specific particle. Following this approach, the extraction of data on each particle is easier because it is clear which particle owns which properties in the matrices.

The drawbacks of this approach are the number of lines in the FDS code that are required to come up with this scheme, since each particle requires a unique line to be defined, and another unique line to assign release parameters. Additionally, a third line that defines the time of release via control logic, which is a simple timer in this case. The increased number of particle groups also requires more virtual memory by FDS and slightly increases the computational costs. However, the impact on actual calculation times is not expected to be significant as usually it is not the memory of a computer that is the limiting factor in computational speed when solving CFD models, but it is rather the processor speed that plays the more important role for those considerations. The Matlab function as it is offered by the FDS developers on “Github” is provided in Appendix C [73].

Once the data is extracted and can be read, the particles are analyzed regarding their trajectories, and flying and landing behaviour in relation of their initial properties.

5 Results

The following sections contain results that were obtained at different parts of the modelling process and were involved in the decision making towards analysed configurations of the final transportation modelling and data collection. The presented results contain brief descriptions of the respective case. Results that only address submodels and sub-aspects of the original problem are briefly discussed towards the conclusions where it is considered that they are important for the configuration of the overall simulation of the transportation problem.

5.1 Testing the Pyrolysis Model

To establish the proper functioning of the model, small-scale simulations were carried out to test the reaction of firebrands with the specified properties and pyrolysis kinetics. Two different setups are considered in this process and will be discussed in the following section. The relevant FDS input for both cases is reported in Appendix D.

The first case mimics a TGA experiment where a very thin firebrand is considered and assigned an arbitrary high heat transfer coefficient. Hence, the firebrand can be regarded to be thermally thin. Starting from an ambient temperature of 20°C the ambient gas temperature is increased at a rate ok 5K/min until reaching 820°C which ensures that the particle can be assumed to be at the same temperature as the surrounding gas. Only the reaction of the solid phase is considered, and no combustion of the fuel gases is simulated. The results from this configuration for relevant variables that were recorded throughout this simulation are shown in Figure 25.

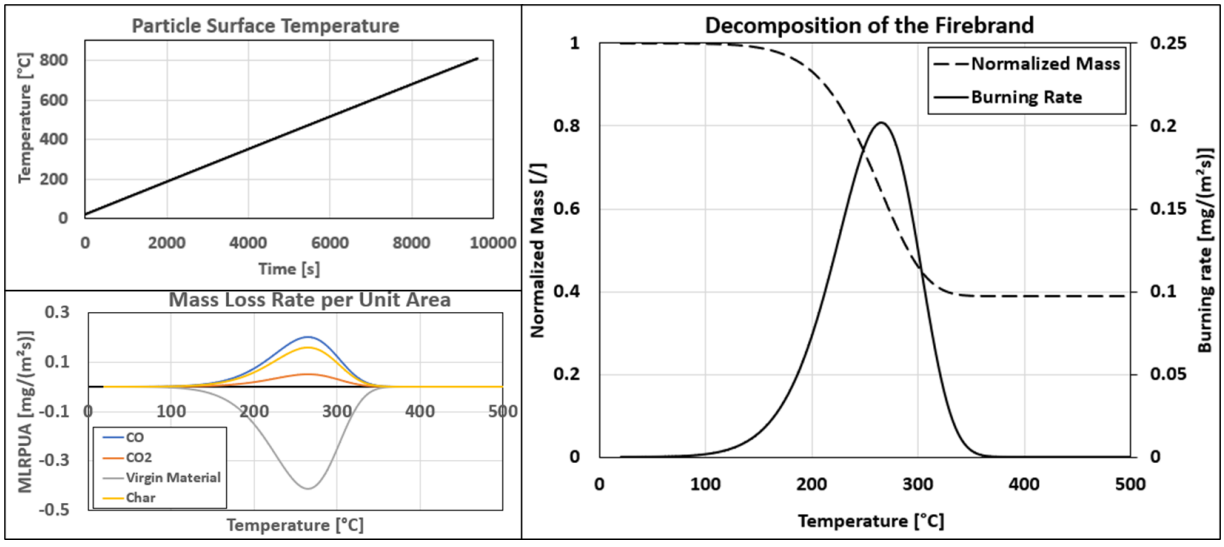

Figure 25: Results from a simulated TGA experiment. The burning rate refers to the MLRPUA of fuel gas (CO).

The MLRPUA for all species and hence the pyrolysis reaction rate peak at 265°C, which is close to the range of values reported in Babrauskas [41] from a study by Bixel and Moore [74] on autoignition temperatures (AIT) of various wood and cellulosic materials in a similar test configuration, where each specimen was also heated over hours. AITs between 203 and 257°C are reported for different wood types [41]. For shorter times to ignition by pilot ignition, higher heat fluxes and corresponding ignition temperatures are reported for wood, e.g. 350-500°C for times to ignition between 23 and 1094 seconds for wood samples with densities between 280-540 kg/m³ [75]. In conclusion, the pyrolysis behaviour seems to be in good agreement with experimental values from the literature. The far smaller density of the sample from this work needs to be considered as well, which indicates relatively low thermal inertia (see chapter 2.3) for the firebrands here compared to the material used in other studies. Therefore, shorter times to reach pyrolysis and or ignition can be expected for realistic cases as the material will be relatively well responsive to incident heat from the ambient.

For further references and summaries of the results from similar studies the reader is referred to Babrauskas [41].

The second experiment considers a firebrand with the geometry and the thermophysical properties as are later used in the full-scale model simulations. In this setup, the firebrand is released into the domain where the ambient gases are at 20°C and the firebrand bears an initial temperature of 900°C, the heat transfer towards the firebrand is not arbitrarily controlled but calculated through FDS. Pyrolysis and combustion of the generated fuel gases is considered and monitored. This configuration should come somewhat close to what the firebrands are later subjected to from the fire plume. The results from monitoring these processes are presented in Figure 26.

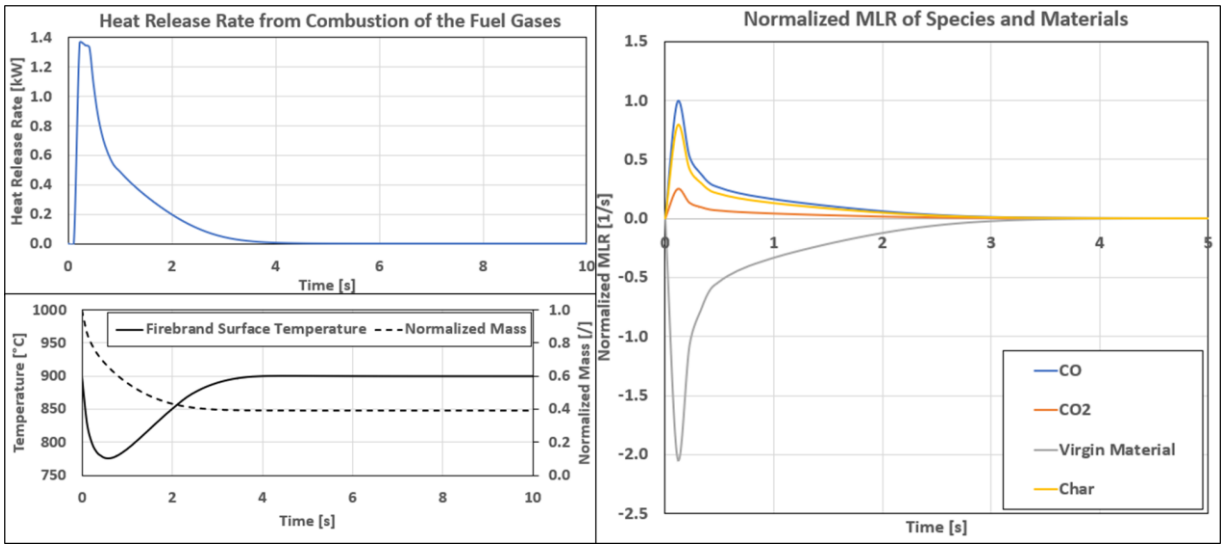

Figure 26: Results from test running the simulation of pyrolysis of a firebrand under more realistic conditions.

Naturally, the temperatures will not be constantly as high as 900°C but decrease with distance from the fire source. However, for the purposes of the simulation, the particle is static and not moving while also not being influenced by any wind. Yet, the general behaviour becomes clear from this setup. The total amount of energy released during the combustion, which is the time integral over the HRR curve, is 1. 2447 kJ. That is in very good agreement with the energy release that is expected from a single brand from theoretical calculations:

$$Q = m\Delta H_c = 0.488 \cdot 0.035449^2[m^2] \cdot 0.002[m] \cdot 100\left[\frac{kg}{m^3}\right] \cdot 10100\left[\frac{kJ}{kg}\right] = 1.2387\ kJ \qquad (5\text{-}1)$$

The first four terms in the explicit form are the mass fraction of carbon monoxide that emerges from virgin material via pyrolysis, the edge size and thickness of the square-shaped firebrand and its density, respectively. FDS seems to slightly overpredict the heat release from the particle here, but the error is very small with less than 0.5%. The general trends of the shown curves look as expected and the mass loss that is evident from the normalized mass correlates well with the normalized MLR of the different pyrolysis products and the HRR. The curves for HRR show the onset of Pyrolysis until reaching a peak in the transformation of the virgin material and also the decrease of the pyrolysis rate with less virgin material being available.

5.2 Analysis of the Pyrolysis Model

Following the validation simulations for pyrolysis behaviour of firebrands, the pyrolysis process as it is modelled by the presented model is further investigated in detail to identify dominant parameters that influence the thermal degradation of the particles. The configuration of this analysis follows the second case that is considered in the tests of section 5.1 and is chosen with a single firebrand that is initially at a high temperature and subjected to an ambient gas temperature of 20°C. This shall mimic a firebrand that is released from the fire and cools down. During the cooling process, the surface temperature, the HRR from the generated fuel gases and mass loss rate of fuel gas leaving the particle, and the particle mass are recorded over time to keep track of the process of pyrolysis. Heat transfer is calculated through FDS. The input files resemble the approach depicted in Figure 50 in Appendix D.

Three parameters are investigated that might influence the pyrolysis characteristics of a firebrand. The density of the material, the temperature that the firebrand is exposed to, here also referred to as the initial temperature, and the thickness of the firebrand. The thickness, however, could also be expressed in terms of the aspect ratio in an understandable manner, because all following results were obtained from tests with 10 cm diameter-equivalent, except where stated differently. The aspect ratio for the considered thicknesses between 0.2 cm and 10 cm varies, following equation (2-1) for discs, with 0.02 to 1. The largest firebrands might

actually have an aspect ratio >1, as the diameter equivalent to 10 cm results in edge sizes of 8.87 cm. With a thickness of 10 cm, the comparison to disc-like firebrands might become a long stretch and the aspect ratio for those brands when employing the ratio for rod-like geometries becomes 1.13. The thicknesses of firebrands in the simulation is changed for results of later chapters to not exceed the edge size of the disc-like particles. For the remainder of this chapter, the firebrands are characterized in terms of thickness rather than the aspect ratio, because it provides a better understanding of the detailed geometry for the reader right away. The initial temperature of the firebrands is varied between 900°C, which is an estimate of typical high temperatures in fires, and 500°C. Moreover, three different densities are considered throughout these tests that were employed by Sardoy et al. [39] in their original work: 50 kg/m³, 100 kg/m³ and 150 kg/m³.

Figure 27 shows how the surface temperatures of firebrands, between 0.5 cm and 6 cm thickness, show different behaviour depending also on the initial temperature. The density is 150 kg/m³ for all samples. First, it becomes evident that thicker firebrands tend to cool down slower which is a result of the thermal inertia of the material. Even though this property does not change for the different particles as it is a material property, it describes how much energy is necessary to heat up certain amounts of that material and how well this heat is then transferred through the body. By reviewing this case backwards and considering the heating of the particles makes the process more approachable: With less material that needs to be heated for thinner brands, but the same amount of heat exchange with the ambient as the particles are subjected to the same conditions, the thinner brands do heat quicker because of that lack of material that can absorb and distribute the heat, the particle becomes more sensitive and quickly responsive to changes of temperature in the ambient. More results on how the thickness influences the observed trends for firebrands in this model are shown in Figure 51 in Appendix E. From those results, it becomes visible that firebrands with a density of 150 kg/m³ cool down quickly when they are thinner than 2 cm. In contrast, firebrands with a thickness greater than 2 cm do not show significant differences in their surface temperature over the first 60 seconds of burning compared to each other. Firebrands between 4 and 10 cm thickness all show almost the same surface temperature within the first 90 seconds of burning.

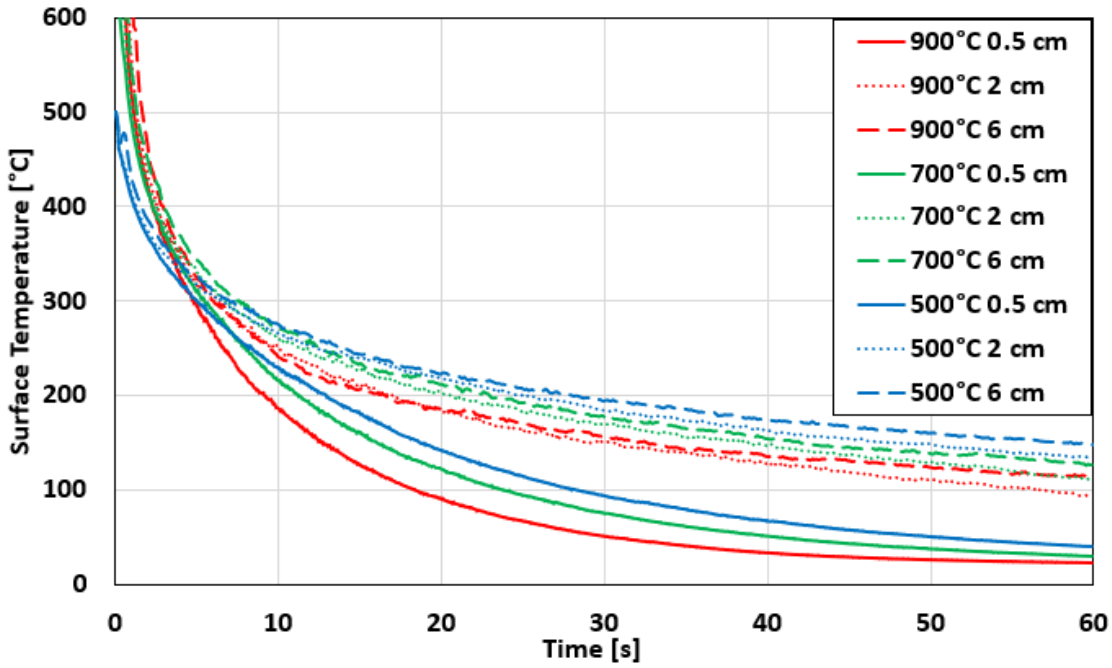

Figure 27: Surface temperature of firebrands over time for different initial temperatures and thicknesses

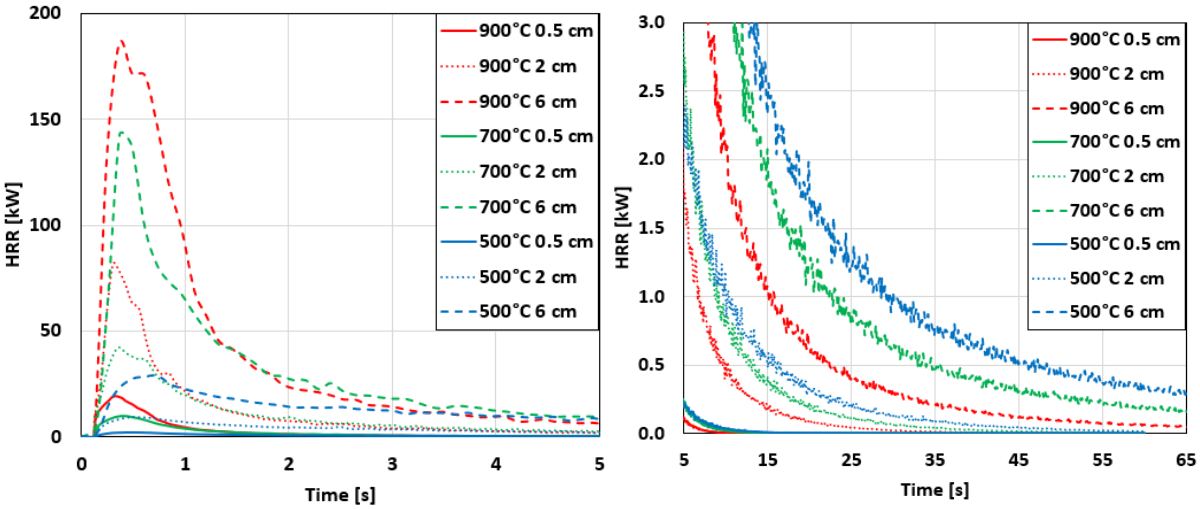

Figure 28: HRR from firebrands at different initial temperatures and with different thicknesses.

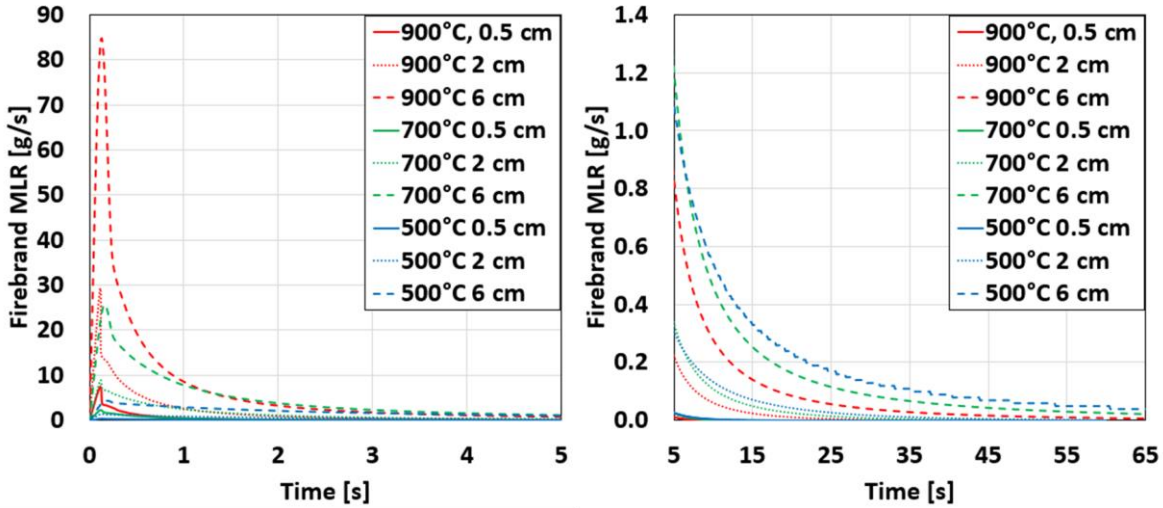

Figure 29: MLR of fuel gas from firebrands at different initial temperatures and with different thicknesses.

Figure 27 shows furthermore how the initial temperature influences the cooling of the firebrands and the trend that becomes apparent is unintuitive. Firebrands that are released at higher temperatures show steep cooling curves and show surface temperatures that are smaller than those of firebrands that are released at lower temperatures already after approximately 5 seconds. Taking the Mass loss rate of HRR from each firebrand into account that is shown in Figure 28, it becomes clear that the higher the initial temperature is, the higher the peak of the HRR is also. The firebrands released at 900°C, for example show peaks in their HRR that are about 35, 46 and 148 times higher than the values for the heat that they still release after 5 seconds for 6 cm, 2 cm and 0.5 cm thickness, respectively. The same firebrands released at 500°C, on the contrary, show peaks that are only 3.5, 4.3 and 11.8 times higher than the HRR value after 5 seconds. Figure 29 shows the MLR of the same firebrands and similar trends become visible.

This observation gives insights on two mechanisms. First, the HRR and the MLR can be taken as a direct measurement of the reaction rate of pyrolysis as the amount of fuel gases that the HRR depends on directly depends itself on this very rate. However, the HRR also depends on the combustion process and might be limited in conclusions that can be made for the pyrolysis rate from it without further consideration of the combustion details. Hence, the MLR of the solid should rather be taken in consideration to show the course of the pyrolysis rate and from that one can see a peak in the pyrolysis reaction rate for initially hot firebrands and as pyrolysis is an endothermic process, the particle loses energy in the form of heat to vaporization of the solid and generation of volatiles. Additionally, the high pyrolysis rate consumes most of the material that can be converted into fuel gas almost instantaneously, whereas lower initial temperatures lead to a steadier release of fuel gas from the brand. This ensures that even after the first few seconds, significant amounts of fuel gas are being released from the particle and issue a heat feedback towards the firebrand from combustion of said gases and reducing the rate at which the particle cools down. This is evident from the MLR from firebrands that are injected at lower initial temperatures which are higher than those for particles released at high temperatures after the first burning phase of 2-3 seconds as well as when the normalized mass of the firebrands is plotted over time as it is done different initial temperatures and thicknesses of the otherwise similar particle ($\rho = 150 \frac{kg}{m^3}; D = 10\ cm$) in Figure 30. With v_f^{char} taken as 0.39, a normalized mass of 0.39 corresponds to a fully charred firebrand.

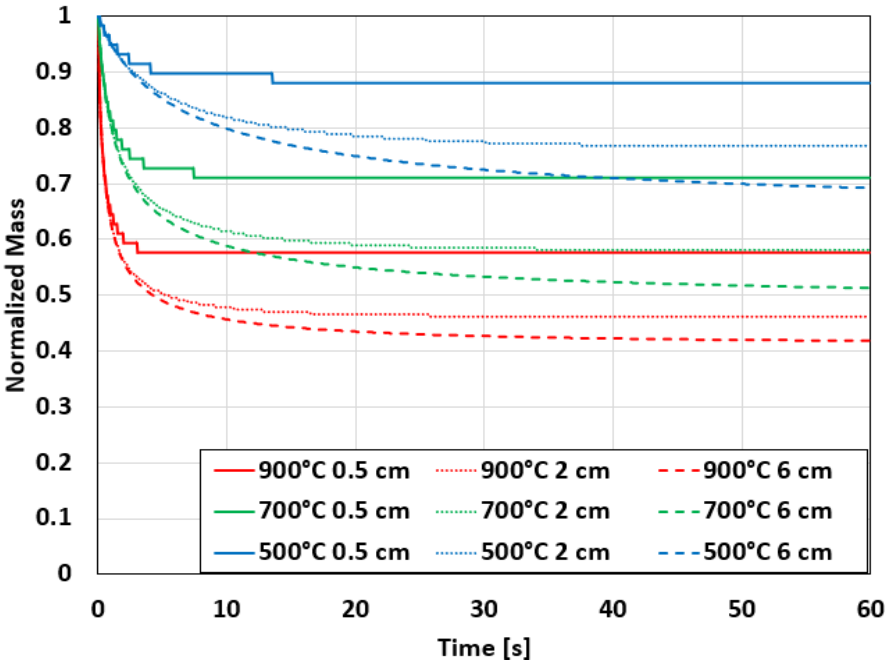

Figure 30: Normalized mass over time for firebrands at different initial temperatures.

Figure 30 furthermore shows, that for brands of smaller thickness, the conversion of virgin material becomes less and less complete and the effect stacks with lowering the initial temperatures even further. This results in less heat being released from the particle pyrolysis, and subsequent combustion, of the fuel gases once the firebrand left the initial state of pyrolysis due to its initial high temperature. We see that the curves for the same initial temperature in Figure 30 are identical for the first 1 to 2 seconds approximately. Here the particles still pyrolyze at the same rate due to their initial temperature and self-sustained pyrolysis is not yet an issue. The thinner particles show less capability for self-sustained pyrolysis over longer time, reducing their mass loss rate very rapidly to small values. This is also indicated looking at the HRR (Figure 28) and MLRPUA (Figure 31) of fuel gas released by the particles. The HRR depends on the MLR of fuel gas and is relatively small for thin particles in general. For particles of the same thickness, the MLRPUA is smaller at the beginning for lower initial temperatures. However, just simultaneously to the HRR, the values for the MLRPUA of fuel gases are more constant and reduce at a lower rate than for initially very hot particles. Additionally, to the above discussed mechanisms of the generation of volatiles and more virgin material being available influencing the pyrolysis , the large amounts of char that are produced right at the beginning for particles initially at high temperatures need to be mentioned. They have an insulating effect, and pyrolysis becomes less effective because the virgin material must be heated in depth of the body and not just in the outer regions of the particle.

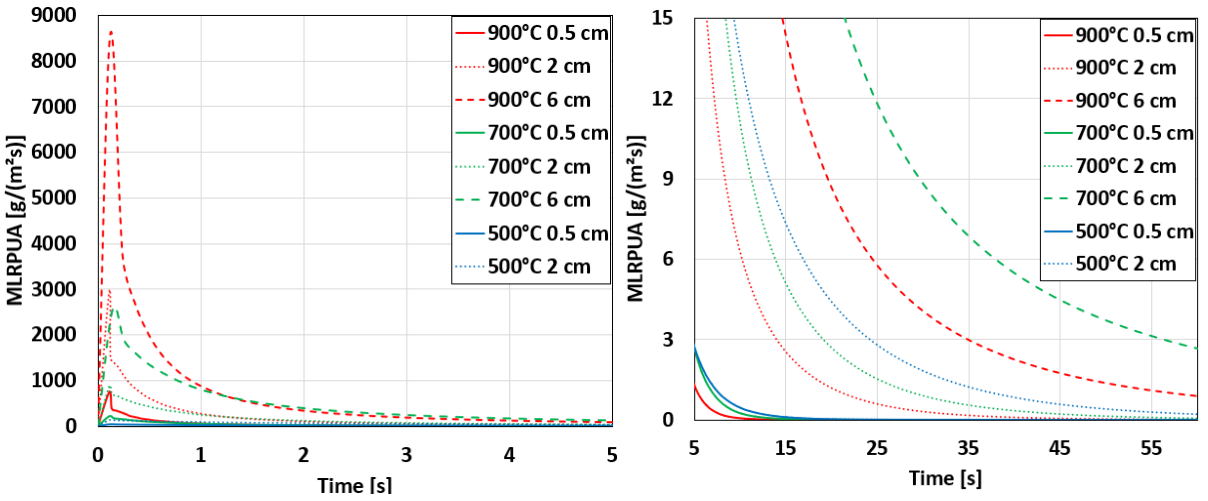

Figure 31: Mass loss rate of fuel gas from the firebrand per unit area of the surface from firebrands of different thickness and initial temperature.

In support of the statements about the heat of reaction (HOR) for the endothermic pyrolysis influencing this process significantly, Figure 32 shows the reaction of a firebrand ($\tau = 6\ cm; \rho = 150 \frac{kg}{m^3}; D = 10\ cm$) at different initial temperatures when the HOR is set to 0. In comparison to Figure 27 and Figure 28, the firebrands do not deviate that much from each other in their properties over time anymore, but the effect of the sudden vaporization of fuel gas for high temperature firebrands and more sustained heat feedback from combustion over a longer period towards particles released at lower temperatures is still visible. Both mechanisms are therefore equally important to explain the influence of the initial temperature of the firebrand.

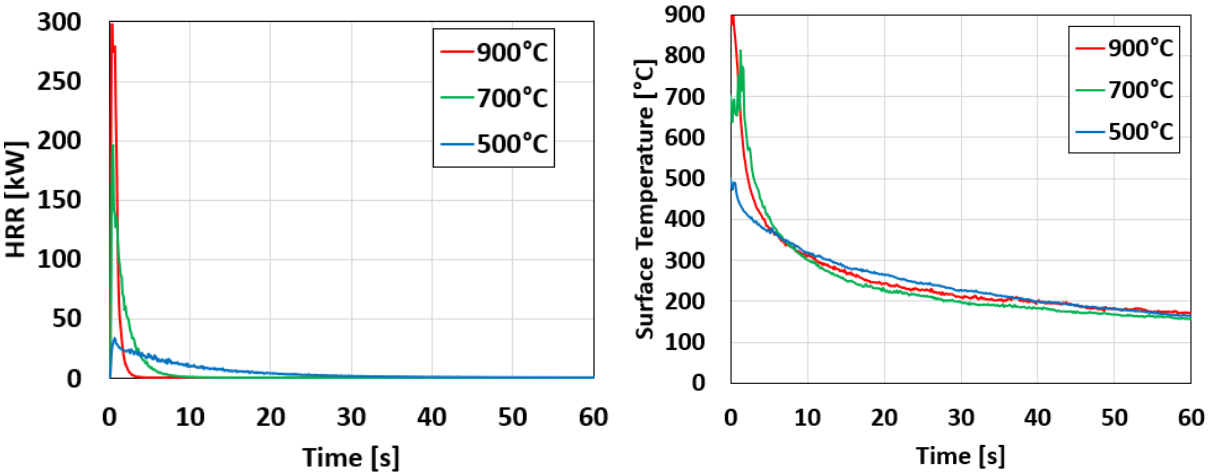

Figure 32: HRR and surface temperatures for firebrands released at different temperatures with HOR=0 kJ/kg.

The influence of the density of firebrands is investigated for brands of the same size and the same initial temperature ($D = 10\ cm, T_0 = 900°C$). Figure 33 shows how firebrands of different density and thickness vary in their behaviour of cooling down showing the surface temperature over time. Figure 34 shows how the HRR varies for the same particles. The ability to maintain at higher temperatures for longer for particles with higher densities is a consequence of the

increased thermal inertia. The concept of this bulk property of the product of thermal conductivity, density and thermal capacity was introduced in chapter 2.3 and with increasing thermal inertia, a body takes longer to react to changes of temperature in the ambient. On top of this, higher density vegetative material bears the potential to release more mass of fuel gas, which is the reason for those particles showing higher heat release rates than their counterparts. The increased heat will also cause slightly higher heat feedbacks towards the particle which supports maintaining the higher surface temperatures.

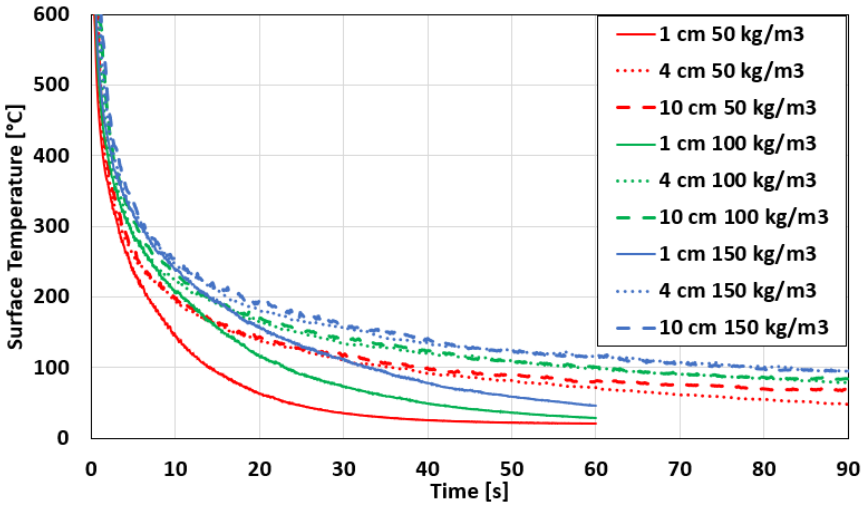

Figure 33: Cooling of firebrands of different density and thickness.

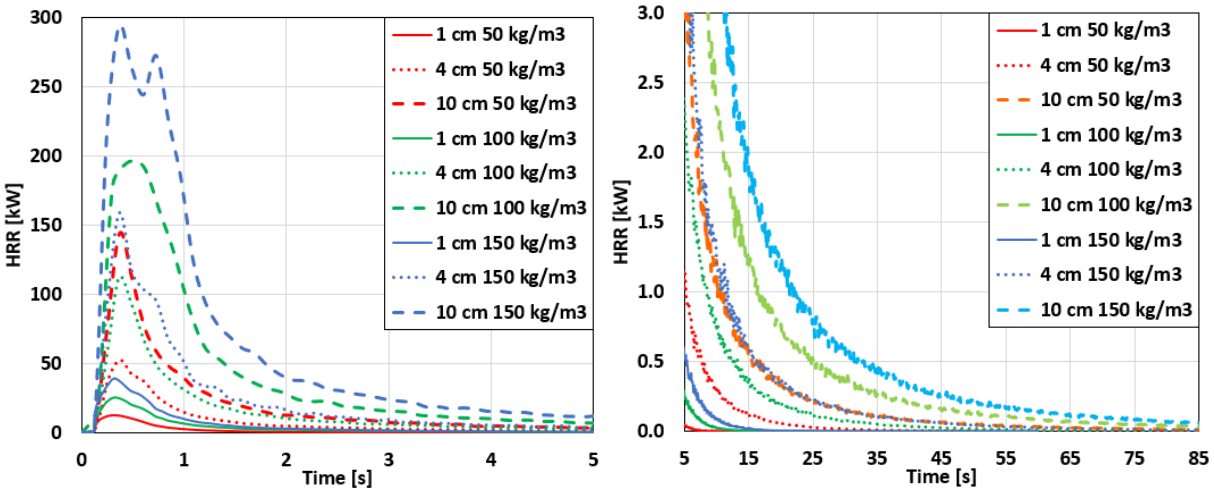

Figure 34: HRR from firebrands of different density and thickness.

From the previous results on how the different firebrands undergo pyrolysis, two mechanisms that end pyrolysis can be identified that become most visible in Figure 30, where the normalized mass over time for particles at different initial temperatures is shown. Either the firebrand is fully charred, and no vegetative material is left to pyrolyze, or the firebrand cools down to a temperature that does not allow further pyrolysis. Since char oxidation is not considered in this model, the firebrand will cool down after being fully pyrolyzed. The conclusion from these statements is that the temperature of a firebrand can be considered as a criterion to identify whether a particle is still pyrolyzing or not in this model.

For this purpose, the surface temperature of the particles from the cases described above is plotted against the HRR from the same. The HRR is taken as a measure for the pyrolysis reaction rate and quantifies the heat output from a certain particle. Figure 35 and Figure 36 show the mentioned plots for different particle densities, thicknesses and initial temperatures. Additional plots showing similar curves for a larger variety of particle thicknesses are provided in Figure 53 in Appendix E. The plots show some irregular shapes for the region of higher temperatures. This is the result from only a very few data points available in that region because the particles release most of the heat in the first 1-2 seconds after their release and therefore not many data points are collected during that time. The fluctuations of the data then lead to this unfamiliar shapes when curves are plotted. This issue does not need to be further addressed as it will become clear in the following text that the low temperature region is the part that needs to be addressed here more closely.

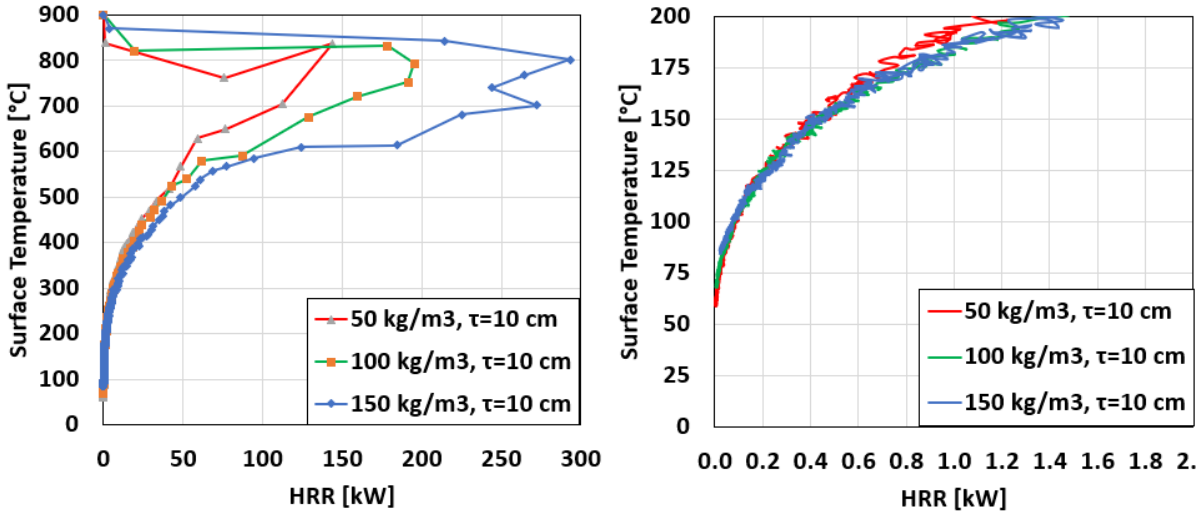

Figure 35: Surface temperature vs. heat release rate for particles of different densities.

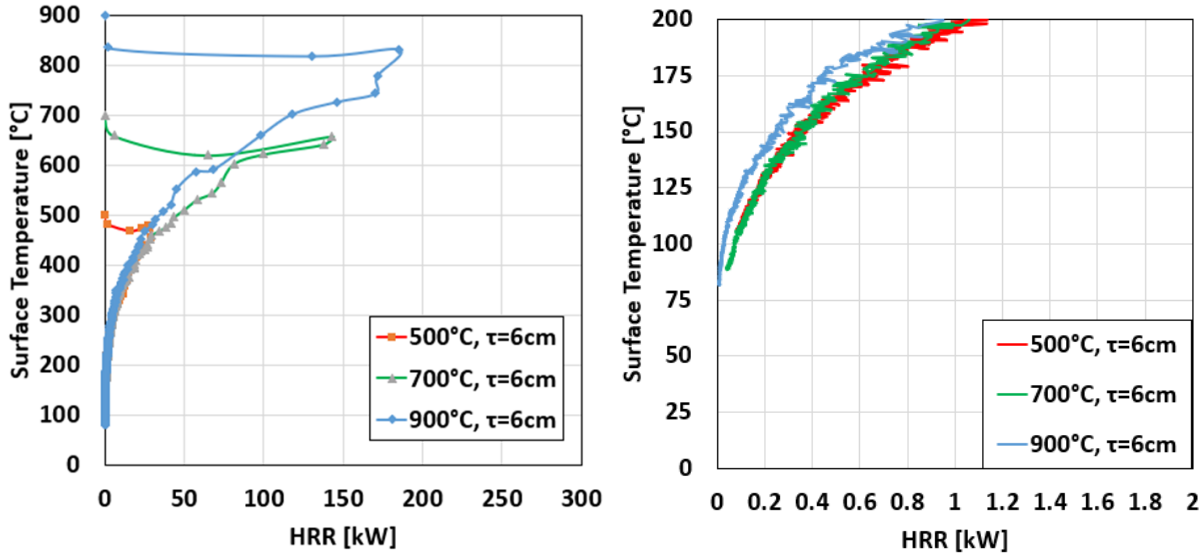

Figure 36: Surface temperature vs. heat release rate for particles of different initial temperature.

From these graphs a trend becomes apparent. The rate of heat release from all particles, independent of the thickness, initial density or initial temperature of the firebrand, falls below approximately 0.1 kW when getting to a surface temperature of 100°C. Moreover, the potential peak HRR decreases with density and particle thickness and the actual peak in heat release depends on the intial temperature the firebrand is subjected to. Merging these statements with the results presented in this chapter, two cases emerge for the moment that a particle cools down to 100°C: In the first case the particle is rather thin and/or has a low density, then the peak HRR will be relatively low from that particle regardless of the temperature it is exposed to and 0.1 kW might not yet appear as a small proportion of that peak value. However, in this case the particle can be regarded as being at least close to being thermally thin, this has been already discussed above for particles of lower density and thickness. Hence, the combustible material of it can be assumed to be consumed almost instantaneously and we are looking at a particle that can be assumed to be effectively burnt out. In the second case, thicker particles and those of higher density are considered, which show high potential for their peak HRR. In these cases 0.1 kW refers to a value that is about 0.03% to 0.1 % of the observed peak values from these particles and is deemed small enough to assume that the HRR has reduced sufficiently to define this value as where pyrolysis stops. Furthermore, the temperature of 100°C, that was found to correspond to this 0.1 kW threshold value, is the temperature at which the onset of pyrolysis becomes visible during the TGA tests when a single thin sample is heated slowly over longer times (see Figure 25).

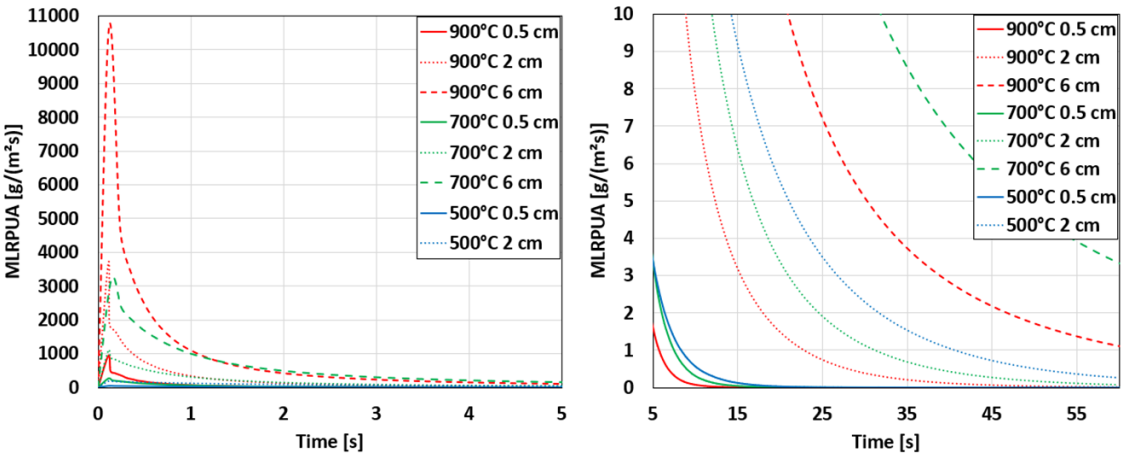

Figure 37: Total mass loss rate per unit area for different firebrand configurations.

In addition to this criterion that is worked out to determine in a simple way if a particle can still be considered pyrolyzing, another way to determine this state is the mass loss rate of the solid. This criterion was already mentioned previously, where the MLR of the fuel gas shows the same trends as the HRR. In different studies, the mass loss rate of solid wood for flaming pyrolysis has been shown to have a minimum between 1.5 and 5.1 g/(m² s) [41,76–80]. Looking at this value for firebrands with different initial conditions and properties (Figure 37) and comparing the time scales that are obtained to get to an end of pyrolysis, the temperature

seems an overly conservative criterion as it predicts, for example, for the thinner brands initially at 900°C times until the end of pyrolysis between approximately 19 and 29 seconds (compare Figure 27). The MLRPUA criterion, depending on the value that is chosen to correspond to the end of pyrolysis, gives time scales between less than 5 seconds and close to 10 seconds for the same firebrands. A difference could lay in the distinction between pyrolysis and flaming pyrolysis. While the minimum values for the MLRPUA of wood are corresponding to observed flaming ignition of the material, the temperature criterion corresponds to the gasification of solid material. Even though the material might be generating volatiles, if there is material left to pryolyze, until it cools down to 100°C flaming, the amount of evaporated fuel gas could be too low to form ignitable mixtures with the ambient air and hence even though the particle might show pyrolysis on that level it is irrelevant for pratical considerations. Hence, the MLR criterion might be more suitable to define the boundary in the distinction between pyrolysing and non-pyrolysing brands.

5.3 Firebrands in Large Outdoor Fires

Following the single item tests, the configuration, as explained in chapter 3 and 4, is considered for the simulation of firebrands in large outdoor fires. Figure 38 shows as an example of the simulation in Smokeview, a program that is developed by NIST alongside FDS, visualizing the results. In several simulations, particles of the size equivalent to 4 and 10 cm diameters were released with initial densities between 50 and 200 kg/m³ and thicknesses between 0.2 and 8.87 cm.

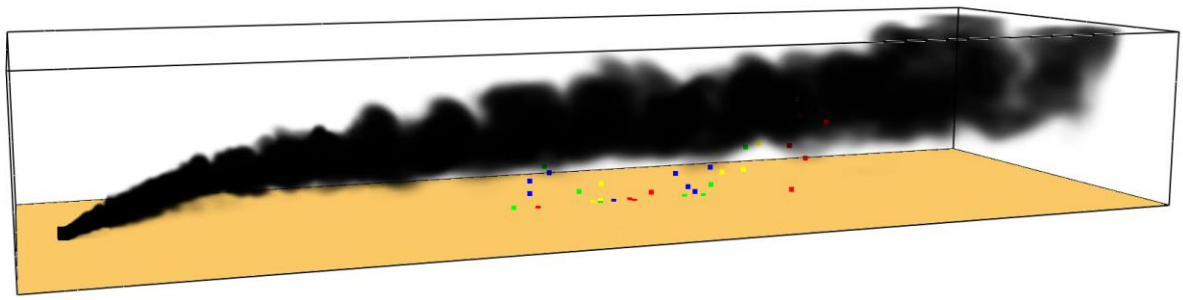

Figure 38: Momentary visualization of the transport of firebrands in the FDS simulations (not to scale.)

In the following sections the results from the firebrands travelling in the fire plume are presented. First, trajectories are shown for cases that were chosen with similar configurations to [39]. Here the results shall be presented in similar manner and deviations (if any) are discussed in regard of their source. Second, more firebrand configurations are considered, and the transport of the firebrands is analyzed with regard of the state that they are in upon landing and the initial properties of the firebrands.

The trajectories of firebrands in the vertical plane reported by Sardoy et al. [39] in comparison to the trajectories of firebrands of the same initial properties calculated by the FDS model

worked out in this manuscript is shown in Figure 39. Figure 40 shows the trajectories of the same brands in the horizontal plane. Sardoy et al. [39] only show a single trajectory per firebrand of the same density, thickness and initial diameter. The results obtained in the simulations of this work did, however, show many different trajectories and hence each particle configuration is represented with five trajectories to give an impression of the landing points. Particles of the same colour refer to the same thickness and density but different diameters. Some firebrands are stopped from being drawn at X = 880 m, because the computational domain was originally derived from the expectations for landing distances from [39] and it was not foreseen that the results would show deviations in the landing distance to that extent. The domain was extended for future studies to 1000 m in the X-direction.

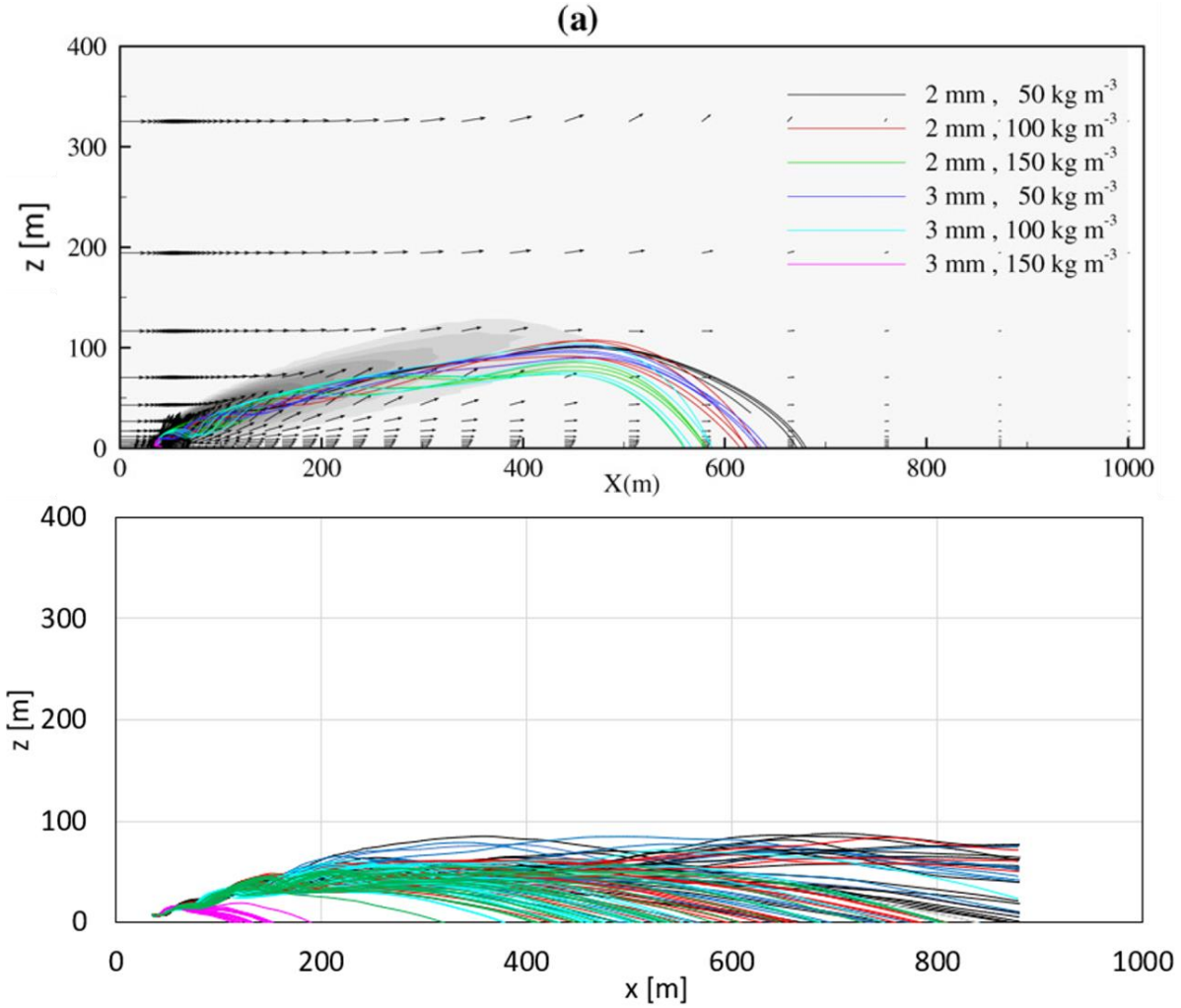

Figure 39: Firebrand trajectories in the vertical plane for a fire intensity of 10 MW/m and wind speed of 6.7 m/s, launched from the top of the canopy. The trajectories in the top graph are results by Sardoy et al. [39]. The bottom graphic represents results from this work.

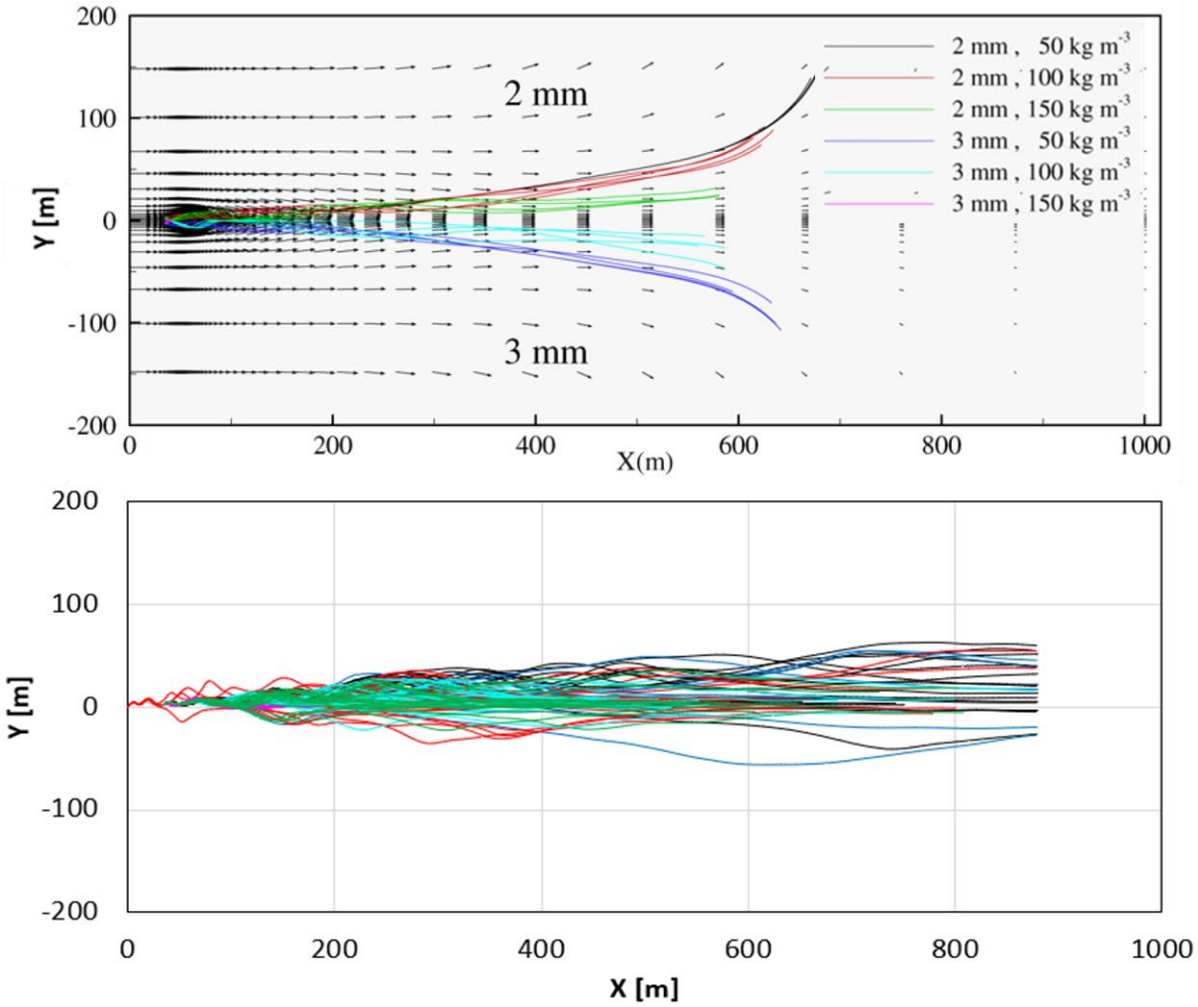

Figure 40: Firebrand trajectories in the horizontal plane as reported by Sardoy et al. [39] (top) and obtained from FDS simulations (bottom).

The trajectories show that the FDS simulation of this work predicts longer travel distances than the model that is developed in [39]. There are two reasons for this behaviour. First, obviously, the present model does not consider loss of volume or mass loss of firebrands at later stages due to char oxidation. But more importantly is the different approach towards pyrolysis. Figure 41 shows how the mass and the surface temperature of firebrands evolve in the present study and in the study from Sardoy et al. [39]. The wind speed in the study of the present work was 10 mph or 6.7 m/s, while it was 15 mph for the brands that are shown in the graph from [39]. However, the influence of the wind on the pyrolysis of the firebrands is disregarded here as it is assumed to be minor, especially since the relative velocity between the particle and the wind should be close to 0 (see chapter 2.2). Two different behaviours can be observed. The mass loss occurs significantly faster in this study than for the firebrands in [39]. Also, the surface temperature reduces at a faster rate. The virgin material of the firebrand seems to be consumed almost at once in the pyrolysis model employed in this work. This is not surprising as the initial temperature of the particles was chosen to be equal to the local gas temperature. In [39], on the contrary, the firebrands were reported to be initially at the temperature of the ambient gas (300 K). Looking at Figure 41 the brands seemed to heat up almost instantaneously

when exposed to the fire. The particle temperature is, however, limited in [39] and not controlled by heat transfer and reaction kinetics, but chosen to be constant at 720°C during pyrolysis following the approach in modelling by Tse & Fernandez-Pello [37]. This could also explain the sudden drop when the temperature is not prescribed anymore but may develop freely according to heat released from char oxidation and heat loss to the ambient. The idea of a constant temperature during pyrolysis is derived from experiments by Ohlemiller [81] who investigated smoldering combustion propagation on wood. The experiments he considered were composed of a stand that consisted of wood samples that were 6.4 cm thick and relatively long and wide and should be in a region where they can be regarded as thermally thick. The peak surface temperature that was recorded from this set of experiments for the parts in which the smoldering combustion transitioned to flaming was taken in [39] as the constant temperature of firebrands during pyrolysis. A discussion on how the temperature is applicable to the problem of firebrands is not carried out in [39] or [37].

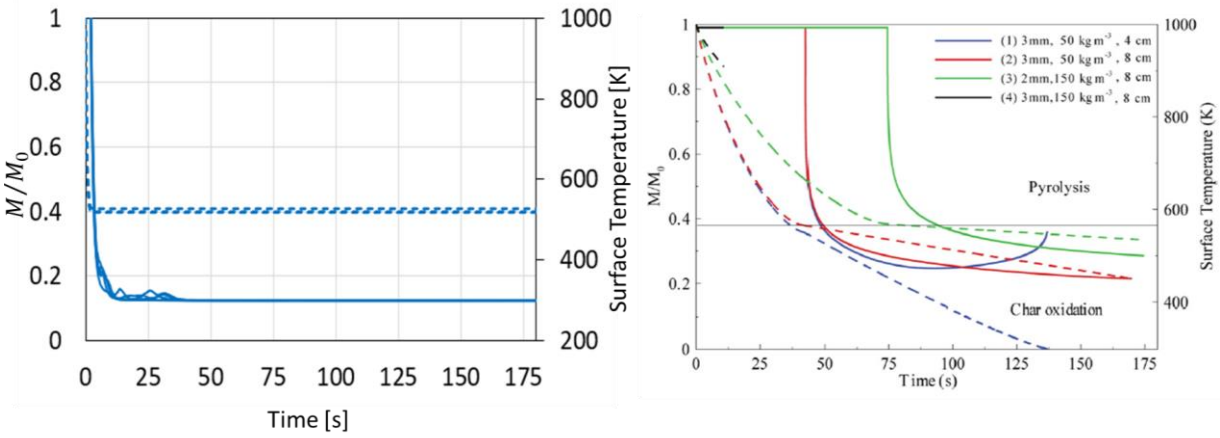

Figure 41: Mass loss (dashed lines) and surface temperature (solid lines) of firebrands in the present study (left graph) and in [39] (right graph). The blue color on the left refers to similar properties as stated in the right graph.

The decision for the FDS model of this work was following the philosophy that the surface temperature is rather an output of the reaction kinetics and the pyrolysis model than an input to prescribe. Therefore, a fixed temperature was not employed. As a result, the particles follow the trend that were already observed for the single particle burning tests in section 5.2 where particles initially at 900°C already showed very high peak HRR and then seemed to be burned out within a second or two. In the present case the firebrands are released at even higher temperatures of 1044°C (the local gas temperature at the point of release) and are not cooling down in an environment of 20°C but are subjected to further heat from the fire and the hot gases in the plume. This amplifies the observed behaviour for high initial temperatures and the firebrands tend to char completely within seconds. From this point of view, this explains how the firebrands end up travelling farther. As they lose about 61% of their mass by charring of the virgin material within the first seconds after being released, they are much lighter than the

firebrands considered in [39]. With significantly less mass but the same size, it is not surprising that the particles will be transported over longer distances.

The above discussion also implies that far travelling firebrands might not be those that can be analysed properly from the numerical model of this work without any consideration of char oxidation. Char oxidation is expected to influence the travel distance as the particle keeps losing mass but also volume to this process. Firebrands from this work will be predicted to enter a smoldering state much earlier than in [39] as the virgin mass is decomposed much quicker. Even though the smoldering itself will not be further addressed, it can be assumed that a firebrand that is fully charred and has completely pyrolyzed all virgin material will enter a smoldering, glowing state next. Hence, mostly short-travelling firebrands with greater thickness or density might make it to the ground still being in a pyrolyzing, and also flaming, state. This leads to another consideration where the criterion previously established in section 5.2 of a surface temperature of 100°C as the threshold value for the end of pyrolysis needs to be questioned.

This specific surface temperature was observed from tests where hot firebrands are exposed to ambient gases at 20°C for cooling. As mentioned above, the fire and the hot gases form a different situation as heat losses from the firebrand will occur at a slower rate as the temperature gradient between the firebrand and the ambient is smaller which linearly influences the convective heat transfer (equation (3-4)). As a result, this criterion cannot be upheld anymore, because the local temperatures that the firebrands are subjected to in the plume are fluctuating, a significant temperature that is found for one firebrand might change for the next one. It makes more sense to assess ongoing pyrolysis reactions by looking at the mass loss of the firebrands. Figure 42 shows the mass loss for firebrands of different thickness over time from the normalized mass of the firebrands. A line that is stopped being drawn indicates that the brand has touched the ground. Figure 43 shows the temperatures of these brands. The different scales on the x-axis should be noted when comparing the two properties. The scales at which FDS records the mass cannot be chosen and can be on the order of $10^{-3}\ kg$ for some particles and $10^{-6}\ kg$ for others. However, the time scales before the particles get assigned a constant value by FDS because more detailed values are not tracked are very short and usually only a hand full on quickly decreasing numbers are available which does not allow for establishing a proper MLRPUA for the brands. As a result, pyrolysis is assumed to still go on while the curve shown in Figure 42 for firebrands of 200 kg/m³ density and 4 cm diameter is not yet showing a flat line for a particle. A similar approach is taken for all firebrands.

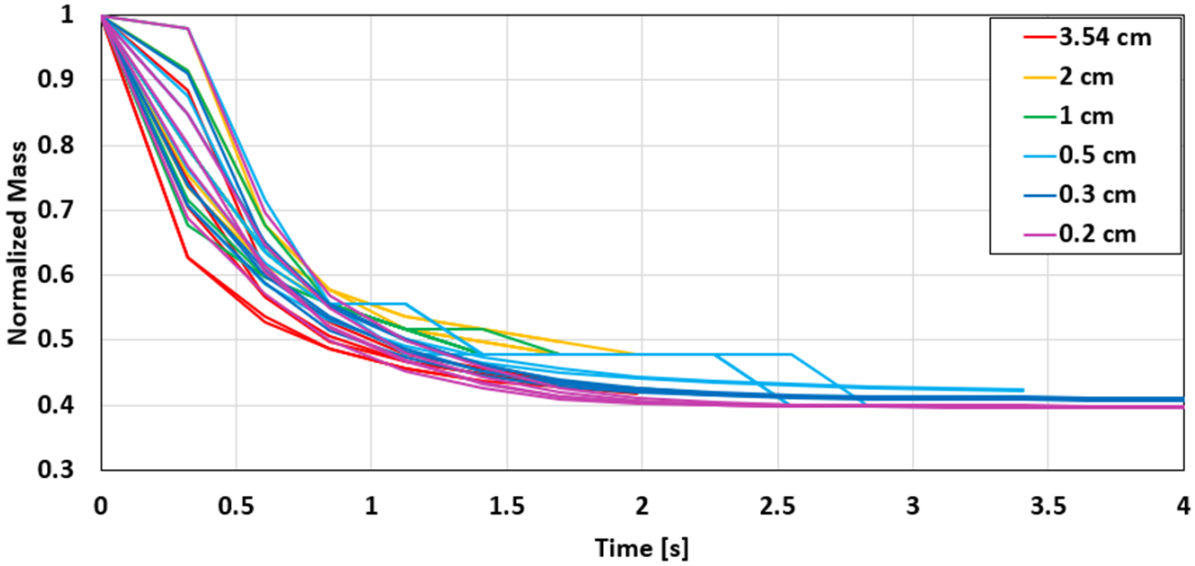

Figure 42: Normalized Mass of firebrands over time. Firebrands have a 4 cm diameter equivalent and an initial density of 200 kg/m³.

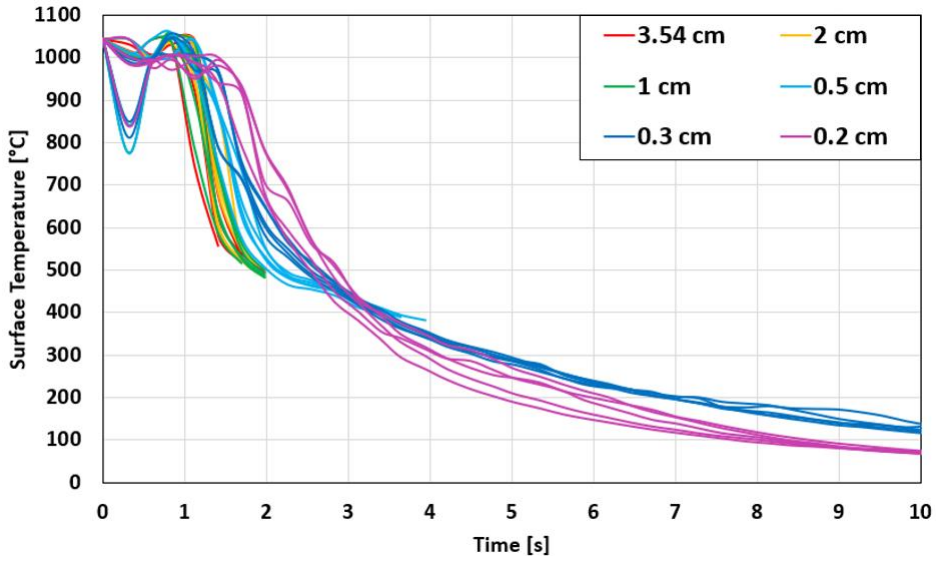

Figure 43: Surface Temperature of firebrands over time. (4 cm diameter equivalent; density: 200 kg/m³)

The latter graph shows that the surface temperatures of all particles is still over 400°C while the firebrands at that temperature do not show mass loss anymore and can be therefore assumed to be not pyrolyzing. This confirms that the mass loss criterion is the better choice for assessing the state of the firebrands. Moreover, in the temperature graph it is noticeable that the thicker brands cool down quicker than the thinner brands or, to be precise, earlier. This is because they are travelling in the plume for shorter times and fall to the ground and leave the layer of hot gases earlier. Sardoy et al. [39] present in their work a correlation of the product of thickness and density and the flying distance which becomes clear looking at Figure 44, where the landing distance over said product of initial density and thickness of a firebrand is shown. The results reported in [39] are shown on the top and the results from this work on the bottom.

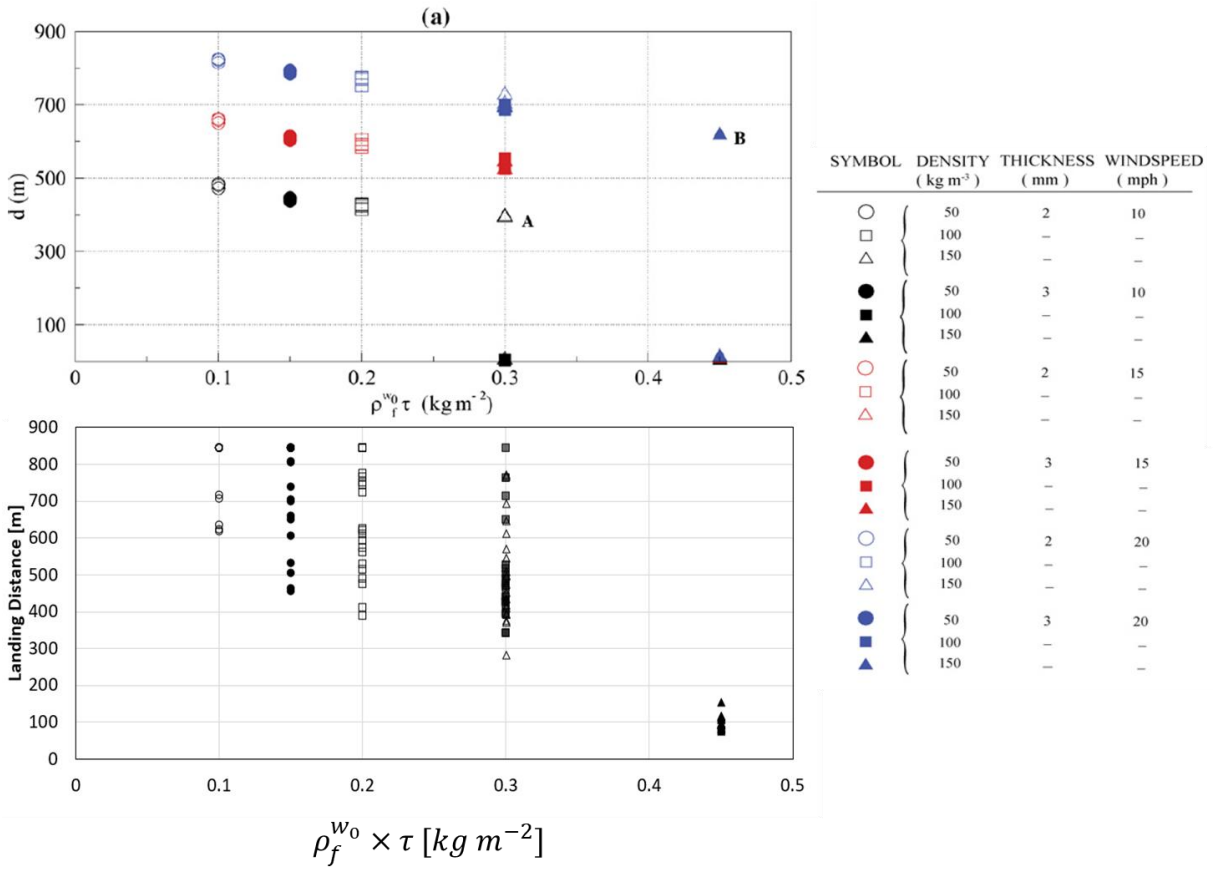

Figure 44: Landing distance of different firebrands over the product of initial thickness times density. The top graph is from [39] and considers different wind conditions. The bottom graph is presenting results from this work at 6.7 m/s only. In addition to the trends shown here, landing distances for larger values of $\rho \times \tau$ are reported in Figure 54 in Appendix F. In the bottom graph, firebrands that were transported beyond the end of the domain (X= 880 m) were assigned a landing distance of 845 m, which is the distance of the domain's end to the fire source. This was done to show the variance in the landing distances and not neglect these results. Therefore, values on the edge of 850 m indicate landing distances >845 m without further specification of the exact landing distance.

The graphic shows how the travel distances of firebrands decrease with increasing mass per area of the firebrand. The results reported by Sardoy et al. [39] show little variance in the landing distance for firebrands of the same mass per area, but only a hand full of values are reported and those are in compliance with the lower boundary of the values found in this study. Some firebrands that were simulated in the extended domain (up to 1 km downwind) were found to fly even further than that and stay in the air before they leave the domain for more than 130 seconds. Following the results from Figure 41, those brands would be expected to fully burn away in using the model in [39], which might be one reason why less firebrands are reported in [39] that show large landing distances.

The product of thickness and density seems to the most important property to define the initial characteristic of a firebrand. In agreement with Ref. [39] different regimes can be identified. In the first one, for small values of the product, the firebrands are lofted by the plume and transported downwind and in the other case, for larger values, the firebrands fall to the ground without being lofted but are blown downstream by the crosswind. Figure 46 gives the results that are obtained for firebrands of various values of this product between 0.1 and 8.86 kg/m².

The data was collected from simulations with firebrands of 4 cm diameter equivalent and densities of 50, 100 and 200 kg/m³ and thicknesses between 0.2 and 3.54 cm and firebrands of 10 cm diameter equivalent with a density of 100 kg/m³ and thicknesses between 0.2 and 8.87 cm. The largest thickness is always corresponding to an aspect ratio of 1, following the relation for disc-like geometries, since the particles get less and less “disc-like” with increasing thickness and this analogy would be overstretched when the particles are thicker than they are long and wide and would effectively become rods. The figure is shown in three parts with different scaling on the axis to allow for the trajectories of all depicted brands to be properly visible. It is evident how particles with a smaller product of thickness times density fly farther than others. Furthermore, a clear distinction between the firebrands that land shortly after the fire zone and between those that are lofted by the plume becomes visible. From the firebrands that were analyzed in this study, all brands that were not lofted fell to the ground still decreasing in mass and with rather high surface temperatures. They are considered to be still flaming, following the criterion for pyrolysis that has been established above. For values of $\rho_f^{w_0} \times \tau \geq 1$, all firebrands are found to touch the ground are in a flaming state. However, due to the considered thicknesses and densities, the next lowest value for which results were collected is $\rho_f^{w_0} \times \tau = 0.6$ and those firebrands are all lofted by the plume and do not show any sign of pyrolysis upon landing. The brands with $\rho_f^{w_0} \times \tau = 1$ were observed to be blown about 10 m downwind before they land and where they could subsequently cause secondary ignition. Firebrands of $\rho_f^{w_0} \times \tau = 0.6$ were observed to travel between 63 and 163 m downwind from the fire, while brands with a value of $\rho_f^{w_0} \times \tau = 2$ were all found to travel less than 3 m in the horizontal X-direction.

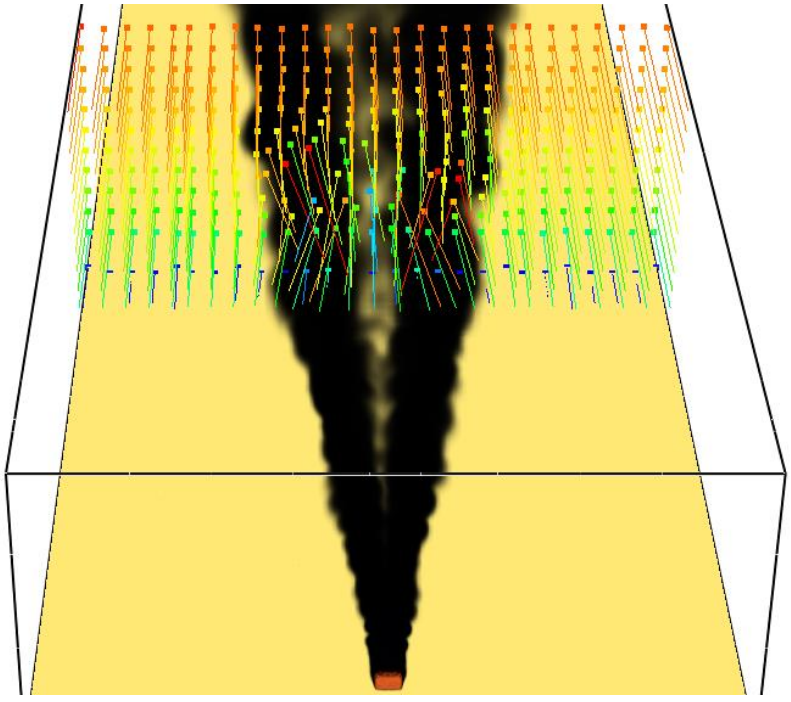

Figure 45: Velocity vectors at X = 352 m as calculated for the flow field of the present work.

The distances the firebrands travel in the Y-direction are found to be short close to the fire and increase with distance to the fire, which has also been reported in [39] and was shown in Figure 40, which is the due to stronger air entrainment effects into the plume close to the fire and large atmospheric flow structures appearing with distance to the fire. The shape of those structures resembles atmospheric eddies and is visible from the shape of the trajectories in the Z-plane depicted in Figure 40. The firebrands in the present study did not drift as far to the sides as reported in [39]. This drifting behaviour might be also a result from the flow field that was computed in [39] and is visible from the vectors in the graph on the top in Figure 40. The vectors show that the entire flow field in the domain seems to be drifting away from the smoke plume and diverge. Figure 45 shows an instantaneous picture of the velocity vectors from the present work in the plane X = 352 m over the entire height of the domain well after the fire developed steady state conditions. The vector field does not indicate a diverging flow towards the boundaries in the Y-direction. Even though the picture shows an instantaneous moment, a behaviour for the flow field as reported in [39] cannot be observed over the entire time of the simulation and only the region within the plume shows fluctuations following turbulence of the hot gases. The different velocity fields will impact the results on the landing distance of the particles. Firebrands that are forced out of the plume downwind due to the diverging flow will have shorter travel distances, while firebrands that keep travelling in the plume will be carried farther. It is not clear how the diverging flow emerges in the results presented by Sardoy et al. [39], where the issue is only addressed as emerging from convective structures.

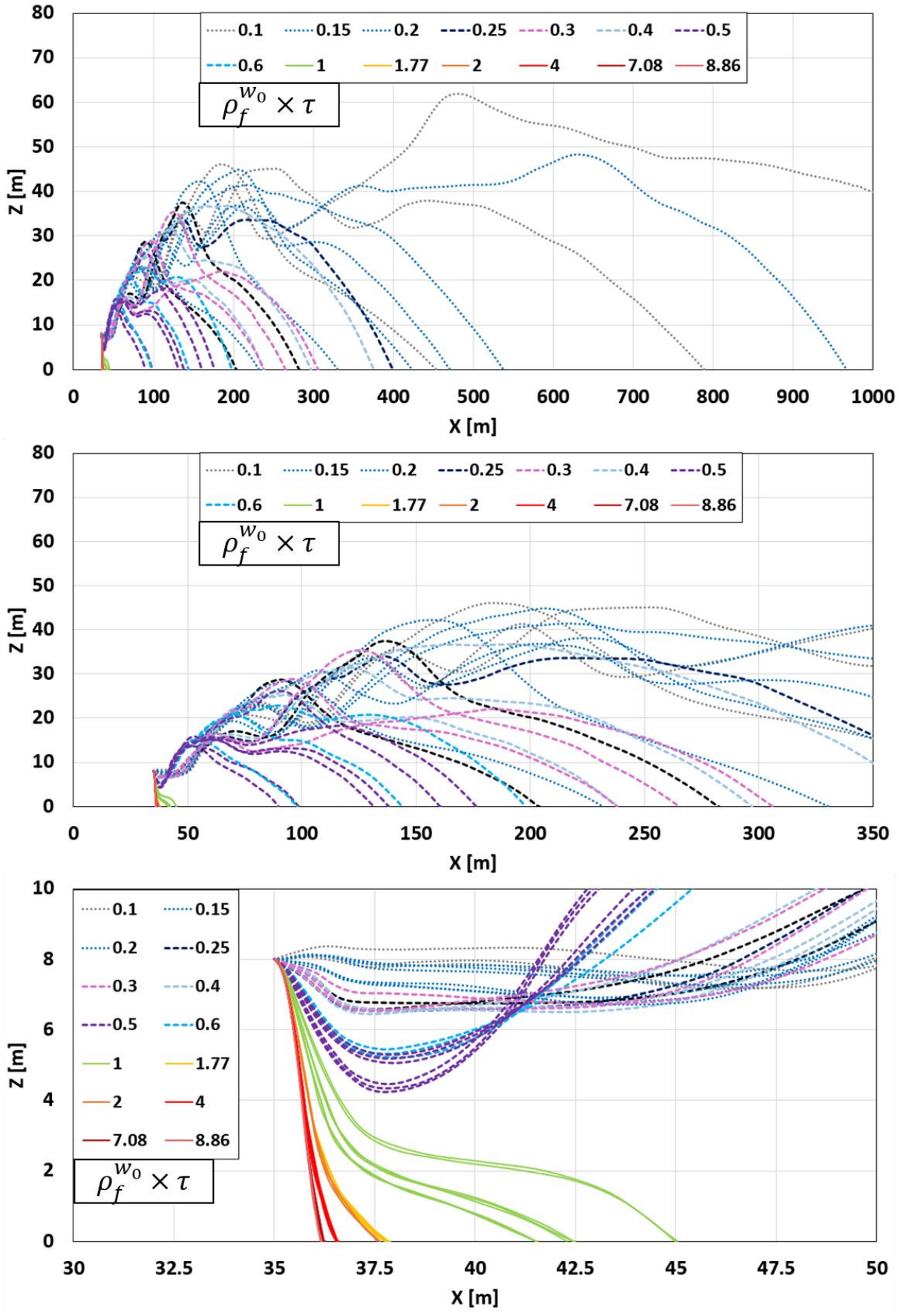

Figure 46: Trajectories of firebrands of different density, diameter and thickness. Dashed lines indicate that the firebrands are not losing mass anymore upon landing. Solid lines refer to brands that are currently losing mass while touching the ground. The brands are categorized using their product of initial density and thickness.

6 Conclusions

The present work reflects on the transportation of firebrands in large outdoor fire scenarios. Firebrand transport poses a large threat in wildland fire as it has the potential to increase the fire spread rate and also trap fire fighters between newly rising flame fronts by spotting ignition. In areas where the outdoor fires meet urban places, they can cause structures to ignite and pose a danger to life and property as well as to the environment in general.

The Fire Dynamics Simulator (FDS) is used to build the foundation to a numerical model that can be able to predict the flying paths and landing distances of firebrands from outdoor fires along with properties that indicated the state that the firebrands are in upon landing. The development of this work follows closely similar work by Sardoy et al. [39] who developed their own numerical model to approach the problem of firebrand transport. Due to time constraints of the project, char oxidation is only considered theoretically to ensure quick access to the most important facts to implement this feature into the model in the future. The work presented was carried out only considering the pyrolysis of firebrands instead. In simulations that resemble TGA test configurations the pyrolysis model was tested and the temperatures at which the pyrolysis rate peaks is found to correlate well with temperature values reported for the ignition of wood in the literature. The study of the pyrolysis model in single item tests is subsequently extended and fuel gas combustion is invoked. The model gives good agreement to what should be expected in the total amount of heat that is released from a single particle. Furthermore, the energy loss due to the generation of volatiles is visible in Figure 26 along with proper values for the mass loss or generation rates of the different species and materials.

The pyrolysis behaviour of firebrands from this model is analyzed using a configuration of initially hot firebrands that are exposed to an ambient temperature of 20°C. The initial hot temperature will initiate pyrolysis and combustion of the fuel gases. Three influencing parameters on the pyrolysis behaviour of the firebrands are found. The initial temperature, thickness and density of the firebrand. Lower initial temperatures lead to more sustained pyrolysis and hot surface temperatures, whereas higher initial temperatures lead to faster cooling of the particle by high reaction rates and high energy loss to the endothermic process. Longer sustained pyrolysis can issue a heat feedback from combustion of the fuel gases towards the firebrands for longer times, which amplifies this behaviour. Thicker particles are found to be longer pyrolyzing and cool down slower than thinner particles as a result of higher thermal inertia. The density has the same effect and also increases the absolute mass of fuel gas that can gasify from the firebrand per unit area which increases the HRR of a firebrand. The HRR of firebrands is taken as a measure for the pyrolysis rate of a particle as it directly translates to it. A threshold value of 0.1 kW is chosen as the point where pyrolysis is assumed to end. This value is found

to correspond well to a surface temperature of 100°C for all firebrands. As an alternative criterion, the total MLR of the solid is introduced and compared to the temperature criterion, where the latter is found to be overly conservative and still show pyrolysis where the MLR criterion would already assume the particle to not be flaming anymore.

In the simulation of the transportation of firebrands from the large outdoor fire, a fire intensity of 10 MW/m with a total strength of 100 MW is considered. Cross wind at 6.7 m/s is considered and firebrands between 50 kg/m² and 200 kg/m³ density, 4 cm and 10 cm diameter, and 0.2 cm and 8.87 cm thickness are considered which corresponds to aspect rations between 0.02 and 1. The firebrands are modelled as plates with rectangular bases to mimic discs. As they are found to travel the farthest from all geometries from previous studies.

The trajectories as they are calculated for firebrands by the FDS model of this work are much longer than those reported by [39]. The origin of this behaviour is in the difference of the pyrolysis model. This work assumes purely kinetic controlled pyrolysis rates that are modelled using a first order Arrhenius equation, whereas Ref. [39] employs additionally a maximum temperature for the firebrands of 720°C during pyrolysis. This increases the times for full pyrolysis of the particles significantly. Due to the high temperatures from the fire of 1044°C at the spot where the particles are released from the canopy, the firebrands lose almost all the mass of virgin material in the first few seconds after being released. The therefore almost initially reduced mass leads to increased landing distances. However, the general trend that the travel distance reduces with the product of initial density times thickness of a firebrand is not only visible but generally in some agreement which gets better for increasing values of $\rho_f^{w_o} \times \tau$. The landing distances are for $\rho_f^{w_o} \times \tau = 0.45$ show almost no variation compared to the results for $\rho_f^{w_o} \times \tau < 0.4$. Generally, the lower bound of the results for the landing distance is in very good agreement here to the results from [39], but only a very few single points are plotted in this analysis in [39]. The nature of LES resolving turbulent structures at certain scales might also enhance the effect of fluctuating appearances of singularities in the flow opposite RANS simulations as used in [39]. This could lead to more unique effects on single brands that entrains them back in the plume which subsequently results in large differences in the landing distance. The product $\rho_f^{w_o} \times \tau$ was found to be the dominating firebrand property associated with the transport of the particles.

By employing the mass loss criterion for flaming pyrolysis in a slightly modified way as the mass is not very accurately recorded for particles by FDS, the state of firebrands upon landing is analyzed. The units in which properties for particles are wished to be tracked in FDS cannot be chosen. Depending on the output value, FDS will give track the mass, for example, in kg or $10^{-3}\ kg$, where the latter gives more refined information on the mass loss. As a result, constant

curves can emerge for the normalized mass of a particle that still make a significant jump after some time, because of the detail in which the mass is recorded by FDS (compare Figure 41). The mass loss criterion can therefore be hardly applied to capture an actual threshold value, but the criterion needed to be adjusted that flaming pyrolysis is assumed while mass records from FDS still show significant mass loss.

Two kind of firebrands are distinguished. Those that are lofted by the plume and those that are blown downstream by cross wind but are not entrained in the upward plume. Firebrands with $\rho_f^{w_o} \times \tau \geq 1$ were found to be not entrained and firebrands with $\rho_f^{w_o} \times \tau \leq 0.6$ were found to be entrained. Moreover, all firebrands that would fall to the ground were still flaming when touching the ground, while a maximum travel distance of 10 m is observed. The minimum travel distance observed for entrained firebrands was approximately 50 m for a firebrand with $\rho_f^{w_o} \times \tau = 0.5$ shortly followed by more firebrands of $\rho_f^{w_o} \times \tau$ between 0.5 and 0.6.

The results shown in Figure 46 for the trajectories of the single firebrands and their landing distance were found to not be sensitive to the diameter of the firebrands. However, only small numbers of 10 cm diameter equivalent firebrands were compared (3-5 particles per thickness), but they show similar values in the flying distance as well as a similar variance in the distribution of these numbers. This fits the conclusion drawn in [39] were firebrands are said to be independent in their landing distance from their initial diameter.

For the future expansion of this numerical model, it is necessary to establish a way to properly validate the pyrolysis model. The model of the present work follows a different approach at some points than what is used in the study by [39] that was used as a comparison case, however it is not fully clear which approach might be more suitable for this problem. The validation used in [39] by employing the burning law by Albini that is presented in chapter 2.4 is a first step, however this burning law is a very major simplification to the problem of firebrands that can show flaming and smoldering combustion and is a linear regression where the data points scatter very much around the trend line. Estimating the proper reaction kinetics and then model the proper behaviour of the brands remains the major issue in these problems.

The current model allows the analysis of flaming brands and their landing distances from the fire and especially the region for $0.6 < \rho_f^{w_o} \times \tau < 1$ needs to be further investigated to come up with a more accurate estimate of the boundary that is separating the two regions of firebrands landing spots. Larger sampling numbers need to be considered for the findings to become statistically more significant as well. It might be beneficial to first work out a good way to process large amount of data as it is produced by FDS for tracked particles as it is a cumbersome and tedious process to read out the files and arrange the data manually in a proper form.

Different fire intensities should be included in future work as well. The wind velocity seems to linearly increase the landing distances as evident from the results in [39]. The fire intensity, however, has the potential to also influence the pyrolysis of the firebrands as the initial temperature can vary with that intensity as well as with the type of fire. Locally dense or less dens accumulations of vegetation can lead to spikes or lows in the local temperature and the rate of pyrolysis might show accordingly as shown for different initial temperatures.

The flow field as it is computed in the simulations should be reviewed in more detail as well. While the velocity vectors representing the flow field from the results in Ref. [39] unveiled a tendency to diverge towards the boundaries in the Y-direction, no such observation could be reported for the flow field as it emerged from the calculation in FDS in the present work. In general, the flow field followed well the wind in the x-direction that was prescribed. The velocity field was not closely monitored until this point in the discussion as it was not expected to show problems as the case of a fire plume in a free wind stream is relatively uncomplicated. However, the comparison of the results now shows that for the future work it needs to be investigated where the diverging behaviour reported in Ref. [39] emerges from and if the flow field computed by FDS and partially shown in the results from this work is the better solution as it does not show such trends.

Lastly, the char oxidation as it can be invoked via different ways in FDS should be given further consideration. The implementation of this feature will enable the possibility to also analyze firebrands that are lofted by the plume in regard of their properties over time in an accurate manner and predicting burn away times and the state that they are in upon landing, which could be smoldering or maybe self-extinguished, in which case the hot particle can still cause secondary ignition as presented in the theory of section 2.3.

In the very long run, once the combustion during transportation is resolved accurately, it could be tried to add the problem of secondary ignition from the landed firebrands to predict probabilities for the ignition of vegetative material or structures from firebrand showers or predict and show how scenarios can evolve from a large wildland fire. Consequently, the model could be developed into a tool to minimize the risks of loss of lives, property or destruction of environment associated with wildland fires.

Acknowledgements

I would like to express my gratitude to Professor Trouvé, my academic supervisor at the University of Maryland, for the patient guidance and constant support throughout the research work and for the many valuable and constructive discussions we had during this project as well as for the time he invested proofreading and helping improving the manuscript.

I would also like to thank Professor Merci, my academic supervisor from Ghent University, for closely monitoring the progress of the project and making sure that the project is right on track.

I would further like to thank all members of staff from the University of Maryland who made my research internship possible and also warmly welcomed me upon my arrival. All the valuable information and advice on the university and life in the US, and Maryland/Washington, D.C. in particular, was very much appreciated.

Moreover, the constant support from all members of the management board of the IMFSE programme has been noticed and I wish to say thank you for taking good care of our sanity during the current times of the pandemic and for closely monitoring the situation of all students and providing helpful information and constant support when questions arose. Special thanks need to be expressed here to Lies Decroos, the Erasmus Mundus Administrator of the IMFSE programme. Lies has been constantly available and supportive throughout the two years of study in the IMFSE porgramme to help students with literally every kind of questions, concerns or problems and her help is very much appreciated.

Lastly, I wish to acknowledge the financial support in form of a scholarship by the German Academic Exchange Service (DAAD) for my second year in the IMFSE programme.

7 References

[1] United States Government Accountability Office, Technology Assessment: Protecting Structures and Improving Communications During Wildland Fires, Washington, D.C., USA, 2005.

[2] O. Pechony, D.T. Shindell, Driving forces of global wildfires over the past millennium and the forthcoming century, Proc. Natl. Acad. Sci. U. S. A. 107 (45) (2010) 19167–19170. https://doi.org/10.1073/pnas.1003669107.

[3] F. Krikken, F. Lehner, K. Haustein, I. Drobyshev, G.J. van Oldenborgh, Attribution of the role of climate change in the forest fires in Sweden 2018, 2019.

[4] Province of British Columbia, 2017 Wildfire Season Summary, Canada. https://www2.gov.bc.ca/gov/content/safety/wildfire-status/about-bcws/wildfire-history/wildfire-season-summary (accessed 12 February 2020).

[5] J. San-Miguel-Ayanz, T. Durrant, R. Boca, G. Libertà, A. Branco, D. de Rigo, D. Ferrari, P. Maianti, T.A. Vivancos, D. Oom, H. Pfeiffer, D. Nuijten, T. Leray, A. Benchikha, M. Abbas, F. Humer, H. Vacik, M. Müller, V. Konstantinov, I. Pešut, A. Kaliger, S. Petkoviček, K. Papageorgiou, I. Toumasis, J. Pecl, R. Ruuska, F. Chassagne, P. Joannelle, A. Gonschorek, C. Theodoridou, P. Debreceni, D. Nagy, C. Nugent, A.B. Zaken, M. Di Fonzo, R. Sciunnach, G. Micillo, G. Fresu, M. Marzoli, D. Ascoli, E. Leisavnieks, Z. Jaunķlķis, G. Mitri, S. Repšienė, Z. Glazko, F. Assali, H. Mharzi Alaoui, E. Kok, C. Stoof, A.-J. van Maren, M. Timovska, D. Botnen, J. Piwnicki, R. Szczygieł, J. Moreira, T. Pereira, M. Cruz, R. Sbirnea, S. Mara, A. Eritsov, V. Longauerová, J. Jakša, A. Lopez-Santalla, L. Sandahl, S. Beyeler, M. Conedera, B. Pezzatti, K.T. Dursun, U. Baltaci, R. Gazzard, A. Moffat, S. Sydorenko, Forest fires in Europe, Middle East and North Africa 2018, Publications Office of the European Union, Luxembourg, 2019.

[6] R. Lidskog, J. Johansson, D. Sjödin, Wildfires, responsibility and trust: Public understanding of Sweden's largest wildfire, Scandinavian Journal of Forest Research 34 (4) (2019) 319–328. https://doi.org/10.1080/02827581.2019.1598483.

[7] E.R. Galea (Editor), Proceedings of workshop: 'Wildfire: Human Behaviour and Evacuation Modelling GEO-SAFE Workshop 2020', London, UK, 20th 2020.

[8] The University of Sydney, More than one billion animals killed in Australian bushfires: Update on number of animals killed in Australian bushfires: Sydney expert, Sydney, Australia, 8th of 2020. https://sydney.edu.au/news-opinion/news/2020/01/08/australian-bushfires-more-than-one-billion-animals-impacted.html (accessed 12 February 2020).

[9] S.L. Manzello, A. Maranghides, W.E. Mell, Firebrand generation from burning vegetation, Int. J. Wildland Fire 16 (4) (2007) 458. https://doi.org/10.1071/WF06079.

[10] T.E. Watermann, Experimental study of firebrand generation: Final Technical Report, Project J6130, Chicago, IL, 1969.

[11] F.A. Albini, Spot Fire Distance From Burning Trees: A Predictive Model, Ogden, UT, USA, 1979.

[12] S.L. Manzello, J.R. Shields, J.C. Yang, Y. Hayashi, D. Nii, On the use of a firebrand generator to investigate the ignition of structures in wildland-urban interface (WUI) fires, in: Proceedings of the 11th International Conference on Fire Science and Engineering (INTERFLAM), London, 2007, pp. 861–872.

[13] A. Tohidi, N. Kaye, W. Bridges, Statistical description of firebrand size and shape distribution from coniferous trees for use in Metropolis Monte Carlo simulations of firebrand flight distance, Fire Safety Journal 77 (2015) 21–35. https://doi.org/10.1016/j.firesaf.2015.07.008.

[14] W.G. Bell, The great fire of London in 1666, Endeavour PressLtd, Lexington, KY, 2016.

[15] E. Koo, P.J. Pagni, D.R. Weise, J.P. Woycheese, Firebrands and spotting ignition in large-scale fires, Int. J. Wildland Fire 19 (7) (2010) 818. https://doi.org/10.1071/WF07119.

[16] C.S. Tarifa, P.P. Del Notario, F.G. Moreno, A.R. Villa, TRANSPORT AND COMBUSTION OF FIREBRANDS, Madrid, 1967.

[17] R.A. Anthenien, S.D. Tse, A. Carlos Fernandez-Pello, On the trajectories of embers initially elevated or lofted by small scale ground fire plumes in high winds, Fire Safety Journal 41 (5) (2006) 349–363. https://doi.org/10.1016/j.firesaf.2006.01.005.

[18] A. Tohidi, N.B. Kaye, Stochastic modeling of firebrand shower scenarios, Fire Safety Journal 91 (2017) 91–102. https://doi.org/10.1016/j.firesaf.2017.04.039.

[19] S.L. Manzello, T.G. Cleary, J.R. Shields, A. Maranghides, W. Mell, J.C. Yang, Experimental investigation of firebrands: Generation and ignition of fuel beds, Fire Safety Journal 43 (3) (2008) 226–233. https://doi.org/10.1016/j.firesaf.2006.06.010.

[20] S.L. Manzello, A. Maranghides, J.R. Shields, W.E. Mell, Y. Hayashi, D. Nii, MEASUREMENT OF FIREBRAND PRODUCTION AND HEAT RELEASE RATE (HRR) FROM BURNING KOREAN PINE TREES, 2007.

[21] S.L. Manzello, A. Maranghides, J.R. Shields, W.E. Mell, Y. Hayashi, D. Nii, Mass and size distribution of firebrands generated from burning Korean pine (Pinus koraiensis) trees, Fire Mater. 33 (1) (2009) 21–31. https://doi.org/10.1002/fam.977.

[22] C.S. Tarifa, P.P.d. Notario, F.G. Moreno, On the flight paths and lifetimes of burning particles of wood, Symposium (International) on Combustion 10 (1) (1965) 1021–1037. https://doi.org/10.1016/S0082-0784(65)80244-2.

[23] S.-L. Lee, J.M. Hellman, Study of firebrand trajectories in a turbulent swirling natural convection plume, Combustion and Flame 13 (6) (1969) 645–655. https://doi.org/10.1016/0010-2180(69)90072-8.

[24] S.C. Bunting, H.A. Wright, Ignition Capabilities of Non-Flaming Firebrands, Journal of Forestry 72 (10) (1974) 646–649.

[25] A.C. Fernandez-Pello, Wildland fire spot ignition by sparks and firebrands, Fire Safety Journal 91 (2017) 2–10. https://doi.org/10.1016/j.firesaf.2017.04.040.

[26] S.E. Caton-Kerr, A. Tohidi, M.J. Gollner, Firebrand Generation From Thermally-Degraded Cylindrical Wooden Dowels, Front. Mech. Eng. 5 (2019) 2167. https://doi.org/10.3389/fmech.2019.00032.

[27] S.L. Manzello, S. Suzuki, Y. Hayashi, Enabling the study of structure vulnerabilities to ignition from wind driven firebrand showers: A summary of experimental results, Fire Safety Journal 54 (2012) 181–196. https://doi.org/10.1016/j.firesaf.2012.06.012.

[28] S. Suzuki, S.L. Manzello, M. Lage, G. Laing, Firebrand generation data obtained from a full-scale structure burn, Int. J. Wildland Fire 21 (8) (2012) 961. https://doi.org/10.1071/WF11133.

[29] S. Suzuki, A. Brown, S.L. Manzello, J. Suzuki, Y. Hayashi, Firebrands generated from a full-scale structure burning under well-controlled laboratory conditions, Fire Safety Journal 63 (2014) 43–51. https://doi.org/10.1016/j.firesaf.2013.11.008.

[30] S. Suzuki, S.L. Manzello, Characteristics of Firebrands Collected from Actual Urban Fires, Fire Technol. 54 (2018). https://doi.org/10.1007/s10694-018-0751-x.

[31] F.J. Vodvarka, Firebrand Field Studies--Final Report, Chicago, IL, USA, 1969.

[32] F.J. Vodvarka, Urban burns - full-scale field studies -- Final Report, Chicago, IL, USA, 1970.

[33] A. Tohidi, N.B. Kaye, Comprehensive wind tunnel experiments of lofting and downwind transport of non-combusting rod-like model firebrands during firebrand shower scenarios, Fire Safety Journal 90 (2017) 95–111. https://doi.org/10.1016/j.firesaf.2017.04.032.

[34] J.P. Woycheese, Wooden Disk Combustion for Spot Fire Spread, in: Proceedings of the 9th International Interflam Conference, Edinburgh, UK, Interscience Communications Ltd, London, UK, 2001, pp. 101–112.

[35] C.S. Tarifa, P.P. Del Notario, A.R. Villa, L. Martinez, O. Perez, Open Fires and Transport of Firebrands. First Annual Report, Madrid, Spain, 1965.

[36] A. Simeoni, Wildland fires, in: M.J. Hurley, D.T. Gottuk, J.R. Hall Jr., K. Harada, E.D. Kuligowski, M. Puchovsky, J.L. Torero, J.M. Watts Jr., C.J. WIECZOREK (Eds.), SFPE Handbook of Fire Protection Engineering (5th Edition), Springer, New York, 2016, pp. 3283–3302.

[37] S.D. Tse, A. Fernandez-Pello, On the flight paths of metal particles and embers generated by power lines in high winds—a potential source of wildland fires, Fire Safety Journal 30 (4) (1998) 333–356. https://doi.org/10.1016/S0379-7112(97)00050-7.

[38] J.G. Quintiere, Fundamentals of fire phenomena, Wiley, Chichester, 2006.

[39] N. Sardoy, J.L. Consalvi, B. Porterie, A.C. Fernandez-Pello, Modeling transport and combustion of firebrands from burning trees, Combustion and Flame 150 (3) (2007) 151–169. https://doi.org/10.1016/j.combustflame.2007.04.008.

[40] B. Karlsson, J.G. Quintiere (Eds.), Enclosure fire dynamics, CRC Press, Boca Raton, Florida, USA, 2000.

[41] V. Babrauskas, Ignition handbook: Principles and applications to fire safety engineering, fire investigation, risk management and forensic science, Fire Science Publishers, Issaquah, Wash., 2003.

[42] D. Drysdale (Ed.), An introduction to fire dynamics, 3rd ed., Wiley, Hoboken, NJ, 2011.

[43] J.L. Torero, Flaming Ignition of Solid Fuels, in: M.J. Hurley, D.T. Gottuk, J.R. Hall Jr., K. Harada, E.D. Kuligowski, M. Puchovsky, J.L. Torero, J.M. Watts Jr., C.J. WIECZOREK (Eds.), SFPE Handbook of Fire Protection Engineering (5th Edition), Springer, New York, 2016, pp. 633–661.

[44] J.L. Torero, "Ignition". In-house hand-out, based on Chapter 11 of the SFPE Handbook (5th Ed.), Edinburgh, UK, 2019.

[45] R.M. Hadden, S. Scott, C. Lautenberger, A.C. Fernandez-Pello, Ignition of Combustible Fuel Beds by Hot Particles: An Experimental and Theoretical Study, Fire Technol 47 (2) (2011) 341–355. https://doi.org/10.1007/s10694-010-0181-x.

[46] B.F. Gray, Spontaneous Combustion and Self-Heating, in: M.J. Hurley, D.T. Gottuk, J.R. Hall Jr., K. Harada, E.D. Kuligowski, M. Puchovsky, J.L. Torero, J.M. Watts Jr., C.J. WIECZOREK (Eds.), SFPE Handbook of Fire Protection Engineering (5th Edition), Springer, New York, 2016, pp. 604–632.

[47] U.I. Gol'dshleger, K.V. Pribytkova, V.V. Barzykin, Ignition of a condensed explosive by a hot object of finite dimensions, Combust Explos Shock Waves 9 (1) (1973) 99–102. https://doi.org/10.1007/BF00740368.

[48] S.L. Manzello, S. Suzuki, Experimental investigation of wood decking assemblies exposed to firebrand showers, Fire Safety Journal 92 (2017) 122–131. https://doi.org/10.1016/j.firesaf.2017.05.019.

[49] S.L. Manzello, S. Suzuki, D. Nii, Full-Scale Experimental Investigation to Quantify Building Component Ignition Vulnerability from Mulch Beds Attacked by Firebrand Showers, Fire Technol. 53 (2) (2017) 535–551. https://doi.org/10.1007/s10694-015-0537-3.

[50] S.L. Manzello, T.G. Cleary, J.R. Shields, J.C. Yang, On the ignition of fuel beds by firebrands, Fire Mater. 30 (1) (2006) 77–87. https://doi.org/10.1002/fam.901.

[51] A. Witkowski, A. Stec, T.R. Hull, Thermal Decomposition of Polymeric Materials, in: M.J. Hurley, D.T. Gottuk, J.R. Hall Jr., K. Harada, E.D. Kuligowski, M. Puchovsky, J.L. Torero, J.M. Watts Jr., C.J. WIECZOREK (Eds.), SFPE Handbook of Fire Protection Engineering (5th Edition), Springer, New York, 2016, pp. 167–254.

[52] B. Porterie, J.L. Consalvi, A. Kaiss, J.C. Loraud, PREDICTING WILDLAND FIRE BEHAVIOR AND EMISSIONS USING A FINE-SCALE PHYSICAL MODEL, Numerical Heat Transfer, Part A: Applications 47 (6) (2005) 571–591. https://doi.org/10.1080/10407780590891362.

[53] G. Rein, Smoldering Combustion, in: M.J. Hurley, D.T. Gottuk, J.R. Hall Jr., K. Harada, E.D. Kuligowski, M. Puchovsky, J.L. Torero, J.M. Watts Jr., C.J. WIECZOREK (Eds.), SFPE Handbook of Fire Protection Engineering (5th Edition), Springer, New York, 2016, pp. 581–603.

[54] A. Muraszew, W.K. Fedele, Firebrand Investigation: Report ATR-75 7470-1. The Aerespace Corp., 1975.

[55] B. Merci, T. Beji, Fluid mechanics aspects of fire and smoke dynamics in enclosures, CRC Press Taylor & Francis Group a Balkema book, Boca Raton, London, New York, Leiden, 2016.

[56] K.B. McGrattan, S. Hostikka, R. McDermott, J. Floyd, M. Vanella, Fire Dynamics Simulator: Technical Reference Guide - Volume 1: Mathematical Model. Sixth Edition, NIST Special Publication 1018-1, National Institute of Standards and Technology, Gaithersburg, MD, 2004.

[57] J.H. Ferziger, M. Perić, Computational Methods for Fluid Dynamics, Springer Berlin Heidelberg, Berlin, Heidelberg, s.l., 2002.

[58] R. Schwarze, CFD-Modellierung: Grundlagen und Anwendungen bei Strömungsprozessen, Springer, Berlin, Heidelberg, 2013.

[59] J. Welty, G.L. Rorrer, D.G. Foster, Fundamentals of Momentum, Heat, and Mass Transfer, Revised 6th Edition, 6th ed., Wiley, New York, 2014.

[60] A.M. Grishin, General mathematical model for forest fires and its applications, Combust Explos Shock Waves 32 (5) (1996) 503–519. https://doi.org/10.1007/BF01998573.

[61] Fuel Properties and Combustion Data, in: M.J. Hurley, D.T. Gottuk, J.R. Hall Jr., K. Harada, E.D. Kuligowski, M. Puchovsky, J.L. Torero, J.M. Watts Jr., C.J. WIECZOREK (Eds.), SFPE Handbook of Fire Protection Engineering (5th Edition), Springer, New York, 2016, pp. 3437–3475.

[62] Fire Plumes and Flame Heights, in: B. Karlsson, J.G. Quintiere (Eds.), Enclosure fire dynamics, CRC Press, Boca Raton, Florida, USA, 2000.

[63] L.-M. Yuan, G. Cox, An experimental study of some line fires, Fire Safety Journal 27 (2) (1996) 123–139. https://doi.org/10.1016/S0379-7112(96)00047-1.

[64] G.H. Yeoh, Computational fluid dynamics in fire engineering: Theory, modelling und practice, Butterworth-Heinemann, Burlington (Ma), 2009.

[65] C.J. Freitas, The issue of numerical uncertainty, Applied Mathematical Modelling 26 (2) (2002) 237–248. https://doi.org/10.1016/S0307-904X(01)00058-0.

[66] K.B. McGrattan, S. Hostikka, R. McDermott, J. Floyd, M. Vanella, Fire Dynamics Simulator: User's Guide. Sixth Edition, NIST Special Publication 1019, National Institute of Standards and Technology, Gaithersburg, MD, 2004.

[67] D. Morvan, J.L. Dupuy, Modeling the propagation of a wildfire through a Mediterranean shrub using a multiphase formulation, Combustion and Flame 138 (3) (2004) 199–210. https://doi.org/10.1016/j.combustflame.2004.05.001.

[68] M. El Houssami, E. Mueller, A. Filkov, J.C. Thomas, N. Skowronski, M.R. Gallagher, K. Clark, R. Kremens, A. Simeoni, Experimental Procedures Characterising Firebrand Generation in Wildland Fires, Fire Technol 52 (3) (2016) 731–751. https://doi.org/10.1007/s10694-015-0492-z.

[69] A.M. Obukhov, Turbulence in an atmosphere with a non-uniform temperature, Boundary-Layer Meteorol 2 (1) (1971) 7–29. https://doi.org/10.1007/BF00718085.

[70] A.J. Dyer, A review of flux-profile relationships, Boundary-Layer Meteorol 7 (3) (1974) 363–372. https://doi.org/10.1007/BF00240838.

[71] C. Di Blasi, Processes of flames spreading over the surface of charring fuels: Effects of the solid thickness, Combustion and Flame 97 (2) (1994) 225–239. https://doi.org/10.1016/0010-2180(94)90006-X.

[72] K.M. Bryden, K.W. Ragland, C.J. Rutland, Modeling thermally thick pyrolysis of wood, Biomass and Bioenergy 22 (1) (2002) 41–53. https://doi.org/10.1016/S0961-9534(01)00060-5.

[73] B. Trettel, R. McDermott, Matlab function to read the FDS 'part' file (*.prt5): read_prt5.m, 2011. https://github.com/firemodels/fds/blob/master/Utilities/Matlab/scripts/read_prt5.m (accessed April 27th 2020).

[74] E.C. Bixel, H.J. Moore, Are fires caused by steam pipes. (B. S. thesis), Case School of Applied Science, Pittsburgh (1910).

[75] Y. Li, D.D. Drysdale, Measurement of the ignition temperature of wood, Fire Safety Science 1 (1992) 380–385.

[76] A. Atreya, I.S. Wichman, Heat and Mass Transfer During Piloted Ignition of Cellulosic Solids, Journal of Heat Transfer 111 (3) (1989) 719–725. https://doi.org/10.1115/1.3250742.

[77] C.H. Bamford, J. Crank, D.H. Malan, The combustion of wood. Part I, Math. Proc. Camb. Phil. Soc. 42 (2) (1946) 166–182. https://doi.org/10.1017/S030500410002288X.

[78] J.L. de Ris, M.M. Khan, A sample holder for determining material properties, Fire Mater. 24 (5) (2000) 219–226. https://doi.org/10.1002/1099-1018(200009/10)24:5<219:AID-FAM741>3.0.CO;2-7.

[79] D.D. Drysdale, H.E. Thomson, Flammability of plastics II: Critical mass flux at the fire-point, Fire Safety Journal 14 (3) (1989) 179–188. https://doi.org/10.1016/0379-7112(89)90071-4.

[80] S.J. Melinek, Fire Research Note No. 755: Ignition Behaviour of Heated Wood Surfaces, Borehamwood, England, 1969.

[81] T.J. Ohlemiller, Smoldering Combustion Propagation on Solid Wood, in: G. Cox, B. Langford (Eds.), Fire Safety Science: Proceedings of the third international Symposium, Taylor and Francis, Hoboken, 1991, pp. 565–574.

Appendix A: Radial Profiles of the Plume at 10 m and 35 m height

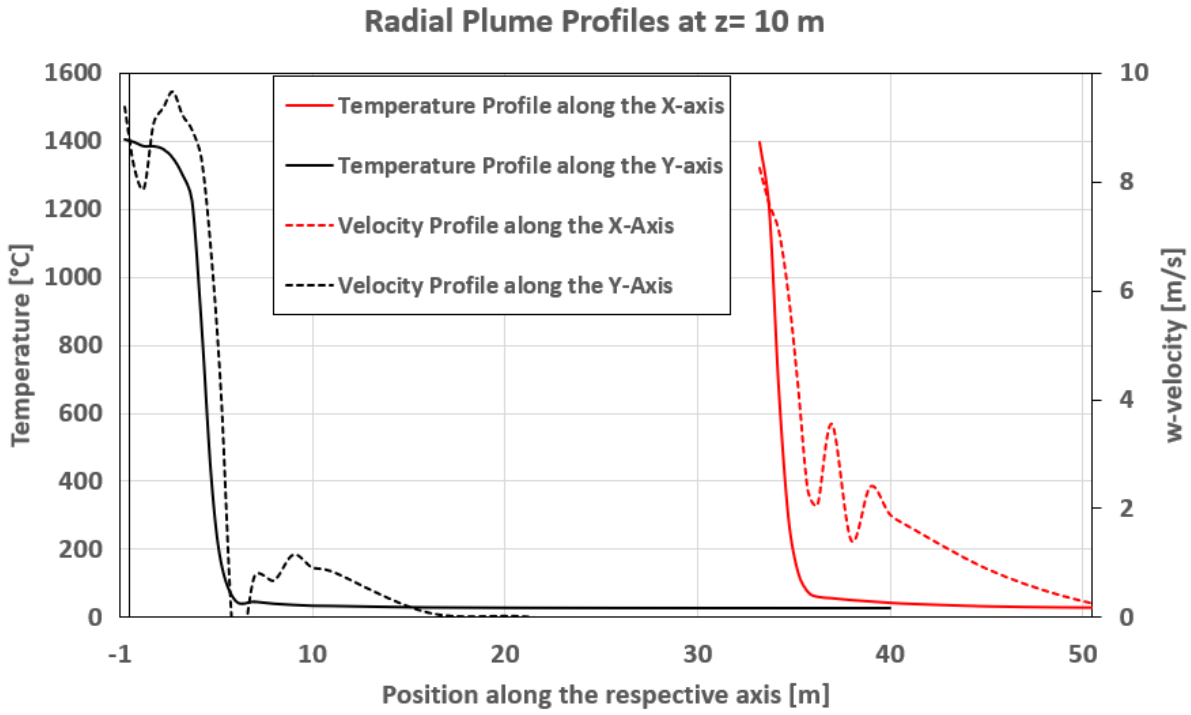

Figure 47: Radial Profile of the Plume in X and Y direction at z=10m.

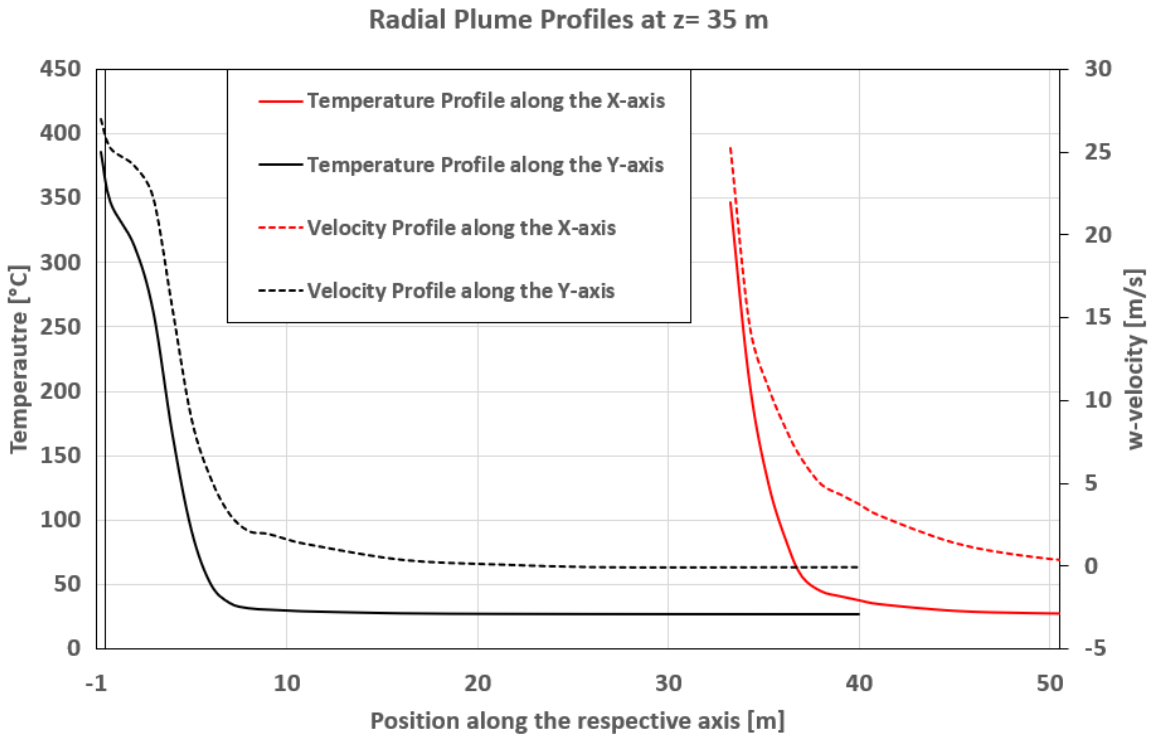

Figure 48: Radial Profile of the Plume in X and Y direction at z=35m.

The radial profiles of the fire plume as it is implemented in the numerical model at two different heights are depicted in Figure 47 and Figure 48. From the graphs, it can be seen how the plume widens with height as the temperature and velocity drops towards the outside of the plume are less steep at higher elevations. The center point of the fire that is considered in this

study lays at $X = 32.5$ and $Y = 0.0$, which would be expected to be the centerline of the fire when comparing it to the characteristics of an axisymmetric fire. However, both graphs show higher values in velocity and temperature at a position measured at $X = 32.5\ and\ Y = -0.25$. This indicates that the line at which the fire shows the highest temperatures and velocities might be slightly offset from the center point. This might be a result of the randomly distributed fuel particles in the region of the fire, which are not aligned cell centered and thus in an ununiform random pattern. This ununiform pattern of the particles, does allow for fluctuations in peak values over the fire regions, however, the largest values are still expected close to the center, where the plume is being fed from combined fuel gas sources, i.e. many particles releasing combusting fuel gas.

Appendix B: FDS Input File

```
&HEAD CHID='Results100', TITLE='Results100'/
&MISC TMPA=26.85/
&PRES MAX_PRESSURE_ITERATIONS=100 /
&TIME T_END= 300.0, WALL_INCREMENT=1 /


+++++MESH TOTAL++++ TOTAL CELLS 1,500,800
/////MESH IJK=X,Y,Z, XB=-1.0,1003.0,-152.0,152.0,0.0,140.0 / Total Domain
+++++MESH 0.5m++++  CELLS 30,720
&MESH IJK=16,40,48, XB=27.0,35.0,-10.0,10.0,0.0,24.0, COLOR= RED, MPI_PROCESS=0 /
+++++MESH 1m++++    CELLS 262,400
&MESH IJK=8,30,52, XB=27.0,35.0,-40,-10.0,0.0,52.0, COLOR=YELLOW, MPI_PROCESS=0 /
&MESH IJK=28,80,52, XB=35.0,63.0,-40.0,40.0,0.0,52.0, COLOR=YELLOW, MPI_PROCESS=1 /
&MESH IJK=8,30,52, XB=27.0,35.0,10.0,40.0,0.0,52.0, COLOR=YELLOW, MPI_PROCESS=1 /
&MESH IJK=28,80,52, XB=-1.0,27.0,-40.0,40.0,0.0,52.0, COLOR=YELLOW, MPI_PROCESS=2 /
&MESH IJK=8,20,28, XB=27.0,35.0,-10.0,10.0,24.0,52.0, COLOR=YELLOW, MPI_PROCESS=2 /
+++++MESH 2m++++    CELLS 621,920
&MESH IJK=126,32,50, XB=-1.0,251.0,-104.0,-40.0,0.0,100.0, COLOR=GREEN, MPI_PROCESS=3 /
&MESH IJK=94,40,50, XB=63.0,251.0,-40.0,40.0,0.0,100.0, COLOR=GREEN, MPI_PROCESS=4 /
&MESH IJK=126,32,50, XB=-1.0,251.0,40.0,104.0,0.0,100.0, COLOR=GREEN, MPI_PROCESS=5 /
&MESH IJK=32,40,24, XB=-1.0,63.0,-40.0,40.0,52.0,100.0, COLOR=GREEN, MPI_PROCESS=6 /
+++++MESH 4m++++     CELLS 585,760
&MESH IJK=251,12,35, XB=-1.0,1003.0,-152.0,-104.0,0.0,140.0, COLOR=BLUE, MPI_PROCESS=7 /
&MESH IJK=188,8,35, XB=251.0,1003.0,-104.0,-72.0,0.0,140.0 , COLOR=BLUE, MPI_PROCESS=8 /
&MESH IJK=188,36,35, XB=251.0,1003.0,-72.0,72.0,0.0,140.0 , COLOR=BLUE, MPI_PROCESS=9 /
&MESH IJK=188,8,35, XB=251.0,1003.0,72.0,104.0,0.0,140.0 , COLOR=BLUE, MPI_PROCESS=10 /
&MESH IJK=251,12,35, XB=-1.0,1003.0,104.0,152.0,0.0,140.0, COLOR=BLUE, MPI_PROCESS=11  /
&MESH IJK=63,52,10, XB=-1.0,251.0,-104.0,104.0,100.0,140.0, COLOR=BLUE, MPI_PROCESS=12  /


++++++VENTS - WIND - ATM TEMP+++++
&VENT MB=ZMAX, SURF_ID='OPEN'/
&VENT PBX=-1.0, SURF_ID='OPEN', WIND=.TRUE./
&VENT PBX=1003.0, SURF_ID='OPEN', WIND=.TRUE./
&VENT PBY=-152.0, SURF_ID='OPEN', WIND=.TRUE./
&VENT PBY=152.0, SURF_ID='OPEN', WIND=.TRUE./


&WIND SPEED=6.7, Z_REF=10.0, DIRECTION=270.0, L=1000000.0, Z_0=0.000038, U_STAR=0.2147348  /

+++++++ FUEL REACTION ++++++++

&SPEC ID='CARBON DIOXIDE' /
&SPEC ID='CARBON MONOXIDE' /
&SPEC ID='OXYGEN'/
&SPEC ID='SOOT' /
&REAC  FUEL = 'CARBON MONOXIDE',
                    SOOT_YIELD = 0.03092783505,
                    CO_YIELD = 0.000,
                    C = 1,
                    H = 0,
                    O = 1,
                    HEAT_OF_COMBUSTION=10100./AUTO_IGNITION_TEMPERATURE=0.0
```

++++++++++++++++++BRAND PROPERTIES FOR ALL BRANDS ++++++++++++++++++++++++++++++++++

```
&PROP ID='particle',  SMOKEVIEW_ID='box', SMOKEVIEW_PARAMETERS(1:6)='R=192', 'G=255', 'B=128',
'DX=0.004', 'DY=0.004', 'DZ=0.002' /

&MATL ID = 'Vegetation',
      DENSITY = 100.0,
      CONDUCTIVITY = 0.24,
      SPECIFIC_HEAT = 1.466,
      EMISSIVITY=0.9,
      N_S(1) = 1.0,
      A(1) = 725.0,
      E(1) = 57361.48,
      MATL_ID(1,1) = 'CHAR',
      NU_MATL(1,1) = 0.39,
      SPEC_ID(1:2,1) = 'CARBON MONOXIDE', 'CARBON DIOXIDE'
      NU_SPEC(1:2,1) = 0.488,0.122,
      HEAT_OF_REACTION = 418.0 /


&MATL ID = 'CHAR',
      DENSITY = 39.0,
      CONDUCTIVITY = 0.1,
      EMISSIVITY=0.9,
      SPECIFIC_HEAT = 1.1 /



++++++++++++++++++   BRANDS  PROPERTIES 0.2 cm THICKNESS       +++++++++++++++++
&PART  ID='brand_part-1', INITIAL_TEMPERATURE=1044.0, SURF_ID='brand-1', PROP_ID='particle',
COLOR='RED', QUANTITIES='PARTICLE TEMPERATURE','PARTICLE MASS'/

&PART  ID='brand_part-2', INITIAL_TEMPERATURE=1044.0, SURF_ID='brand-1', PROP_ID='particle',
COLOR='RED', QUANTITIES='PARTICLE TEMPERATURE','PARTICLE MASS'/

&PART  ID='brand_part-3', INITIAL_TEMPERATURE=1044.0, SURF_ID='brand-1', PROP_ID='particle',
COLOR='RED', QUANTITIES='PARTICLE TEMPERATURE','PARTICLE MASS'/

&PART  ID='brand_part-4', INITIAL_TEMPERATURE=1044.0, SURF_ID='brand-1', PROP_ID='particle',
COLOR='RED', QUANTITIES='PARTICLE TEMPERATURE','PARTICLE MASS'/

&PART  ID='brand_part-5', INITIAL_TEMPERATURE=1044.0, SURF_ID='brand-1', PROP_ID='particle',
COLOR='RED', QUANTITIES='PARTICLE TEMPERATURE','PARTICLE MASS'/

&PART  ID='brand_part-6', INITIAL_TEMPERATURE=1044.0, SURF_ID='brand-1', PROP_ID='particle',
COLOR='RED', QUANTITIES='PARTICLE TEMPERATURE','PARTICLE MASS'/

&PART  ID='brand_part-7', INITIAL_TEMPERATURE=1044.0, SURF_ID='brand-1', PROP_ID='particle',
COLOR='RED', QUANTITIES='PARTICLE TEMPERATURE','PARTICLE MASS'/

&PART  ID='brand_part-8', INITIAL_TEMPERATURE=1044.0, SURF_ID='brand-1', PROP_ID='particle',
COLOR='RED', QUANTITIES='PARTICLE TEMPERATURE','PARTICLE MASS'/

&PART  ID='brand_part-9', INITIAL_TEMPERATURE=1044.0, SURF_ID='brand-1', PROP_ID='particle',
COLOR='RED', QUANTITIES='PARTICLE TEMPERATURE','PARTICLE MASS'/

&PART  ID='brand_part-10', INITIAL_TEMPERATURE=1044.0, SURF_ID='brand-1', PROP_ID='particle',
COLOR='RED', QUANTITIES='PARTICLE TEMPERATURE','PARTICLE MASS'/

&SURF ID='brand-1',
      MATL_ID='Vegetation',
      COLOR     = 'RED',
      BACKING   = 'INSULATED' ,
      THICKNESS=0.001,
      LENGTH=0.0886227,
      WIDTH=0.0886227,
      GEOMETRY='CARTESIAN' /
```

++++++++++++++++++ BRANDS PROPERTIES 0.3 cm THICKNESS ++++++++++++++++++++++

&PART ID='brand_part-11', INITIAL_TEMPERATURE=1044.0, SURF_ID='brand-2', PROP_ID='particle',
COLOR='YELLOW', QUANTITIES='PARTICLE TEMPERATURE','PARTICLE MASS'/

&PART ID='brand_part-12', INITIAL_TEMPERATURE=1044.0, SURF_ID='brand-2', PROP_ID='particle',
COLOR='YELLOW', QUANTITIES='PARTICLE TEMPERATURE','PARTICLE MASS'/

&PART ID='brand_part-13', INITIAL_TEMPERATURE=1044.0, SURF_ID='brand-2', PROP_ID='particle',
COLOR='YELLOW', QUANTITIES='PARTICLE TEMPERATURE','PARTICLE MASS'/

&PART ID='brand_part-14', INITIAL_TEMPERATURE=1044.0, SURF_ID='brand-2', PROP_ID='particle',
COLOR='YELLOW', QUANTITIES='PARTICLE TEMPERATURE','PARTICLE MASS'/

&PART ID='brand_part-15', INITIAL_TEMPERATURE=1044.0, SURF_ID='brand-2', PROP_ID='particle',
COLOR='YELLOW', QUANTITIES='PARTICLE TEMPERATURE','PARTICLE MASS'/

&PART ID='brand_part-16', INITIAL_TEMPERATURE=1044.0, SURF_ID='brand-2', PROP_ID='particle',
COLOR='YELLOW', QUANTITIES='PARTICLE TEMPERATURE','PARTICLE MASS'/

&PART ID='brand_part-17', INITIAL_TEMPERATURE=1044.0, SURF_ID='brand-2', PROP_ID='particle',
COLOR='YELLOW', QUANTITIES='PARTICLE TEMPERATURE','PARTICLE MASS'/

&PART ID='brand_part-18', INITIAL_TEMPERATURE=1044.0, SURF_ID='brand-2', PROP_ID='particle',
COLOR='YELLOW', QUANTITIES='PARTICLE TEMPERATURE','PARTICLE MASS'/

&PART ID='brand_part-19', INITIAL_TEMPERATURE=1044.0, SURF_ID='brand-2', PROP_ID='particle',
COLOR='YELLOW', QUANTITIES='PARTICLE TEMPERATURE','PARTICLE MASS'/

&PART ID='brand_part-20', INITIAL_TEMPERATURE=1044.0, SURF_ID='brand-2', PROP_ID='particle',
COLOR='YELLOW', QUANTITIES='PARTICLE TEMPERATURE','PARTICLE MASS'/

&SURF ID='brand-2',
	MATL_ID='Vegetation',
	COLOR = 'YELLOW',
	BACKING = 'INSULATED' ,
	THICKNESS=0.0015,
	LENGTH=0.0886227,
	WIDTH=0.0886227,
	GEOMETRY='CARTESIAN' /

++++++++++++++++++ BRANDS PROPERTIES 0.5 cm THICKNESS ++++++++++++++++++++++++

&PART ID='brand_part-21', INITIAL_TEMPERATURE=1044.0, SURF_ID='brand-3', PROP_ID='particle',
COLOR='GREEN', QUANTITIES='PARTICLE TEMPERATURE','PARTICLE MASS'/

&PART ID='brand_part-22', INITIAL_TEMPERATURE=1044.0, SURF_ID='brand-3', PROP_ID='particle',
COLOR='GREEN', QUANTITIES='PARTICLE TEMPERATURE','PARTICLE MASS'/

&PART ID='brand_part-23', INITIAL_TEMPERATURE=1044.0, SURF_ID='brand-3', PROP_ID='particle',
COLOR='GREEN', QUANTITIES='PARTICLE TEMPERATURE','PARTICLE MASS'/

&PART ID='brand_part-24', INITIAL_TEMPERATURE=1044.0, SURF_ID='brand-3', PROP_ID='particle',
COLOR='GREEN', QUANTITIES='PARTICLE TEMPERATURE','PARTICLE MASS'/

&PART ID='brand_part-25', INITIAL_TEMPERATURE=1044.0, SURF_ID='brand-3', PROP_ID='particle',
COLOR='GREEN', QUANTITIES='PARTICLE TEMPERATURE','PARTICLE MASS'/

&PART ID='brand_part-26', INITIAL_TEMPERATURE=1044.0, SURF_ID='brand-3', PROP_ID='particle',
COLOR='GREEN', QUANTITIES='PARTICLE TEMPERATURE','PARTICLE MASS'/

&PART ID='brand_part-27', INITIAL_TEMPERATURE=1044.0, SURF_ID='brand-3', PROP_ID='particle',
COLOR='GREEN', QUANTITIES='PARTICLE TEMPERATURE','PARTICLE MASS'/

&PART ID='brand_part-28', INITIAL_TEMPERATURE=1044.0, SURF_ID='brand-3', PROP_ID='particle',
COLOR='GREEN', QUANTITIES='PARTICLE TEMPERATURE','PARTICLE MASS'/

```
&PART  ID='brand_part-29', INITIAL_TEMPERATURE=1044.0, SURF_ID='brand-3', PROP_ID='particle',
COLOR='GREEN', QUANTITIES='PARTICLE TEMPERATURE','PARTICLE MASS'/

&PART  ID='brand_part-30', INITIAL_TEMPERATURE=1044.0, SURF_ID='brand-3', PROP_ID='particle',
COLOR='GREEN', QUANTITIES='PARTICLE TEMPERATURE','PARTICLE MASS'/

&SURF ID='brand-3',
            MATL_ID='Vegetation',
            COLOR     = 'GREEN',
            BACKING   = 'INSULATED' ,
            THICKNESS=0.0025,
            LENGTH=0.0886227,
            WIDTH=0.0886227,
            GEOMETRY='CARTESIAN' /


++++++++++++++++++   BRANDS  PROPERTIES 1.0 cm THICKNESS++++++++++++++++++++

&PART  ID='brand_part-31', INITIAL_TEMPERATURE=1044.0, SURF_ID='brand-4', PROP_ID='particle',
COLOR='BLUE', QUANTITIES='PARTICLE TEMPERATURE','PARTICLE MASS'/

&PART  ID='brand_part-32', INITIAL_TEMPERATURE=1044.0, SURF_ID='brand-4', PROP_ID='particle',
COLOR='BLUE', QUANTITIES='PARTICLE TEMPERATURE','PARTICLE MASS'/

&PART  ID='brand_part-33', INITIAL_TEMPERATURE=1044.0, SURF_ID='brand-4', PROP_ID='particle',
COLOR='BLUE', QUANTITIES='PARTICLE TEMPERATURE','PARTICLE MASS'/

&PART  ID='brand_part-34', INITIAL_TEMPERATURE=1044.0, SURF_ID='brand-4', PROP_ID='particle',
COLOR='BLUE', QUANTITIES='PARTICLE TEMPERATURE','PARTICLE MASS'/

&PART  ID='brand_part-35', INITIAL_TEMPERATURE=1044.0, SURF_ID='brand-4', PROP_ID='particle',
COLOR='BLUE', QUANTITIES='PARTICLE TEMPERATURE','PARTICLE MASS'/

&PART  ID='brand_part-36', INITIAL_TEMPERATURE=1044.0, SURF_ID='brand-4', PROP_ID='particle',
COLOR='BLUE', QUANTITIES='PARTICLE TEMPERATURE','PARTICLE MASS'/

&PART  ID='brand_part-37', INITIAL_TEMPERATURE=1044.0, SURF_ID='brand-4', PROP_ID='particle',
COLOR='BLUE', QUANTITIES='PARTICLE TEMPERATURE','PARTICLE MASS'/

&PART  ID='brand_part-38', INITIAL_TEMPERATURE=1044.0, SURF_ID='brand-4', PROP_ID='particle',
COLOR='BLUE', QUANTITIES='PARTICLE TEMPERATURE','PARTICLE MASS'/

&PART  ID='brand_part-39', INITIAL_TEMPERATURE=1044.0, SURF_ID='brand-4', PROP_ID='particle',
COLOR='BLUE', QUANTITIES='PARTICLE TEMPERATURE','PARTICLE MASS'/

&PART  ID='brand_part-40', INITIAL_TEMPERATURE=1044.0, SURF_ID='brand-4', PROP_ID='particle',
COLOR='BLUE', QUANTITIES='PARTICLE TEMPERATURE','PARTICLE MASS'/

&SURF ID='brand-4',
            MATL_ID='Vegetation',
            COLOR     = 'BLUE',
            BACKING   = 'INSULATED' ,
            THICKNESS=0.005,
            LENGTH=0.0886227,
            WIDTH=0.0886227,
            GEOMETRY='CARTESIAN' /


++++++++++++++++++   BRANDS  PROPERTIES 2.0 cm THICKNESS      ++++++++++++++++++++

&PART  ID='brand_part-41', INITIAL_TEMPERATURE=1044.0, SURF_ID='brand-5', PROP_ID='particle',
COLOR='MAGENTA', QUANTITIES='PARTICLE TEMPERATURE','PARTICLE MASS'/

&PART  ID='brand_part-42', INITIAL_TEMPERATURE=1044.0, SURF_ID='brand-5', PROP_ID='particle',
COLOR='MAGENTA', QUANTITIES='PARTICLE TEMPERATURE','PARTICLE MASS'/

&PART  ID='brand_part-43', INITIAL_TEMPERATURE=1044.0, SURF_ID='brand-5', PROP_ID='particle',
COLOR='MAGENTA', QUANTITIES='PARTICLE TEMPERATURE','PARTICLE MASS'/
```

```
&PART  ID='brand_part-44', INITIAL_TEMPERATURE=1044.0, SURF_ID='brand-5', PROP_ID='particle',
COLOR='MAGENTA', QUANTITIES='PARTICLE TEMPERATURE','PARTICLE MASS'/

&PART  ID='brand_part-45', INITIAL_TEMPERATURE=1044.0, SURF_ID='brand-5', PROP_ID='particle',
COLOR='MAGENTA', QUANTITIES='PARTICLE TEMPERATURE','PARTICLE MASS'/

&PART  ID='brand_part-46', INITIAL_TEMPERATURE=1044.0, SURF_ID='brand-5', PROP_ID='particle',
COLOR='MAGENTA', QUANTITIES='PARTICLE TEMPERATURE','PARTICLE MASS'/

&PART  ID='brand_part-47', INITIAL_TEMPERATURE=1044.0, SURF_ID='brand-5', PROP_ID='particle',
COLOR='MAGENTA', QUANTITIES='PARTICLE TEMPERATURE','PARTICLE MASS'/

&PART  ID='brand_part-48', INITIAL_TEMPERATURE=1044.0, SURF_ID='brand-5', PROP_ID='particle',
COLOR='MAGENTA', QUANTITIES='PARTICLE TEMPERATURE','PARTICLE MASS'/

&PART  ID='brand_part-49', INITIAL_TEMPERATURE=1044.0, SURF_ID='brand-5', PROP_ID='particle',
COLOR='MAGENTA', QUANTITIES='PARTICLE TEMPERATURE','PARTICLE MASS'/

&PART  ID='brand_part-50', INITIAL_TEMPERATURE=1044.0, SURF_ID='brand-5', PROP_ID='particle',
COLOR='MAGENTA', QUANTITIES='PARTICLE TEMPERATURE','PARTICLE MASS'/

&SURF ID='brand-5',
        MATL_ID='Vegetation',
        COLOR     = 'MAGENTA',
        BACKING   = 'INSULATED' ,
        THICKNESS=0.01,
        LENGTH=0.0886227,
        WIDTH=0.0886227,
        GEOMETRY='CARTESIAN' /
++++++++++++++++++++   BRANDS  PROPERTIES 4.0 cm THICKNESS      ++++++++++++++++++++

&PART  ID='brand_part-51', INITIAL_TEMPERATURE=1044.0, SURF_ID='brand-6', PROP_ID='particle',
COLOR='BLACK', QUANTITIES='PARTICLE TEMPERATURE','PARTICLE MASS'/

&PART  ID='brand_part-52', INITIAL_TEMPERATURE=1044.0, SURF_ID='brand-6', PROP_ID='particle',
COLOR='BLACK', QUANTITIES='PARTICLE TEMPERATURE','PARTICLE MASS'/

&PART  ID='brand_part-53', INITIAL_TEMPERATURE=1044.0, SURF_ID='brand-6', PROP_ID='particle',
COLOR='BLACK', QUANTITIES='PARTICLE TEMPERATURE','PARTICLE MASS'/

&PART  ID='brand_part-54', INITIAL_TEMPERATURE=1044.0, SURF_ID='brand-6', PROP_ID='particle',
COLOR='BLACK', QUANTITIES='PARTICLE TEMPERATURE','PARTICLE MASS'/

&PART  ID='brand_part-55', INITIAL_TEMPERATURE=1044.0, SURF_ID='brand-6', PROP_ID='particle',
COLOR='BLACK', QUANTITIES='PARTICLE TEMPERATURE','PARTICLE MASS'/

&PART  ID='brand_part-56', INITIAL_TEMPERATURE=1044.0, SURF_ID='brand-6', PROP_ID='particle',
COLOR='BLACK', QUANTITIES='PARTICLE TEMPERATURE','PARTICLE MASS'/

&PART  ID='brand_part-57', INITIAL_TEMPERATURE=1044.0, SURF_ID='brand-6', PROP_ID='particle',
COLOR='BLACK', QUANTITIES='PARTICLE TEMPERATURE','PARTICLE MASS'/

&PART  ID='brand_part-58', INITIAL_TEMPERATURE=1044.0, SURF_ID='brand-6', PROP_ID='particle',
COLOR='BLACK', QUANTITIES='PARTICLE TEMPERATURE','PARTICLE MASS'/

&PART  ID='brand_part-59', INITIAL_TEMPERATURE=1044.0, SURF_ID='brand-6', PROP_ID='particle',
COLOR='BLACK', QUANTITIES='PARTICLE TEMPERATURE','PARTICLE MASS'/

&PART  ID='brand_part-60', INITIAL_TEMPERATURE=1044.0, SURF_ID='brand-6', PROP_ID='particle',
COLOR='BLACK', QUANTITIES='PARTICLE TEMPERATURE','PARTICLE MASS'/

&SURF ID='brand-6',
        MATL_ID='Vegetation',
        COLOR     = 'BLACK',
        BACKING   = 'INSULATED' ,
        THICKNESS=0.02,
        LENGTH=0.0886227,
        WIDTH=0.0886227,
        GEOMETRY='CARTESIAN' /
```

++++++++++++++++++ BRANDS PROPERTIES 8.86 cm THICKNESS ++++++++++++++++++++

&PART ID='brand_part-61', INITIAL_TEMPERATURE=1044.0, SURF_ID='brand-7', PROP_ID='particle', COLOR='MINT', QUANTITIES='PARTICLE TEMPERATURE','PARTICLE MASS'/

&PART ID='brand_part-62', INITIAL_TEMPERATURE=1044.0, SURF_ID='brand-7', PROP_ID='particle', COLOR='MINT', QUANTITIES='PARTICLE TEMPERATURE','PARTICLE MASS'/

&PART ID='brand_part-63', INITIAL_TEMPERATURE=1044.0, SURF_ID='brand-7', PROP_ID='particle', COLOR='MINT', QUANTITIES='PARTICLE TEMPERATURE','PARTICLE MASS'/

&PART ID='brand_part-64', INITIAL_TEMPERATURE=1044.0, SURF_ID='brand-7', PROP_ID='particle', COLOR='MINT', QUANTITIES='PARTICLE TEMPERATURE','PARTICLE MASS'/

&PART ID='brand_part-65', INITIAL_TEMPERATURE=1044.0, SURF_ID='brand-7', PROP_ID='particle', COLOR='MINT', QUANTITIES='PARTICLE TEMPERATURE','PARTICLE MASS'/

&PART ID='brand_part-66', INITIAL_TEMPERATURE=1044.0, SURF_ID='brand-7', PROP_ID='particle', COLOR='MINT', QUANTITIES='PARTICLE TEMPERATURE','PARTICLE MASS'/

&PART ID='brand_part-67', INITIAL_TEMPERATURE=1044.0, SURF_ID='brand-7', PROP_ID='particle', COLOR='MINT', QUANTITIES='PARTICLE TEMPERATURE','PARTICLE MASS'/

&PART ID='brand_part-68', INITIAL_TEMPERATURE=1044.0, SURF_ID='brand-7', PROP_ID='particle', COLOR='MINT', QUANTITIES='PARTICLE TEMPERATURE','PARTICLE MASS'/

&PART ID='brand_part-69', INITIAL_TEMPERATURE=1044.0, SURF_ID='brand-7', PROP_ID='particle', COLOR='MINT', QUANTITIES='PARTICLE TEMPERATURE','PARTICLE MASS'/

&PART ID='brand_part-70', INITIAL_TEMPERATURE=1044.0, SURF_ID='brand-7', PROP_ID='particle', COLOR='MINT', QUANTITIES='PARTICLE TEMPERATURE','PARTICLE MASS'/

&SURF ID='brand-7',
MATL_ID='Vegetation',
COLOR = 'MINT',
BACKING = 'INSULATED' ,
THICKNESS=0.0443,
LENGTH=0.0886227,
WIDTH=0.0886227,
GEOMETRY='CARTESIAN' /

********** RELEASE &INIT **********

&INIT ID='FIREBRAND-1', PART_ID='brand_part-1', XYZ=34.999, 2.5, 7.999, N_PARTICLES=1, UVW=0.697, -0.666, 0.174, DEVC_ID='PART-TIME-1'/

&INIT ID='FIREBRAND-2', PART_ID='brand_part-2', XYZ=34.999, 2.5, 7.999, N_PARTICLES=1, UVW=0.697, -0.666, 0.174, DEVC_ID='PART-TIME-2'/

&INIT ID='FIREBRAND-3', PART_ID='brand_part-3', XYZ=34.999, 2.5, 7.999, N_PARTICLES=1, UVW=0.697, -0.666, 0.174, DEVC_ID='PART-TIME-3'/

&INIT ID='FIREBRAND-4', PART_ID='brand_part-4', XYZ=34.999, 2.5, 7.999, N_PARTICLES=1, UVW=0.697, -0.666, 0.174, DEVC_ID='PART-TIME-4'/

&INIT ID='FIREBRAND-5', PART_ID='brand_part-5', XYZ=34.999, 2.5, 7.999, N_PARTICLES=1, UVW=0.697, -0.666, 0.174, DEVC_ID='PART-TIME-5'/

&INIT ID='FIREBRAND-6', PART_ID='brand_part-6', XYZ=34.999, 2.5, 7.999, N_PARTICLES=1, UVW=0.697, -0.666, 0.174, DEVC_ID='PART-TIME-6'/

&INIT ID='FIREBRAND-7', PART_ID='brand_part-7', XYZ=34.999, 2.5, 7.999, N_PARTICLES=1, UVW=0.697, -0.666, 0.174, DEVC_ID='PART-TIME-7'/

&INIT ID='FIREBRAND-8', PART_ID='brand_part-8', XYZ=34.999, 2.5, 7.999, N_PARTICLES=1, UVW=0.697, -0.666, 0.174, DEVC_ID='PART-TIME-8'/

&INIT ID='FIREBRAND-9', PART_ID='brand_part-9', XYZ=34.999, 2.5, 7.999, N_PARTICLES=1, UVW=0.697, -0.666, 0.174, DEVC_ID='PART-TIME-9'/

&INIT ID='FIREBRAND-10', PART_ID='brand_part-10', XYZ=34.999, 2.5, 7.999, N_PARTICLES=1, UVW=0.697, -0.666, 0.174, DEVC_ID='PART-TIME-10'/

&INIT ID='FIREBRAND-11', PART_ID='brand_part-11', XYZ=34.999, 2.5, 7.999, N_PARTICLES=1, UVW=0.697, -0.666, 0.174, DEVC_ID='PART-TIME-11'/

&INIT ID='FIREBRAND-12', PART_ID='brand_part-12', XYZ=34.999, 2.5, 7.999, N_PARTICLES=1, UVW=0.697, -0.666, 0.174, DEVC_ID='PART-TIME-12'/

&INIT ID='FIREBRAND-13', PART_ID='brand_part-13', XYZ=34.999, 2.5, 7.999, N_PARTICLES=1, UVW=0.697, -0.666, 0.174, DEVC_ID='PART-TIME-13'/

&INIT ID='FIREBRAND-14', PART_ID='brand_part-14', XYZ=34.999, 2.5, 7.999, N_PARTICLES=1, UVW=0.697, -0.666, 0.174, DEVC_ID='PART-TIME-14'/

&INIT ID='FIREBRAND-15', PART_ID='brand_part-15', XYZ=34.999, 2.5, 7.999, N_PARTICLES=1, UVW=0.697, -0.666, 0.174, DEVC_ID='PART-TIME-15'/

&INIT ID='FIREBRAND-16', PART_ID='brand_part-16', XYZ=34.999, 2.5, 7.999, N_PARTICLES=1, UVW=0.697, -0.666, 0.174, DEVC_ID='PART-TIME-16'/

&INIT ID='FIREBRAND-17', PART_ID='brand_part-17', XYZ=34.999, 2.5, 7.999, N_PARTICLES=1, UVW=0.697, -0.666, 0.174, DEVC_ID='PART-TIME-17'/

&INIT ID='FIREBRAND-18', PART_ID='brand_part-18', XYZ=34.999, 2.5, 7.999, N_PARTICLES=1, UVW=0.697, -0.666, 0.174, DEVC_ID='PART-TIME-18'/

&INIT ID='FIREBRAND-19', PART_ID='brand_part-19', XYZ=34.999, 2.5, 7.999, N_PARTICLES=1, UVW=0.697, -0.666, 0.174, DEVC_ID='PART-TIME-19'/

&INIT ID='FIREBRAND-20', PART_ID='brand_part-20', XYZ=34.999, 2.5, 7.999, N_PARTICLES=1, UVW=0.697, -0.666, 0.174, DEVC_ID='PART-TIME-20'/

&INIT ID='FIREBRAND-21', PART_ID='brand_part-21', XYZ=34.999, 2.5, 7.999, N_PARTICLES=1, UVW=0.697, -0.666, 0.174, DEVC_ID='PART-TIME-21'/

&INIT ID='FIREBRAND-22', PART_ID='brand_part-22', XYZ=34.999, 2.5, 7.999, N_PARTICLES=1, UVW=0.697, -0.666, 0.174, DEVC_ID='PART-TIME-22'/

&INIT ID='FIREBRAND-23', PART_ID='brand_part-23', XYZ=34.999, 2.5, 7.999, N_PARTICLES=1, UVW=0.697, -0.666, 0.174, DEVC_ID='PART-TIME-23'/

&INIT ID='FIREBRAND-24', PART_ID='brand_part-24', XYZ=34.999, 2.5, 7.999, N_PARTICLES=1, UVW=0.697, -0.666, 0.174, DEVC_ID='PART-TIME-24'/

&INIT ID='FIREBRAND-25', PART_ID='brand_part-25', XYZ=34.999, 2.5, 7.999, N_PARTICLES=1, UVW=0.697, -0.666, 0.174, DEVC_ID='PART-TIME-25'/

&INIT ID='FIREBRAND-26', PART_ID='brand_part-26', XYZ=34.999, 2.5, 7.999, N_PARTICLES=1, UVW=0.697, -0.666, 0.174, DEVC_ID='PART-TIME-26'/

&INIT ID='FIREBRAND-27', PART_ID='brand_part-27', XYZ=34.999, 2.5, 7.999, N_PARTICLES=1, UVW=0.697, -0.666, 0.174, DEVC_ID='PART-TIME-27'/

&INIT ID='FIREBRAND-28', PART_ID='brand_part-28', XYZ=34.999, 2.5, 7.999, N_PARTICLES=1, UVW=0.697, -0.666, 0.174, DEVC_ID='PART-TIME-28'/

&INIT ID='FIREBRAND-29', PART_ID='brand_part-29', XYZ=34.999, 2.5, 7.999, N_PARTICLES=1, UVW=0.697, -0.666, 0.174, DEVC_ID='PART-TIME-29'/

&INIT ID='FIREBRAND-30', PART_ID='brand_part-30', XYZ=34.999, 2.5, 7.999, N_PARTICLES=1, UVW=0.697, -0.666, 0.174, DEVC_ID='PART-TIME-30'/

&INIT ID='FIREBRAND-31', PART_ID='brand_part-31', XYZ=34.999, 2.5, 7.999, N_PARTICLES=1, UVW=0.697, -0.666, 0.174, DEVC_ID='PART-TIME-31'/

&INIT ID='FIREBRAND-32', PART_ID='brand_part-32', XYZ=34.999, 2.5, 7.999, N_PARTICLES=1, UVW=0.697, -0.666, 0.174, DEVC_ID='PART-TIME-32'/

&INIT ID='FIREBRAND-33', PART_ID='brand_part-33', XYZ=34.999, 2.5, 7.999, N_PARTICLES=1, UVW=0.697, -0.666, 0.174, DEVC_ID='PART-TIME-33'/

&INIT ID='FIREBRAND-34', PART_ID='brand_part-34', XYZ=34.999, 2.5, 7.999, N_PARTICLES=1, UVW=0.697, -0.666, 0.174, DEVC_ID='PART-TIME-34'/

&INIT ID='FIREBRAND-35', PART_ID='brand_part-35', XYZ=34.999, 2.5, 7.999, N_PARTICLES=1, UVW=0.697, -0.666, 0.174, DEVC_ID='PART-TIME-35'/

&INIT ID='FIREBRAND-36', PART_ID='brand_part-36', XYZ=34.999, 2.5, 7.999, N_PARTICLES=1, UVW=0.697, -0.666, 0.174, DEVC_ID='PART-TIME-36'/

&INIT ID='FIREBRAND-37', PART_ID='brand_part-37', XYZ=34.999, 2.5, 7.999, N_PARTICLES=1, UVW=0.697, -0.666, 0.174, DEVC_ID='PART-TIME-37'/

&INIT ID='FIREBRAND-38', PART_ID='brand_part-38', XYZ=34.999, 2.5, 7.999, N_PARTICLES=1, UVW=0.697, -0.666, 0.174, DEVC_ID='PART-TIME-38'/

&INIT ID='FIREBRAND-39', PART_ID='brand_part-39', XYZ=34.999, 2.5, 7.999, N_PARTICLES=1, UVW=0.697, -0.666, 0.174, DEVC_ID='PART-TIME-39'/

&INIT ID='FIREBRAND-40', PART_ID='brand_part-40', XYZ=34.999, 2.5, 7.999, N_PARTICLES=1, UVW=0.697, -0.666, 0.174, DEVC_ID='PART-TIME-40'/

&INIT ID='FIREBRAND-41', PART_ID='brand_part-41', XYZ=34.999, 2.5, 7.999, N_PARTICLES=1, UVW=0.697, -0.666, 0.174, DEVC_ID='PART-TIME-41'/

&INIT ID='FIREBRAND-42', PART_ID='brand_part-42', XYZ=34.999, 2.5, 7.999, N_PARTICLES=1, UVW=0.697, -0.666, 0.174, DEVC_ID='PART-TIME-42'/

&INIT ID='FIREBRAND-43', PART_ID='brand_part-43', XYZ=34.999, 2.5, 7.999, N_PARTICLES=1, UVW=0.697, -0.666, 0.174, DEVC_ID='PART-TIME-43'/

&INIT ID='FIREBRAND-44', PART_ID='brand_part-44', XYZ=34.999, 2.5, 7.999, N_PARTICLES=1, UVW=0.697, -0.666, 0.174, DEVC_ID='PART-TIME-44'/

&INIT ID='FIREBRAND-45', PART_ID='brand_part-45', XYZ=34.999, 2.5, 7.999, N_PARTICLES=1, UVW=0.697, -0.666, 0.174, DEVC_ID='PART-TIME-45'/

&INIT ID='FIREBRAND-46', PART_ID='brand_part-46', XYZ=34.999, 2.5, 7.999, N_PARTICLES=1, UVW=0.697, -0.666, 0.174, DEVC_ID='PART-TIME-46'/

&INIT ID='FIREBRAND-47', PART_ID='brand_part-47', XYZ=34.999, 2.5, 7.999, N_PARTICLES=1, UVW=0.697, -0.666, 0.174, DEVC_ID='PART-TIME-47'/

&INIT ID='FIREBRAND-48', PART_ID='brand_part-48', XYZ=34.999, 2.5, 7.999, N_PARTICLES=1, UVW=0.697, -0.666, 0.174, DEVC_ID='PART-TIME-48'/

&INIT ID='FIREBRAND-49', PART_ID='brand_part-49', XYZ=34.999, 2.5, 7.999, N_PARTICLES=1, UVW=0.697, -0.666, 0.174, DEVC_ID='PART-TIME-49'/

&INIT ID='FIREBRAND-50', PART_ID='brand_part-50', XYZ=34.999, 2.5, 7.999, N_PARTICLES=1, UVW=0.697, -0.666, 0.174, DEVC_ID='PART-TIME-50'/

&INIT ID='FIREBRAND-51', PART_ID='brand_part-51', XYZ=34.999, 2.5, 7.999, N_PARTICLES=1, UVW=0.697, -0.666, 0.174, DEVC_ID='PART-TIME-51'/

&INIT ID='FIREBRAND-52', PART_ID='brand_part-52', XYZ=34.999, 2.5, 7.999, N_PARTICLES=1, UVW=0.697, -0.666, 0.174, DEVC_ID='PART-TIME-52'/

&INIT ID='FIREBRAND-53', PART_ID='brand_part-53', XYZ=34.999, 2.5, 7.999, N_PARTICLES=1, UVW=0.697, -0.666, 0.174, DEVC_ID='PART-TIME-53'/

&INIT ID='FIREBRAND-54', PART_ID='brand_part-54', XYZ=34.999, 2.5, 7.999, N_PARTICLES=1, UVW=0.697, -0.666, 0.174, DEVC_ID='PART-TIME-54'/

&INIT ID='FIREBRAND-55', PART_ID='brand_part-55', XYZ=34.999, 2.5, 7.999, N_PARTICLES=1, UVW=0.697, -0.666, 0.174, DEVC_ID='PART-TIME-55'/

&INIT ID='FIREBRAND-56', PART_ID='brand_part-56', XYZ=34.999, 2.5, 7.999, N_PARTICLES=1, UVW=0.697, -0.666, 0.174, DEVC_ID='PART-TIME-56'/

&INIT ID='FIREBRAND-57', PART_ID='brand_part-57', XYZ=34.999, 2.5, 7.999, N_PARTICLES=1, UVW=0.697, -0.666, 0.174, DEVC_ID='PART-TIME-57'/

&INIT ID='FIREBRAND-58', PART_ID='brand_part-58', XYZ=34.999, 2.5, 7.999, N_PARTICLES=1, UVW=0.697, -0.666, 0.174, DEVC_ID='PART-TIME-58'/

&INIT ID='FIREBRAND-59', PART_ID='brand_part-59', XYZ=34.999, 2.5, 7.999, N_PARTICLES=1, UVW=0.697, -0.666, 0.174, DEVC_ID='PART-TIME-59'/

&INIT ID='FIREBRAND-60', PART_ID='brand_part-60', XYZ=34.999, 2.5, 7.999, N_PARTICLES=1, UVW=0.697, -0.666, 0.174, DEVC_ID='PART-TIME-60'/

&INIT ID='FIREBRAND-61', PART_ID='brand_part-61', XYZ=34.999, 2.5, 7.999, N_PARTICLES=1, UVW=0.697, -0.666, 0.174, DEVC_ID='PART-TIME-61'/

&INIT ID='FIREBRAND-62', PART_ID='brand_part-62', XYZ=34.999, 2.5, 7.999, N_PARTICLES=1, UVW=0.697, -0.666, 0.174, DEVC_ID='PART-TIME-62'/

&INIT ID='FIREBRAND-63', PART_ID='brand_part-63', XYZ=34.999, 2.5, 7.999, N_PARTICLES=1, UVW=0.697, -0.666, 0.174, DEVC_ID='PART-TIME-63'/

&INIT ID='FIREBRAND-64', PART_ID='brand_part-64', XYZ=34.999, 2.5, 7.999, N_PARTICLES=1, UVW=0.697, -0.666, 0.174, DEVC_ID='PART-TIME-64'/

&INIT ID='FIREBRAND-65', PART_ID='brand_part-65', XYZ=34.999, 2.5, 7.999, N_PARTICLES=1, UVW=0.697, -0.666, 0.174, DEVC_ID='PART-TIME-65'/

&INIT ID='FIREBRAND-66', PART_ID='brand_part-66', XYZ=34.999, 2.5, 7.999, N_PARTICLES=1, UVW=0.697, -0.666, 0.174, DEVC_ID='PART-TIME-66'/

&INIT ID='FIREBRAND-67', PART_ID='brand_part-67', XYZ=34.999, 2.5, 7.999, N_PARTICLES=1, UVW=0.697, -0.666, 0.174, DEVC_ID='PART-TIME-67'/

&INIT ID='FIREBRAND-68', PART_ID='brand_part-68', XYZ=34.999, 2.5, 7.999, N_PARTICLES=1, UVW=0.697, -0.666, 0.174, DEVC_ID='PART-TIME-68'/

&INIT ID='FIREBRAND-69', PART_ID='brand_part-69', XYZ=34.999, 2.5, 7.999, N_PARTICLES=1, UVW=0.697, -0.666, 0.174, DEVC_ID='PART-TIME-69'/

&INIT ID='FIREBRAND-70', PART_ID='brand_part-70', XYZ=34.999, 2.5, 7.999, N_PARTICLES=1, UVW=0.697, -0.666, 0.174, DEVC_ID='PART-TIME-70'/

********** RELEASE &DEVC Time control **********

&DEVC ID='PART-TIME-1', XYZ=1.0, 0.0, 5.0, QUANTITY='TIME', SETPOINT=60, INITIAL_STATE=.FALSE./

&DEVC ID='PART-TIME-2', XYZ=1.0, 0.0, 5.0, QUANTITY='TIME', SETPOINT=61, INITIAL_STATE=.FALSE./

&DEVC ID='PART-TIME-3', XYZ=1.0, 0.0, 5.0, QUANTITY='TIME', SETPOINT=62, INITIAL_STATE=.FALSE./

&DEVC ID='PART-TIME-4', XYZ=1.0, 0.0, 5.0, QUANTITY='TIME', SETPOINT=63, INITIAL_STATE=.FALSE./

&DEVC ID='PART-TIME-5', XYZ=1.0, 0.0, 5.0, QUANTITY='TIME', SETPOINT=64, INITIAL_STATE=.FALSE./

&DEVC ID='PART-TIME-6', XYZ=1.0, 0.0, 5.0, QUANTITY='TIME', SETPOINT=65, INITIAL_STATE=.FALSE./

&DEVC ID='PART-TIME-7', XYZ=1.0, 0.0, 5.0, QUANTITY='TIME', SETPOINT=66, INITIAL_STATE=.FALSE./

&DEVC ID='PART-TIME-8', XYZ=1.0, 0.0, 5.0, QUANTITY='TIME', SETPOINT=67, INITIAL_STATE=.FALSE./

&DEVC ID='PART-TIME-9', XYZ=1.0, 0.0, 5.0, QUANTITY='TIME', SETPOINT=68, INITIAL_STATE=.FALSE./

&DEVC ID='PART-TIME-10', XYZ=1.0, 0.0, 5.0, QUANTITY='TIME', SETPOINT=69, INITIAL_STATE=.FALSE./

&DEVC ID='PART-TIME-11', XYZ=1.0, 0.0, 5.0, QUANTITY='TIME', SETPOINT=70, INITIAL_STATE=.FALSE./

&DEVC ID='PART-TIME-12', XYZ=1.0, 0.0, 5.0, QUANTITY='TIME', SETPOINT=71, INITIAL_STATE=.FALSE./

&DEVC ID='PART-TIME-13', XYZ=1.0, 0.0, 5.0, QUANTITY='TIME', SETPOINT=72, INITIAL_STATE=.FALSE./

&DEVC ID='PART-TIME-14', XYZ=1.0, 0.0, 5.0, QUANTITY='TIME', SETPOINT=73, INITIAL_STATE=.FALSE./

&DEVC ID='PART-TIME-15', XYZ=1.0, 0.0, 5.0, QUANTITY='TIME', SETPOINT=74, INITIAL_STATE=.FALSE./

&DEVC ID='PART-TIME-16', XYZ=1.0, 0.0, 5.0, QUANTITY='TIME', SETPOINT=75, INITIAL_STATE=.FALSE./

&DEVC ID='PART-TIME-17', XYZ=1.0, 0.0, 5.0, QUANTITY='TIME', SETPOINT=76, INITIAL_STATE=.FALSE./

&DEVC ID='PART-TIME-18', XYZ=1.0, 0.0, 5.0, QUANTITY='TIME', SETPOINT=77, INITIAL_STATE=.FALSE./

&DEVC ID='PART-TIME-19', XYZ=1.0, 0.0, 5.0, QUANTITY='TIME', SETPOINT=78, INITIAL_STATE=.FALSE./

&DEVC ID='PART-TIME-20', XYZ=1.0, 0.0, 5.0, QUANTITY='TIME', SETPOINT=79, INITIAL_STATE=.FALSE./

&DEVC ID='PART-TIME-21', XYZ=1.0, 0.0, 5.0, QUANTITY='TIME', SETPOINT=80, INITIAL_STATE=.FALSE./

&DEVC ID='PART-TIME-22', XYZ=1.0, 0.0, 5.0, QUANTITY='TIME', SETPOINT=81, INITIAL_STATE=.FALSE./

&DEVC ID='PART-TIME-23', XYZ=1.0, 0.0, 5.0, QUANTITY='TIME', SETPOINT=82, INITIAL_STATE=.FALSE./

&DEVC ID='PART-TIME-24', XYZ=1.0, 0.0, 5.0, QUANTITY='TIME', SETPOINT=83, INITIAL_STATE=.FALSE./

&DEVC ID='PART-TIME-25', XYZ=1.0, 0.0, 5.0, QUANTITY='TIME', SETPOINT=84, INITIAL_STATE=.FALSE./

&DEVC ID='PART-TIME-26', XYZ=1.0, 0.0, 5.0, QUANTITY='TIME', SETPOINT=85, INITIAL_STATE=.FALSE./

&DEVC ID='PART-TIME-27', XYZ=1.0, 0.0, 5.0, QUANTITY='TIME', SETPOINT=86, INITIAL_STATE=.FALSE./

&DEVC ID='PART-TIME-28', XYZ=1.0, 0.0, 5.0, QUANTITY='TIME', SETPOINT=87, INITIAL_STATE=.FALSE./

&DEVC ID='PART-TIME-29', XYZ=1.0, 0.0, 5.0, QUANTITY='TIME', SETPOINT=88, INITIAL_STATE=.FALSE./

&DEVC ID='PART-TIME-30', XYZ=1.0, 0.0, 5.0, QUANTITY='TIME', SETPOINT=89, INITIAL_STATE=.FALSE./

&DEVC ID='PART-TIME-31', XYZ=1.0, 0.0, 5.0, QUANTITY='TIME', SETPOINT=90, INITIAL_STATE=.FALSE./

&DEVC ID='PART-TIME-32', XYZ=1.0, 0.0, 5.0, QUANTITY='TIME', SETPOINT=91, INITIAL_STATE=.FALSE./

&DEVC ID='PART-TIME-33', XYZ=1.0, 0.0, 5.0, QUANTITY='TIME', SETPOINT=92, INITIAL_STATE=.FALSE./

&DEVC ID='PART-TIME-34', XYZ=1.0, 0.0, 5.0, QUANTITY='TIME', SETPOINT=93, INITIAL_STATE=.FALSE./

&DEVC ID='PART-TIME-35', XYZ=1.0, 0.0, 5.0, QUANTITY='TIME', SETPOINT=94, INITIAL_STATE=.FALSE./

&DEVC ID='PART-TIME-36', XYZ=1.0, 0.0, 5.0, QUANTITY='TIME', SETPOINT=95, INITIAL_STATE=.FALSE./

&DEVC ID='PART-TIME-37', XYZ=1.0, 0.0, 5.0, QUANTITY='TIME', SETPOINT=96, INITIAL_STATE=.FALSE./

&DEVC ID='PART-TIME-38', XYZ=1.0, 0.0, 5.0, QUANTITY='TIME', SETPOINT=97, INITIAL_STATE=.FALSE./

&DEVC ID='PART-TIME-39', XYZ=1.0, 0.0, 5.0, QUANTITY='TIME', SETPOINT=98, INITIAL_STATE=.FALSE./

&DEVC ID='PART-TIME-40', XYZ=1.0, 0.0, 5.0, QUANTITY='TIME', SETPOINT=99, INITIAL_STATE=.FALSE./

&DEVC ID='PART-TIME-41', XYZ=1.0, 0.0, 5.0, QUANTITY='TIME', SETPOINT=100, INITIAL_STATE=.FALSE./

&DEVC ID='PART-TIME-42', XYZ=1.0, 0.0, 5.0, QUANTITY='TIME', SETPOINT=101, INITIAL_STATE=.FALSE./

&DEVC ID='PART-TIME-43', XYZ=1.0, 0.0, 5.0, QUANTITY='TIME', SETPOINT=102, INITIAL_STATE=.FALSE./

&DEVC ID='PART-TIME-44', XYZ=1.0, 0.0, 5.0, QUANTITY='TIME', SETPOINT=103, INITIAL_STATE=.FALSE./

&DEVC ID='PART-TIME-45', XYZ=1.0, 0.0, 5.0, QUANTITY='TIME', SETPOINT=104, INITIAL_STATE=.FALSE./

&DEVC ID='PART-TIME-46', XYZ=1.0, 0.0, 5.0, QUANTITY='TIME', SETPOINT=105, INITIAL_STATE=.FALSE./

&DEVC ID='PART-TIME-47', XYZ=1.0, 0.0, 5.0, QUANTITY='TIME', SETPOINT=106, INITIAL_STATE=.FALSE./

```
&DEVC ID='PART-TIME-48', XYZ=1.0, 0.0, 5.0, QUANTITY='TIME',  SETPOINT=107, INITIAL_STATE=.FALSE./
&DEVC ID='PART-TIME-49', XYZ=1.0, 0.0, 5.0, QUANTITY='TIME',  SETPOINT=108, INITIAL_STATE=.FALSE./
&DEVC ID='PART-TIME-50', XYZ=1.0, 0.0, 5.0, QUANTITY='TIME',  SETPOINT=109, INITIAL_STATE=.FALSE./
&DEVC ID='PART-TIME-51', XYZ=1.0, 0.0, 5.0, QUANTITY='TIME',  SETPOINT=110, INITIAL_STATE=.FALSE./
&DEVC ID='PART-TIME-52', XYZ=1.0, 0.0, 5.0, QUANTITY='TIME',  SETPOINT=111, INITIAL_STATE=.FALSE./
&DEVC ID='PART-TIME-53', XYZ=1.0, 0.0, 5.0, QUANTITY='TIME',  SETPOINT=112, INITIAL_STATE=.FALSE./
&DEVC ID='PART-TIME-54', XYZ=1.0, 0.0, 5.0, QUANTITY='TIME',  SETPOINT=113, INITIAL_STATE=.FALSE./
&DEVC ID='PART-TIME-55', XYZ=1.0, 0.0, 5.0, QUANTITY='TIME',  SETPOINT=114, INITIAL_STATE=.FALSE./
&DEVC ID='PART-TIME-56', XYZ=1.0, 0.0, 5.0, QUANTITY='TIME',  SETPOINT=115, INITIAL_STATE=.FALSE./
&DEVC ID='PART-TIME-57', XYZ=1.0, 0.0, 5.0, QUANTITY='TIME',  SETPOINT=116, INITIAL_STATE=.FALSE./
&DEVC ID='PART-TIME-58', XYZ=1.0, 0.0, 5.0, QUANTITY='TIME',  SETPOINT=117, INITIAL_STATE=.FALSE./
&DEVC ID='PART-TIME-59', XYZ=1.0, 0.0, 5.0, QUANTITY='TIME',  SETPOINT=118, INITIAL_STATE=.FALSE./
&DEVC ID='PART-TIME-60', XYZ=1.0, 0.0, 5.0, QUANTITY='TIME',  SETPOINT=119, INITIAL_STATE=.FALSE./
&DEVC ID='PART-TIME-61', XYZ=1.0, 0.0, 5.0, QUANTITY='TIME',  SETPOINT=120, INITIAL_STATE=.FALSE./
&DEVC ID='PART-TIME-62', XYZ=1.0, 0.0, 5.0, QUANTITY='TIME',  SETPOINT=121, INITIAL_STATE=.FALSE./
&DEVC ID='PART-TIME-63', XYZ=1.0, 0.0, 5.0, QUANTITY='TIME',  SETPOINT=122, INITIAL_STATE=.FALSE./
&DEVC ID='PART-TIME-64', XYZ=1.0, 0.0, 5.0, QUANTITY='TIME',  SETPOINT=123, INITIAL_STATE=.FALSE./
&DEVC ID='PART-TIME-65', XYZ=1.0, 0.0, 5.0, QUANTITY='TIME',  SETPOINT=124, INITIAL_STATE=.FALSE./
&DEVC ID='PART-TIME-66', XYZ=1.0, 0.0, 5.0, QUANTITY='TIME',  SETPOINT=125, INITIAL_STATE=.FALSE./
&DEVC ID='PART-TIME-67', XYZ=1.0, 0.0, 5.0, QUANTITY='TIME',  SETPOINT=126, INITIAL_STATE=.FALSE./
&DEVC ID='PART-TIME-68', XYZ=1.0, 0.0, 5.0, QUANTITY='TIME',  SETPOINT=127, INITIAL_STATE=.FALSE./
&DEVC ID='PART-TIME-69', XYZ=1.0, 0.0, 5.0, QUANTITY='TIME',  SETPOINT=128, INITIAL_STATE=.FALSE./
&DEVC ID='PART-TIME-70', XYZ=1.0, 0.0, 5.0, QUANTITY='TIME',  SETPOINT=129, INITIAL_STATE=.FALSE./

++++++++++++++++++            FIRE SOURCE            +++++++++++++++

&PART  ID='fire needles',
                    SAMPLING_FACTOR=1,
                    SURF_ID='fire',
                    PROP_ID='needle image',
                    STATIC=.TRUE. /
&INIT     PART_ID='fire needles',
                    XB=30.001,34.999,-4.999,4.999,3.001,7.999,
                    N_PARTICLES_PER_CELL=1,
                    PARTICLE_WEIGHT_FACTOR=2017/
&PROP  ID='needle image',
                    SMOKEVIEW_ID='TUBE',
                    SMOKEVIEW_PARAMETERS='L=0.3','D=0.0005' /
&SURF  ID = 'fire',
                    MLRPUA = 0.00324622626197,
                    MATL_ID = 'FIRE_NEEDLE',
                    THICKNESS = 0.000400534,
                    LENGTH = 0.3,
                    GEOMETRY = 'CYLINDRICAL' /
&MATL  ID = 'FIRE_NEEDLE',
                    DENSITY = 100.0,
                    CONDUCTIVITY = 0.24,
                    SPECIFIC_HEAT = 1.466 /
&TAIL /
```

Appendix C: Matlab Function for reading the FDS Particle File [73]

```
function [STIME, XP, YP, ZP, QP, varargout] = read_prt5(filename,precision,varargin)

nout = max(nargout,1);

evac = false;
if size(varargin)>0
    if strcmp(varargin{1},'evac') | strcmp(varargin{1},'EVAC') | strcmp(varargin{1},'Evac')
        evac = true;
    end
end

fid = fopen(filename);

DUMMY       = fread(fid,1,'integer*4');
ONE_INTEGER = fread(fid,1,'integer*4');
DUMMY       = fread(fid,1,'integer*4');

DUMMY       = fread(fid,1,'integer*4');
INT_VERSION = fread(fid,1,'integer*4');
DUMMY       = fread(fid,1,'integer*4');

DUMMY  = fread(fid,1,'integer*4');
N_PART = fread(fid,1,'integer*4');
DUMMY  = fread(fid,1,'integer*4');

for NPC=1:N_PART

    DUMMY = fread(fid,1,'integer*4');
    PC    = fread(fid,2,'integer*4'); N_QUANTITIES(NPC) = PC(1);
    DUMMY = fread(fid,1,'integer*4');

    for NQ=1:N_QUANTITIES(NPC)
        DUMMY               = fread(fid,1,'integer*4');
        SMOKEVIEW_LABEL{NQ} = fgets(fid,30);
        DUMMY               = fread(fid,1,'integer*4');

        DUMMY     = fread(fid,1,'integer*4');
        UNITS{NQ} = fgets(fid,30);
        DUMMY     = fread(fid,1,'integer*4');
    end

end
```

```
while ~feof(fid)
    n = n + 1;

    DUMMY = fread(fid,1,'integer*4');
    stime_tmp = fread(fid,1,precision);
    DUMMY = fread(fid,1,'integer*4');

    if size(stime_tmp,1)==0
        break
    else
        STIME(n) = stime_tmp;
    end

    for NPC=1:N_PART

        DUMMY = fread(fid,1,'integer*4');
        NPLIM = fread(fid,1,'integer*4');
        DUMMY = fread(fid,1,'integer*4');

        DUMMY = fread(fid,1,'integer*4');
        xp = fread(fid,NPLIM,precision);
        yp = fread(fid,NPLIM,precision);
        zp = fread(fid,NPLIM,precision);
        if evac
            ap1 = fread(fid,NPLIM,precision);
            ap2 = fread(fid,NPLIM,precision);
            ap3 = fread(fid,NPLIM,precision);
            ap4 = fread(fid,NPLIM,precision);
        end
        DUMMY = fread(fid,1,'integer*4');

        for NP=1:NPLIM
            XP(n,NP,NPC) = xp(NP);
            YP(n,NP,NPC) = yp(NP);
            ZP(n,NP,NPC) = zp(NP);
            if evac & nout==6
                AP(n,NP,NPC,1) = ap1(NP);
                AP(n,NP,NPC,2) = ap2(NP);
                AP(n,NP,NPC,3) = ap3(NP);
                AP(n,NP,NPC,4) = ap4(NP);
            end
        end
        %clear xp yp zp

        DUMMY = fread(fid,1,'integer*4');
        TA    = fread(fid,NPLIM,'integer*4');
        DUMMY = fread(fid,1,'integer*4');

        if N_QUANTITIES(NPC)>0
            DUMMY = fread(fid,1,'integer*4');
            for NQ=1:N_QUANTITIES(NPC)
                qp = fread(fid,NPLIM,precision);
                for NP=1:NPLIM
                    QP(n,NP,NPC,NQ) = qp(NP);
                end
                %clear qp
            end
            DUMMY = fread(fid,1,'integer*4');
        end

    end

end
fclose(fid);

if evac & nout==6
    varargout{1} = AP;
end
```

Appendix D: FDS Input for the Validation of the Pyrolysis model

```
&MESH IJK=4,4,4, XB=-2,2,-2,2,-2,2 /

&TIME T_END=9600. /

&MISC Solid_Phase_only=.True.,
Y_O2_INFTY=0.0000001,
ASSUMED_GAS_TEMPERATURE=820.,
ASSUMED_GAS_TEMPERATURE_RAMP='T_RAMP' /

&RAMP ID = 'T_RAMP' T = 0.,    F = 0. /
&RAMP ID = 'T_RAMP' T = 9600., F = 1.0 /

&REAC   FUEL = 'CARBON MONOXIDE',
                SOOT_YIELD = 0.03092783505,
                CO_YIELD = 0.000,
                C = 1,
                H = 0,
                O = 1,
                HEAT_OF_COMBUSTION=10100./
&SURF ID='brand',
          MATL_ID='Vegetation',
          COLOR    = 'RED',
          BACKING   = 'INSULATED' ,
          THICKNESS=0.00001,
          LENGTH=1.0,
          HEAT_TRANSFER_COEFFICIENT=10000.0
          GEOMETRY='CYLINDRICAL'/
```

```
&MATL ID = 'Vegetation',
          DENSITY = 100.,
          CONDUCTIVITY = 0.24,
          SPECIFIC_HEAT = 1.466,
          EMISSIVITY=0.9,
          N_S(1) = 1.0,
          A(1) = 725.0,
          E(1) = 57361.48,
          MATL_ID(1,1) = 'CHAR',
          NU_MATL(1,1) = 0.39,
          SPEC_ID(1:2,1) = 'CARBON MONOXIDE', 'CARBON DIOXIDE'
          NU_SPEC(1:2,1) = 0.488,0.122,
          HEAT_OF_REACTION = 418.0 /

&MATL ID = 'CHAR',
          DENSITY = 39.0,
          CONDUCTIVITY = 0.1,
          EMISSIVITY=0.9,
          SPECIFIC_HEAT = 1.1 /

&PART    ID='brand_part', SURF_ID='brand',STATIC=.TRUE.,
         PROP_ID='particle', QUANTITIES='PARTICLE MASS'/
&INIT ID='example', PART_ID='brand_part', XYZ=0.,0.,0.0, N_PARTICLES = 1  /
```

Figure 49: FDS input to imitate TGA experiments.

```
&MESH IJK=20,20,20, XB=-1,1,-1,1,-1,1 /
&INIT XB=-1,1,-1,1,-1,1, TEMPERATURE=20.0 /

&MISC TMPA=900.0/

&VENT SURF_ID='OPEN' PBX=-1.0, TMP_EXTERIOR=20.0 /
&VENT SURF_ID='OPEN' PBX=1.0,TMP_EXTERIOR=20.0 /
&VENT SURF_ID='OPEN' PBY=-1.0, TMP_EXTERIOR=20.0 /
&VENT SURF_ID='OPEN' PBY=1.0,TMP_EXTERIOR=20.0 /
&VENT SURF_ID='OPEN' PBZ=1.0,TMP_EXTERIOR=20.0 /
&VENT SURF_ID='OPEN' PBZ=-1.0,TMP_EXTERIOR=20.0 /

&PRES MAX_PRESSURE_ITERATIONS=100 /

&REAC   FUEL = 'CARBON MONOXIDE',
                SOOT_YIELD = 0.0306597938,
                CO_YIELD = 0.000,
                C = 1,
                H = 0,
                O = 1,
                HEAT_OF_COMBUSTION=10100.,
                AUTO_IGNITION_TEMPERATURE=0.0/

&PART   ID='brand_part', SURF_ID='brand',STATIC=.TRUE., PROP_ID='particle'/

&INIT ID='example', PART_ID='brand_part', XYZ=0,0,0, N_PARTICLES = 1  /
```

```
&SURF ID='brand',
          MATL_ID='Vegetation',
          COLOR    = 'RED',
          BACKING   = 'INSULATED' ,
          THICKNESS=0.05,
          LENGTH=0.08862269,
          WIDTH=0.08862269,
          MINIMUM_LAYER_THICKNESS = 0.00000000005,
          GEOMETRY='CARTESIAN' /

&MATL ID = 'Vegetation',
          DENSITY = 150.,
          CONDUCTIVITY = 0.24,
          SPECIFIC_HEAT = 1.466,
          EMISSIVITY=0.9,
          N_S(1) = 1.0,
          A(1) = 725.0,
          E(1) = 57361.48,
          MATL_ID(1,1) = 'CHAR',
          NU_MATL(1,1) = 0.39,
          SPEC_ID(1:2,1) = 'CARBON MONOXIDE', 'CARBON DIOXIDE'
          NU_SPEC(1:2,1) = 0.488,0.122,
          HEAT_OF_REACTION = 418.0 /

&MATL ID = 'CHAR',
          DENSITY = 58.5,
          CONDUCTIVITY = 0.1,
          EMISSIVITY=0.9,
          SPECIFIC_HEAT = 1.1 /
```

Figure 50: FDS input to imitate burning behaviour of firebrands.

Appendix E: Additional Material for Pyrolysis Model Analysis

Figure 51 shows the cooling of firebrands with different thicknesses. The particles are equivalent to a disc-shaped firebrand with a diameter of 10 cm. The density of all brands from this test was taken as 150 kg/m³ and the initial temperature of the particles was 900°C with 20°C being the temperature of the ambient gases. Figure 52 gives the heat release rates for the same particles over time.

Figure 53 shows the surface temperature of particles against the heat release rate from the same for different thicknesses. The particles from these tests were all equivalent to 10 cm in diameter at an initial temperature of 900°C and the density was taken as 150 kg/m³.

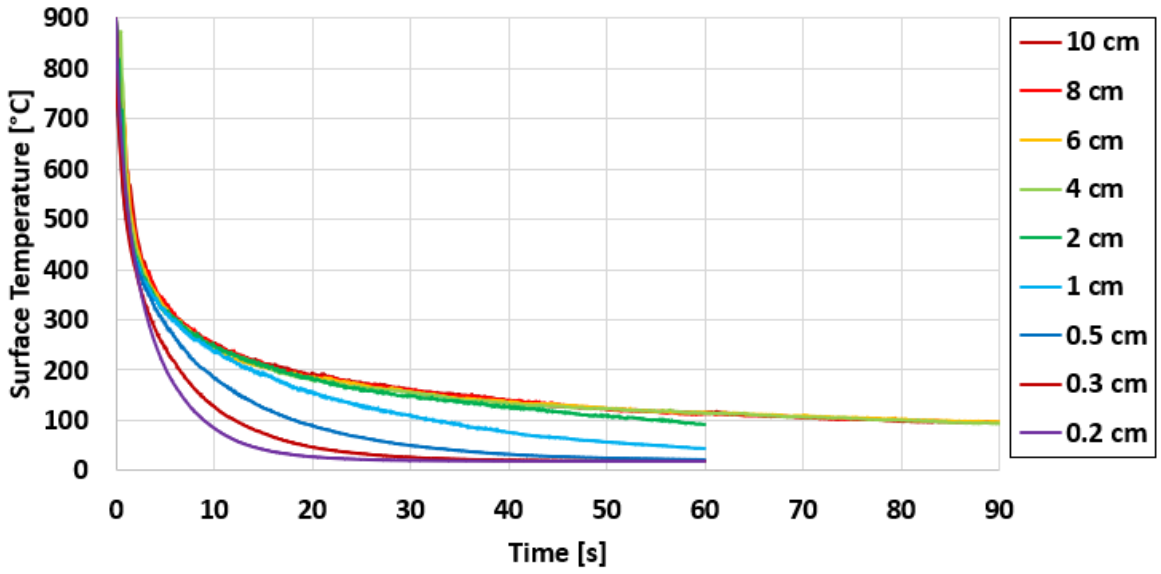

Figure 51: Cooling behaviour of firebrands of different thickness.

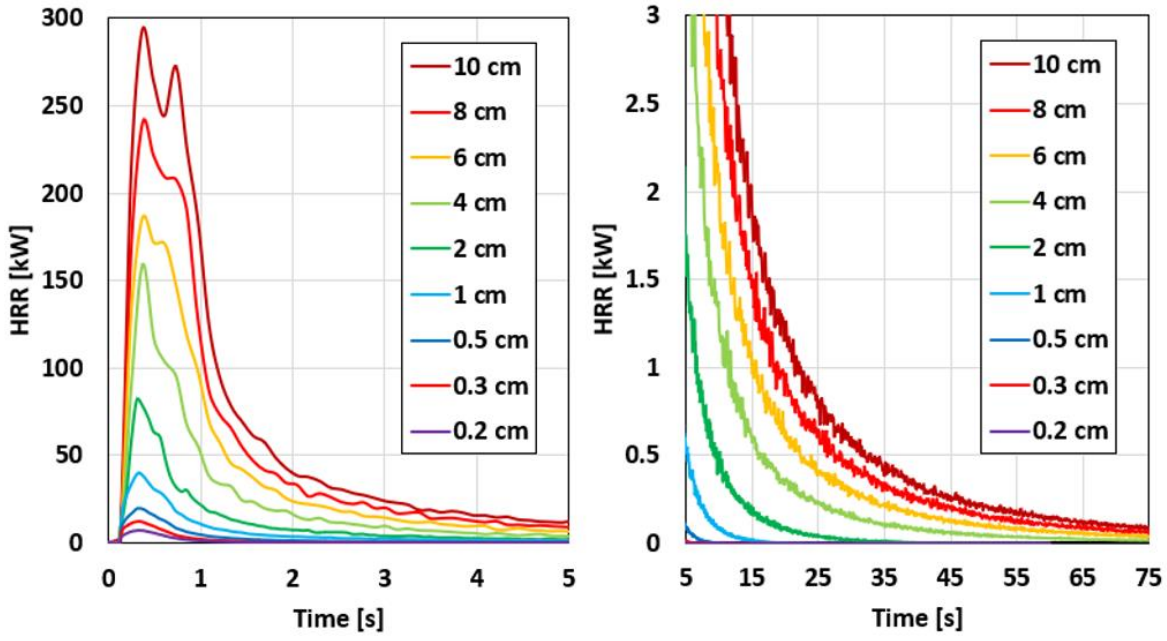

Figure 52: HRR from particles of different thickness.

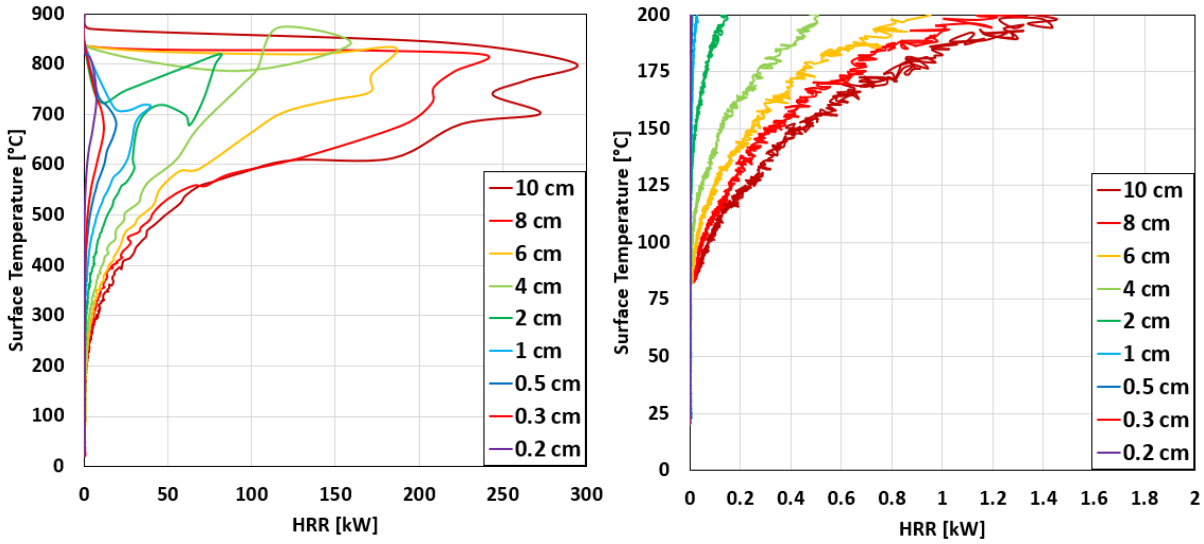

Figure 53: Surface temperature vs. heat release rate for particles of different thickness.

Appendix F: Additional Results on the Landing Distance

Figure 51 shows additional data for the landing distance of firebrands over the initial density times the thickness of a brand.

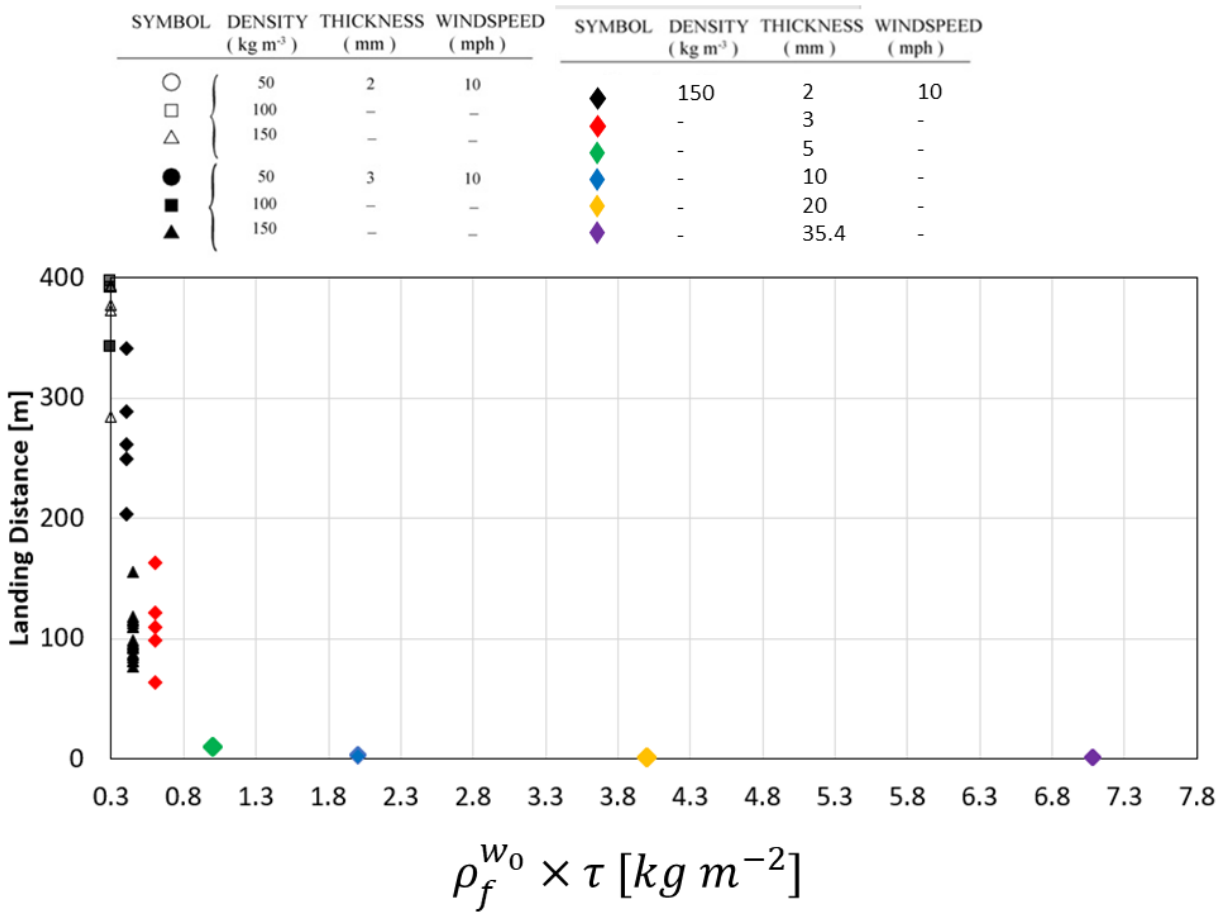

Figure 54: Additional results on the landing distance of firebrands over the product of initial density times thickness. Parts of the legend is after [39].